Phase Equilibria and Thermochemistry of Advanced Fuels: Modeling Burnup Behavior

Final Report

Federal Agency and Organization Element	U.S. Department of Energy Office of Nuclear Research
Award Number	DE-NE0008570 Project 16-10204
Principal Investigator	Theodore M. Besmann (University of South Carolina)
Collaborators	Jacob W. McMurray (Oak Ridge National Laboratory) Andrew T. Nelson, Joshua T. White (Los Alamos National Laboratory) Edward J. Lahoda, Simon C. Middleburgh, Antoine Claisse (Westinghouse Electric Company, LLC)
Contributors	Tashiema L. Ulrich Kaitlin E. Johnson Vancho Kocevski Denise Adorno Lopes Sven Vogel
Recipient Organization	University of South Carolina Sponsored Awards Management 1600 Hampton Street, Suite 414 Columbia, SC 29208
Submission Date	March 31, 2020

Abstract

Achieving the goal of developing advanced fuel concepts that meet the DOE objectives of being robust, demonstrating high performance, and are more tolerant of accident conditions than current fuel systems will require a thorough understanding of the thermophysical and thermochemical properties of the constituent materials. Non-oxide fuel systems are being explored under the Advanced Fuels Program that hold significant promise for improved performance and accident tolerance, including the uranium silicide-based system considered in the current work.

Prospective cladding materials currently considered that contribute to improved accident tolerance include silicon carbide composites and ferritic alloys (Fe-Cr-Al base compositions). Thus, the effort developed thermochemical models and values, supported with targeted experiments, to evaluate the ferritic alloy and silicon carbide composite cladding systems in contrast to current zirconium alloy cladding. The developed detailed understanding will serve to aid in relatively early screening of candidate systems to avoid wasted effort, guide development of new fuel forms, and to provide a basis for predicting and modeling fuel performance.

Major deliverables for the project included: Thermochemical assessment and models of phases in the U-Si and U-Si-N systems; thermochemical evaluation supported by experimental measurements of fuel-cladding interactions of silicide fuel with baseline zirconium, ceramic composite, and ferritic alloy cladding; thermochemical assessment and models of phases supported by experimental measurements for silicide fuel with key fission products provided in a dataset and reported in refereed publications.

Within the project a significantly refined U-Si phase diagram was developed and reported that now includes homogeneity ranges for key phases, such at the U_3Si_2 proposed fuel phase, and settles issues with regard to uncertainty in the stability of some phases. Computational efforts together with key experiments has determined phase formation in interactions between U_3Si_2 and Zircaloy-4 cladding material, a ferritic FeCrAlY alloy of interest as an advanced cladding material, and silicon carbide, also of interest as a fiber-reinforced composite cladding. As expected, very significant reactions occur between U_3Si_2 and Zircaloy-4, with much less interaction at higher temperatures for the ferritic alloy, and finally interactions with SiC only in the region of contact.

A potentially major issue is the stability of U_3Si_2 fuel that has undergone significant burnup. The result is the loss of the uranium metal, liberating silicon, and the formation of concomitant fission product elements that either dissolve in the U_3Si_2 phase or form independent, and possibly silicide phases. A combination of experimental determinations of phase formation of U_3Si_2 reacted with representative fission products yttrium, gadolinium, cerium, zirconium, and molybdenum and first principles calculations has helped understand the fuel chemistry. The behavior of the U_3Si_2 phase and the partitioning of silicon to possible fission product phases with burnup was thus determined, with significant dissolution in U_3Si_2 of cerium, gadolinium, zirconium, and plutonium predicted along with independent phase formation of a U-Mo-Si ternary phase, yttrium silicide, and elemental selenium. It can be concluded that at significant burnup there will be a very minor amount of the U_3Si_2 fuel phase that will decompose to a lower silicide or a uranium alloy as silicon preferentially forms a secondary phase.

Table of Contents

List of Tables

List of Figures

1. Introduction

The accident at Fukushima Dai'ichi has inspired creative approaches to replacing UO_2-zirconium alloy cladding with materials less susceptible to rapid oxidation and loss of integrity during a loss of coolant accident (LOCA) or station blackout. There is additional interest in improving fuel performance with higher uranium density and thermal conductivity fuels. The current Department of Energy Advanced Fuels Program targeting accident tolerant fuels together with industry initiatives has prioritized the study of uranium silicide and composite nitride-silicide systems [1, 2]. To complement these are alternative cladding concepts with the leading candidates being ferritic Fe-Cr-Al alloys and SiC composite materials [3, 4]. Neutronic [5, 6] and fuel cycle analyses [7] are generally positive with regard to the use of these fuel and cladding systems in current light water reactors (LWRs).

Industry and DOE program efforts are focused on fabrication methodologies, further experimental assessments of compatibility among the materials, environmental stability, and irradiation testing. There is a need therefore, to support that development with an understanding of phase equilibria and thermochemistry of the fuel and cladding materials with respect to their long-term stability, potential for interaction among the materials, and impact of significant generation of FPs. Hampering the assessment of the fuel systems is the lack of critical phase equilibria and thermochemical data for strategic compositions. The understanding of the U-N system is likely adequate for these analyses, yet there may remain uncertainties in the U-Si system, including a possible unidentified USi_{2-x} phase. Existing DOE programmatic efforts on uranium silicides have made progress in understanding important properties and phases in the U-Si system, and thus the goal of the proposed effort is to utilize those results in broader models and provide complementary analyses. There are also indications of formation of a high temperature ternary phase in the U-Si-N system, but other than that no ternary phase information is reported. Issues such as the solubility of silicon in UN, or conversely of nitrogen in uranium silicides, are not understood. Therefore assessments of these systems need to be undertaken.

It is understood that irradiated fuels will suffer from radiation damage and therefore see substantially larger defect concentrations such as vacancies and interstitials than expected at equilibrium. Yet despite these non-equilibrium effects, determining the equilibrium state is important for several reasons. First, it is at least the starting point for detailed modeling of fuel behavior from which one could then investigate the effect of radiation-induced defects. Second, given the high operating temperatures and relatively long time scales, radiation-caused defects can anneal and thus local equilibrium may still predominate. It has also been argued that irradiation can cause thermal spikes and therefore temperatures can exceed those computed from volumetric power generation, thus causing unexpected phase transitions. This indeed can occur, but again, after a thermal spike temperatures return to steady-state values and thus the phase state can similarly adjust.

With a thermochemical understanding and thus a set of free energy relations for the fuel phases it will be possible to determine their stability with respect to baseline zirconium and prospective ferritic alloy and SiC composite cladding materials. Database values for the alloys and SiC are available, as well as those for a proportion of major interaction products that will allow direct application.[8, 9] Thus it will be possible to explore a wide range of conditions for fuel-cladding systems to predict behavior. These will be tested by exposures of fuel and cladding materials at relevant temperatures with post-exposure microanalysis used to identify interactions and their products. As needed, thermochemical relations for additional reaction products will be developed.

The determination of the influence of FP generation on the fuel-cladding systems is important. Essentially, the fuel phases need to be evaluated as "SIMFUELS" where simulated FP compositions for relatively high burnups are mixed with the fuel to chemically simulate irradiation. The result can provide insight into partitioning of FPs between the fuel phase and secondary phases, and thus their direct contribution to

swelling and the evolution of thermophysical properties such as conductivity, heat capacity, and thermal expansion, which in turn will impact the modeling of phenomena such as pellet cladding mechanical interactions (PCMI). In addition, the fate of FP elements will directly impact pellet-cladding chemical interactions (PCCI). It is thus important to understand the chemical state and activities of reactive FPs so that their potential for cladding attack can be judged. Selected SIMFUEL compositions will be experimentally prepared, subjected to high temperature to affirm expected phase formation and provide any needed adjustments to the thermochemical understanding. Ultimately, SIMFUEL formulations can be tested in contact with potential cladding materials to evaluate compatibility during burnup, and compared to expected behavior predicted from thermochemical analysis.

1.1. Project Objectives

Achieving the goal of developing advanced fuel concepts that meet the DOE objectives of being robust, demonstrating high performance, and are more tolerant of accident conditions than current fuel systems will require a thorough understanding of the thermophysical and thermochemical properties of the constituent materials. Non-oxide fuel systems are being explored under the Advanced Fuels Program that hold significant promise for improved performance and accident tolerance, including uranium silicide-based systems considered in the research reported here.

Currently considered prospective cladding materials that contribute to improved accident tolerance include silicon carbide composites and ferritic alloys (Fe-Cr-Al base compositions). Thus, thermochemical models and values have been developed, and supported with targeted experiments, allowed preliminary evaluation of the various fuel-cladding systems. Such a detailed understanding will serve to aid in early screening of candidate systems to avoid wasted effort, guide development of new fuel forms, and to provide a basis for predicting and modeling fuel performance.

Issues such as phase stability, particularly among composite (two-phase) fuels, compatibility with prospective cladding materials, and behavior during burnup are important. Burnup effects to consider include the solubility of fission products (FPs) and their contribution to swelling, formation of secondary phases, and FP interaction with cladding materials. While a complete and accurate determination of thermophysical/chemical properties for the materials is desirable, combining a comprehensive set of thermodynamic values with a complete set of kinetic mechanisms for all interactions, it is certainly not practical. The targeted generation of properties and behaviors, however, can provide both critical insight for development and important data for fuel performance modeling. It was the objective to provide the phase equilibria and thermochemical aspects necessary to achieve these goals, including critical information such as the contribution to fuel swelling of dissolved non-noble FPs, secondary phase formation, and interactions with cladding. The culmination of this research will be to provide a dataset directly usable in fuel performance codes, for example BISON coupled to THERMOCHIMICA, a chemical equilibrium solver designed to return chemical activity and phase information to BISON to inform burnup simulations. Development of this capability is progressing under the Nuclear Energy Advanced Modeling and Simulation (NEAMS) program and will need the proposed dataset to model advanced fuel performance.

It should be noted that while there were no changes in actual tasks within the project, feedback from Westinghouse Electric Company, LLC early in the project period indicated a lesser interest in UN-containing systems. As a result, greater emphasis in the research was placed on understanding silicide-related issues. Specific project milestones/activities are listed below, with all successfully accomplished and documented in here and in separate reports.

- Develop models for U-Si and U-Si-N phase systems
- Thermochemical evaluation of fuel-cladding interactions of nitride, silicide, and composite fuel with baseline zirconium, SiC composite, and ferritic alloy cladding

- Thermochemical assessment and models of phases for nitride/silicide fuels with key FPs and generate models for use in codes
- Develop models values in FactSage and THERMOCHIMICA use format
- Experimental results from of fuel-cladding diffusion couples with baseline Zr-alloy, SiC composite, and ferritic alloys
- Experimental evaluation of phase formation in silicide fuels with simulated FPs

2. Non-Stoichiometry in U_3Si_2

The U_3Si_2 phase possesses a tetragonal unit cell with space group *P4/mbm*. The crystal structure and phase stability of U_3Si_2 were confirmed by room temperature X-ray diffraction on arc-melted and annealed U_3Si_2 samples [10] and room temperature neutron diffraction on irradiated U_3Si_2 [11]. However, more recently, Obbard et al. [12] conducted the first high temperature neutron diffraction study to 1873 K and reported a new crystal structure with *P4/mmm* space group above 1273 K. While the data quality did not allow for determination of crystallographic parameters, the reflections above 1273 K, the reduction in peak intensities for *P4/mbm* and a diverging coefficient of thermal expansion support the assertion of a new structure. Obbard et al. [12] reported that above 1000 K the coefficient of thermal expansion of U_3Si_2 began decreasing, which agrees with observations by White et al. [13], who studied the thermal expansion of U_3Si_2 by dilatometry up to 1673 K, and reported a constant coefficient of thermal expansion below ~1000 K.

Although a new crystal structure is a reasonable explanation for the above observations another possible explanation is a change in the defect concentration close to 1000 K. As uranium and silicon atoms create ordered vacancies and/or interstitials, new diffraction reflections and deviation in thermal expansion can be observed. Middleburgh *et al.* [14] utilized density functional theory (DFT) and thermochemical analysis to assess the stability of U_3Si_2 with respect to non-stoichiometry. They predicted: 1) U_3Si_2 contains stable interstitial Si sites (specifically at the 2b Wyckoff position), 2) U_3Si_2 is a line compound at room temperature, with excess Si forming Si-rich precipitates, and 3) above 1000 K there is a homogeneity range bounded by $U_3Si_{1.97}$ and $U_3Si_{2.03}$.

The Middleburgh *et al.* [14] predictions lend credence to the argument that deviations in thermal expansion and new reflections are due to defect formation. The same study, however, only relied on calculated defect enthalpies to assess the non-stoichiometry of U_3Si_{2+x} as function of temperature. Andersson *et al.* [15] expanded the effort to include defect formation entropies in the analysis and they predicted even higher Si-excess non-stoichiometry across a wide temperature range. For example, at 1250 K the non-stoichiometry was predicted to be as high as $U_3Si_{2.1}$, although some care should be applied to the interpretation of the exact value since their analysis acknowledged reduced accuracy for such high defect concentrations. The validation of these extensive theoretical studies motivates the current experimental work.

This study provides crystallographic information about the U_3Si_2 phase from investigating its crystal structure up to 1373 K using high temperature time-of-flight neutron diffraction. The proposed U_3Si_2 phase range has been verified, thermal expansion anisotropy was assessed, and the absolute bond lengths, the absolute lattice parameters and atomic displacement parameters were quantified. The potential hyperstoichiometry of U_3Si_2 was evaluated based on the formation energy and concentration of each point defect, in three different environments: 1) Si-rich environment, with excess Si from USi; 2) U-rich environment with excess Si from U_3Si; and 3) U_3Si_2 is near "perfect" stoichiometry.

2.1.1. Methodology

2.1.1. Sample Fabrication

Specimens of U_3Si_2 (with compositions U/Si = 3/2.00161 and U/Si = 3/2.00834) were synthesized by arc-melting the constitutive metals of depleted uranium (<0.2 atom % ^{235}U, rest ^{238}U) and 99.999% pure silicon (Cerac Inc., Milwaukee, Wisconsin) in a tri-arc system (5TA Reed Tri-Arc, Centorr Vacuum Industries, USA) as described by White et al.[16]. The difference between the initial and final mass of each sample was used to determine its composition to within 0.01 mg. For the composition, U/Si = 3/2.00161, the initial and final mass of the ingot was measured as 5.22917 g and 5.22300 g respectively, having a mass change of 6.17 mg. For the

composition, U/Si = 3/2.00834, the initial and final mass of the ingot was measured as 5.41160 g and 5.40807 g respectively, having a mass change of 3.53 mg. Assuming mass loss occurred because of Si volatilization, the change in Si stoichiometry was 0.00065 and 0.00303 for U/Si = 3/2.00161 and U/Si = 3/2.00834, respectively. The U/Si = 3/2.00161 composition will be referred to as $U_3Si_{2.00}$ and the U/Si = 3/2.00834 composition will be referred to as $U_3Si_{2.01}$ throughout the rest of this chapter.

Since uranium metal readily oxidizes, necessary precautions were taken to minimize oxygen exposure during arc melting. A copper getter was used to reduce the O_2 level from 10 ppm to 10^{-12} ppm in argon gas stream that flowed through the arc melter prior to melting depleted uranium and silicon. We used titanium as an additional getter during arc melting to further remove oxygen impurities. Arc melting was done inside a glovebox maintained at <0.1 ppm O_2 and H_2O. Oxygen levels were monitored during arc melting by oxygen sensors (Rapidox 3100 OEM, Cambridge Sensotec, UK) at the inlet and outlet of the tri-arc system.

Powder samples for neutron diffraction were prepared by crushing ~5 g ingot of U_3Si_2 using a mortar and pestle and sieved between a -200 and -325 mesh. Immediately after crushing, samples were placed in a W-mesh metal furnace and annealed at 1523 K for 20 hours in gettered argon atmosphere, limiting sample exposure to oxygen. Powdered samples were processed within an argon glovebox line maintained below 30 ppm O_2. Samples were directly loaded into vanadium sample containers immediately following annealing.

2.1.2. Neutron Diffraction Data Acquisition

A schematic of the High Pressure-Preferred Orientation (HIPPO) neutron time-of-flight diffractometer used in this study is provided in Fig. 2.1. HIPPO has 1,200 ^{3}He detector tubes mounted on 45 detector panels, which are arranged on five rings at 40° (lowest resolution), 60°, 90° (medium resolution), 120° and 145° (highest resolution) nominal diffraction angles, covering 22.4% of the sphere around the sample to detect the fraction of the ~2×10^7 n/s/cm^2 incident neutron intensity at 100 μA proton current scattered by the sample. An ILL-type (developed at the Institute Laue-Langevin in Grenoble specifically for neutron diffraction) vacuum furnace with vanadium heating elements and heat shields and operated at a vacuum pressure of <10^{-6} Torr was used inside the HIPPO sample chamber for high temperature measurements.

Vanadium was used as sample container and furnace heating elements and heat shields as it has a negligible coherent scattering cross-section of 0.0184 barns (coherent scattering length of b=-0.3824 fm) compared to ^{238}U (8.871 barns, b=8.402 fm) and Si (2.163 barns, b=4.1491 fm, all cross-sections from Sears, 1992) and therefore contributes negligible reflections in diffraction patterns. Also, there is no interaction between U_3Si_2 and vanadium at the temperatures of interest. In their experiments, Obbard *et al.* [12], used Al_2O_3 as sample container and furnace, which obscured the U_3Si_2 reflection peaks.

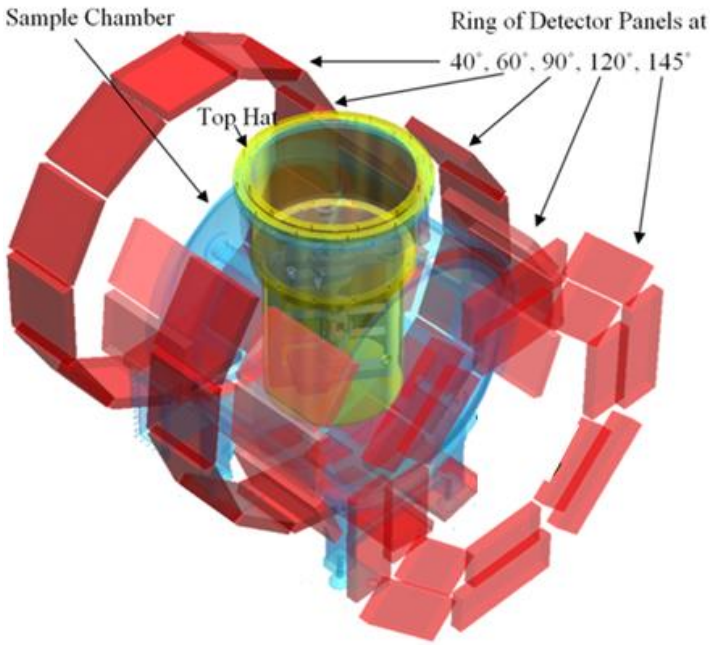

Fig. 2.1. Schematic of the High-Pressure Preferred Orientation (HIPPO) time of flight neutron diffractometer.

Listed in Table 2.1 are the temperatures at which time-of-flight neutron diffraction data were recorded. Neutron diffraction measurements were recorded every 200 K as the temperature increased from room temperature to 1198 K, then every 25 K from 1198 K to final temperature (1323 K and 1373 K for $U_3Si_{2.00}$ and $U_3Si_{2.01}$ respectively). The acquisition time per temperature dwell point was equivalent to 120 minutes at a proton current of 100 μA. For the $U_3Si_{2.01}$ sample, diffraction measurements were also recorded every 200 K as the sampled cooled to 298 K, which allowed for verification of any U-Si precipitate formation.

Utilizing a robotic sampler, long count time neutron data were collected to detect possible U-Si precipitates at low concentration (0.1-0.2 wt. %) approximately one year after collecting high temperature measurements. The data were collected for ~9 hours and ~12 hours at room temperature for $U_3Si_{2.00}$ and $U_3Si_{2.01}$, respectively. These data are referred to as the high-quality data.

Table 2.1. Time-of-flight neutron diffraction data collection temperatures.

Temperature [K]	$U_3Si_{2.00}$	$U_3Si_{2.01}$
298[a]	Heating	Heating
373	Heating	Heating
473		Cooling
573	Heating	Heating
673		Cooling
773	Heating	Heating
873		Cooling
973	Heating	Heating
1073		Cooling
1198	Heating	Heating
1223	Heating	Heating
1248	Heating	Heating
1273	Heating	Heating and Cooling
1298	Heating	Heating
1323		Heating
1348		Heating
1373		Heating

[a] Following the high temperature measurements, a series of measurements with longer acquisition times were recorded.

2.1.3. Neutron Diffraction Data Processing

Neutron diffraction data were subjected to Rietveld analysis to refine the crystallographic structure. Rietveld analysis was performed using GSAS [17] with scripts written in gsaslanguage [18] to ensure that all datasets (data from both samples at each temperature) were refined with the identical data analysis strategy. Each room temperature dataset was refined starting from the U_3Si_2 crystal structure reported by Zachariasen [19] (Inorganic Crystal Structure Database record 31648) with space group *P4/mbm* with all sites fully occupied and no additional Si sites. The vanadium crystal structure was introduced into the refinement of the high quality data to account for the weak signal from the sample container. Time-of-flight profile function #1 in GSAS was used and all five histograms (40°, 60°, 90°, 120° and 145° nominal diffraction angle) were refined simultaneously with a d-spacing range of 0.5 Å to 3.5 Å, including approximately 635 reflections.

Refined parameters included 12 background parameters per histogram (GSAS background function type 1), diffractometer constants DIFC (conversion from time-of-flight to d-spacing) for all histograms except for the highest resolution 145° backscattering detector bank (essentially adjusting the sample position), lattice parameters, isotropic atomic displacement parameters, atomic position parameters, one absorption parameter per histogram, and the peak width parameter σ_1 of the peak profile function #1 in GSAS. After the refinement of these parameters, the isotropic thermal motion parameters were converted to anisotropic thermal motion parameters and their values were refined together with all other parameters. The room temperature refinement with fixed diffractometer constants (essentially accounting for slight sample misalignment relative to the calibrated sample position) and absorption values were used as a starting point for all high temperature refinements. The maximum number of refined parameters was 91 for the room temperature runs and 82 for the high temperature runs (not including phase scale, lattice parameter and thermal motion parameter refined for the vanadium phase in the long runs).

GSAS routines were utilized to compute absolute bond lengths from the absolute lattice parameters and atom positions. The resulting crystal structure and difference Fourier maps

generated by GSAS after refinement were visualized using the VESTA package [18]. The absolute lattice parameters were used to quantify the coefficients of thermal expansion (CTEs) as a function of temperature using the Thermal Expansion Visualization (TEV) program [20]. Using TEV, second order polynomial fits were applied to the error-weighted lattice parameters vs. temperature. These polynomials and their derivatives were used to generate the 2nd order tensor describing the anisotropic thermal expansion.

2.1.4. DFT Calculations of Defect Energies and Entropies

The DFT calculations performed for this work followed the well-established methodology for the modeling of U_3Si_2 [14, 15, 21-25]. DFT calculations were performed with the Vienna Ab Initio Simulation (VASP) package [26]. The exchange and correlation interactions are accounted for using the generalized gradient approximation (GGA) as parametrized by Perdew-Burke-Ernzerhof (PBE) [27-30]. A 2x2x3 supercell (120 atoms) expansion of the U_3Si_2 unit cell was used to calculate the thermodynamic and kinetic properties for defect formation.
The point defect concentration (per U_3Si_2 unit cell) is expressed as:

$$C_{A_B} = Z_{A_B} \exp\left(\frac{F_{A_B,f}}{k_B T}\right) \quad 2.1$$

where A denotes the defect type (vacancy, interstitial or anti-site) and B denotes the species involved (U or Si), while Z_{AB} is the site multiplicity, T is the temperature, and k_B the Boltzmann constant. The corresponding site fractions (y_{AB}) and the fraction of A_B with respect to the total amount of B(u_{A_B}) can be derived from C_{A_B}. Vibrational defect entropies were calculated from the normal mode phonon frequencies following the approach of Mishin *et al*. [30].

At temperatures higher than the Debye temperature, the entropy of crystalline solids can be approximated as:

$$S = -k_B \sum_{n=1}^{3N-3} \ln\left(\frac{h\upsilon_n}{k_B T}\right) + (3N-3)k_B \quad 2.2$$

N is the number of atoms in the crystal, k_B is the Boltzmann constant, T is the temperature, and υ_n is the normal vibrational frequency of the crystal. The free energy (F) is calculated from the energy (E) and entropy (S) according to

$$F = E - TS \quad 2.3$$

The defect formation energy for vacancies and interstitial is obtained from supercell calculations according to:

$$E_{A_B,f} = E(A_B, N \pm 1) \mp e_B - E(N) \quad 2.4$$

and the entropy as:

$$S_{A_B,f} = S(A_B, N \pm 1) \mp s_B - S(N) \quad 2.5$$

$E(A_B, N\pm1)$ is the entropy of a U_3Si_2 supercell that contains one defect of the type A_B, N is the number of atoms without the defect and N±1 is the number with the defect (interstitial = plus and vacancy = minus) while e_B is the partial energy of U or Si (interstitial = minus and vacancy = plus). $S(A_B, N\pm1)$ and s_B are the corresponding entropies. It should be noted that since U_3Si_2 is metallic, it was not necessary to take the charge state of the defect into consideration.

U anti-site defects were included in the calculations in this study because they have been shown to be important for non-stoichiometry in the U-rich part of the phase diagram [14]. The concentration of the Si anti-site defects was calculated to be less significant [14] and therefore were

not considered. For U anti-sites Eqs. 2.4 and 2.5 were slightly modified to include both the U and Si partial quantities with the number of atoms kept at the same number as the perfect cell (N):

$$E_{U_{Si},f} = E(U_{Si}, N) + e_{Si} - e_U - E(N) \quad 2.6$$

and

$$S_{U_{Si},f} = S(U_{Si}, N) + s_{Si} - s_U - S(N) \quad 2.7$$

Three different cases for the partial molar quantities (chemical potentials) were considered: 1) the environment is Si-rich and U_3Si_2 is in equilibrium with USi; 2) the environment is U-rich and U_3Si_2 is in equilibrium with U_3Si (at high temperature the equilibrium is with uranium metal); and 3) U_3Si_2 is near "perfect" stoichiometry. The stoichiometric or nearly stoichiometric case was bound by the chemical potentials of the Si and U-rich cases.

The partial energy and entropy were computed by solving the following equations:

$$E(U_aSi_b) = ae_U + be_{Si} \quad 2.8$$

$$E(U_cSi_d) = ce_U + de_{Si} \quad 2.9$$

and

$$\tilde{S}(U_aSi_b) = as_U + bs_{Si} \quad 2.10$$

$$\tilde{S}(U_cSi_d) = cs_U + ds_{Si} \quad 2.11$$

$E(U_aSi_b)$ and $E(U_cSi_d)$ are the energies of the U_aSi_b and U_cSi_d phases defining the equilibrium conditions. $\tilde{S}(U_aSi_b) = \frac{N}{N-1}S(U_aSi_b)$ and $\tilde{S}(U_cSi_d) = \frac{N}{N-1}S(U_cSi_d)$ are the corresponding entropies and N is the number of atoms in the cells used to describe U_aSi_b and U_cSi_d, respectively. The $\frac{N}{N-1}$ scaling factor is a consequence of the entropy of the crystalline solid summing over the 3(N-1) non-zero phonon modes, rather than the modes corresponding to the total number of atoms, 3N. The acoustic modes in the long wave-length limit, analogous to translation, are excluded from the summation.

2.2. Results

2.2.1. Rietveld Refinement and Crystal Structure of the $U_3Si_{2.00}$ and $U_3Si_{2.01}$

The goodness of fit (χ^2) and weighted profile factor (R_{wp}) values obtained from the simultaneous Rietveld refinement of the five histograms from the HIPPO detectors at each temperature for both $U_3Si_{2.00}$ and $U_3Si_{2.01}$ show that each refinement was successful using the U_3Si_2 (*P4/mbm*) crystal structure as the initial model (Table 3.2). The high-quality datasets have a larger χ^2 and R_{wp} values compared to the data collected for 120 minutes at the same temperature; Longer acquisition time increases the statistical precision in a diffraction measurement making it impossible to model "imperfections" in the peak shape or peak positions (i.e., features that cannot be modeled) [31].

A histogram recorded at ~298 K and 1298 K by the 145° and 90° detector panels of HIPPO, including Rietveld fit are provided in Figs. 2.2-2.4, 2.3 and 2.4 for $U_3Si_{2.00}$ and $U_3Si_{2.01,}$ respectively. The plots in Figs. 2.2-2.4 were normalized by the incident intensity and the refined background was subtracted for clarity. No additional U-Si phases were observed in either sample, indicating that both are single phase.

Table 2.2. The χ2 and Rwp obtained at each temperature for both samples.

Temperature [K]	χ^2 $U_3Si_{2.00}$	R_{wp} (%) $U_3Si_{2.00}$	χ^2 $U_3Si_{2.01}$	R_{wp} (%) $U_3Si_{2.01}$
298	51.79[b]	1.7533[b]	60.593[b]	1.71[b]
	3.528	0.82	6.589	1.01
373	3.050	0.76	5.746	0.95
473			5.835	0.95
573	2.685	0.72	4.820	0.97
673			4.843	0.88
773	2.339	0.68	4.211	0.84
873			4.439	0.84
973	2.136	0.66	4.032	0.82
1073			4.091	0.81
1198	1.907	0.65	3.800	0.80
1223	1.933	0.65	3.843	0.81
1248	1.924	0.64	3.700	0.81
1273	1.877	0.63	3.835	0.81
1273			3.803	0.80
1298	1.881	0.63	3.791	0.81
1323			3.841	0.81
1348			3.837	0.82
1373			3.925	0.86

[b] χ^2 and R_{wp} for high-quality data.

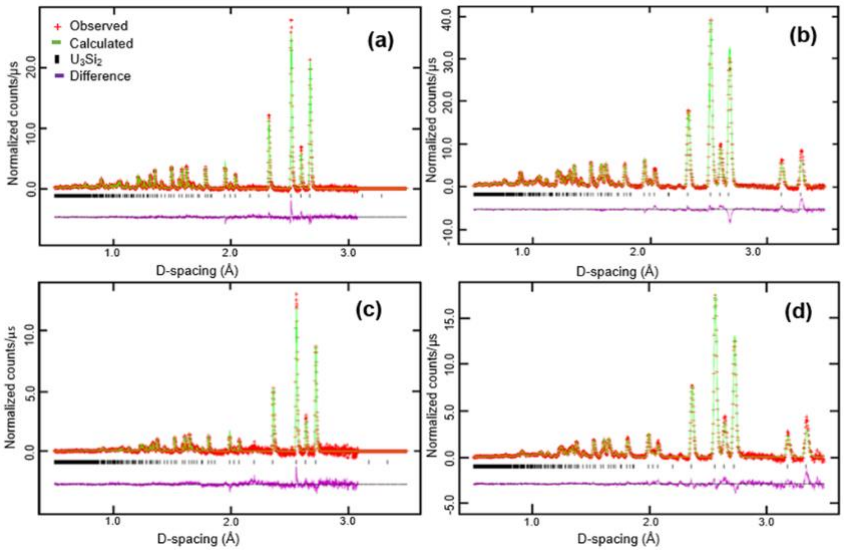

Fig. 2.2. Rietveld fit for $U_3Si_{2.00}$ sample at 298 K (a,b) and 1298 K (c,d) from the 145° (a,c) and 90° detector rings.

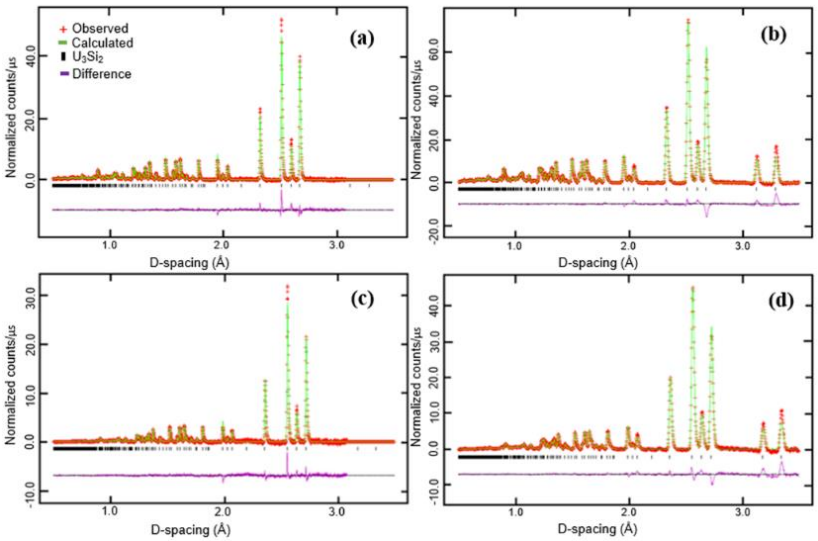

Fig. 2.3. Rietveld fit for $U_3Si_{2.00}$ sample at 298 K (a,b) and 1298 K (c,d) from 145°(a,c) 90° (b,d) detector rings.

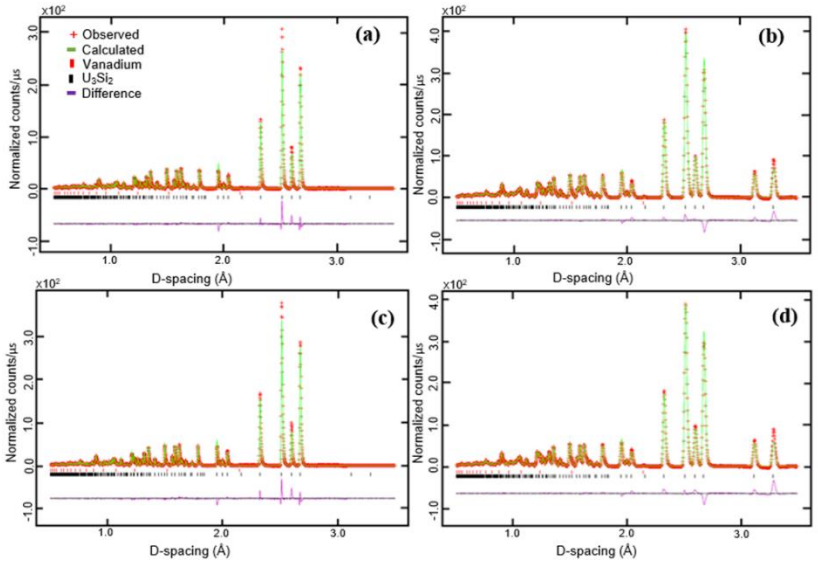

Fig. 2.4. Rietveld fit at 298 K high-quality data for $U_3Si_{2.00}$ (a, b) and $U_3Si_{2.01}$ (c, d) from the 145° (a, c) and 90° (b, d) detector rings.

The crystal structures based on the refined crystallographic parameters together with the densities above ~60% of the maximum density in the difference Fourier maps are shown in Fig. 2.5. The anisotropic atomic displacement parameters U_{ij} are displayed as 99% probability ellipsoids (i.e., covering the entire space of possible locations). The crystal structure contains two distinct uranium Wyckoff sites (2a and 4h) and one silicon site (4g). The uranium atom at the 2a position will be referred to as U1 and the one on the 4h as U2. While the U1 atom displays a strong anisotropic thermal displacement motion along the crystallographic c-axis (U_{33}), the Si and the U2 atoms exhibit an almost isotropic atomic displacement. The positive densities in the difference Fourier maps indicate the location of additional atoms.

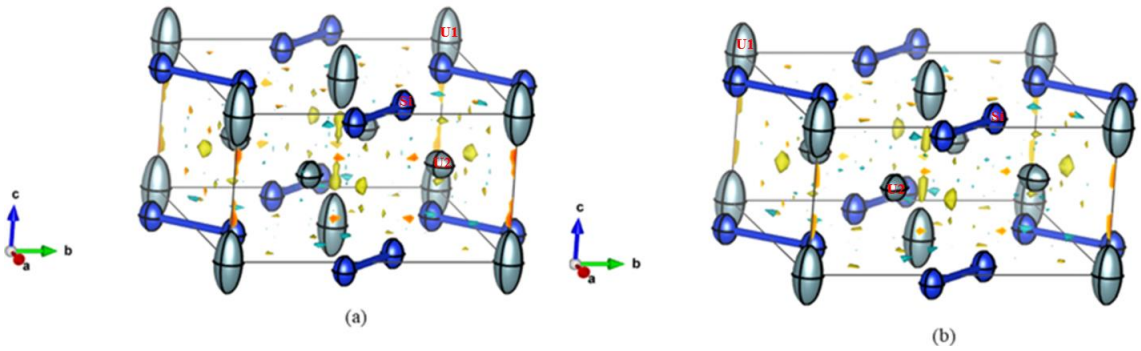

Fig. 2.5. Visualization of the refined crystal structure of $U_3Si_{2.00}$ (a) and $U_3Si_{2.01}$ (b) overlaid with the difference Fourier maps. Yellow shows a positive difference and blue a negative difference.

The atomic displacement parameters (U_{ij}) and the ratio of the atomic displacement parameter along the c axis to the atomic displacement parameter along the a axis (U_{33}/U_{11}) as a function of temperature are shown in in Fig. 2.6. For both samples a value of about 4.5 was obtained for U_{33}/U_{11}, showing that the thermal motion of the U1 atom is very anisotropic, with preferred motion along the c axis. The value of U_{33}/U_{11} varied between 0.96-0.85 and 1.6-1.2 over the entire temperature range for U2 and Si atoms respectively, showing that their thermal motion is almost isotropic, with the U2 atoms having a slightly preferred motion along the a axis, and the Si atoms having a slightly preferred motion along the c-axis.

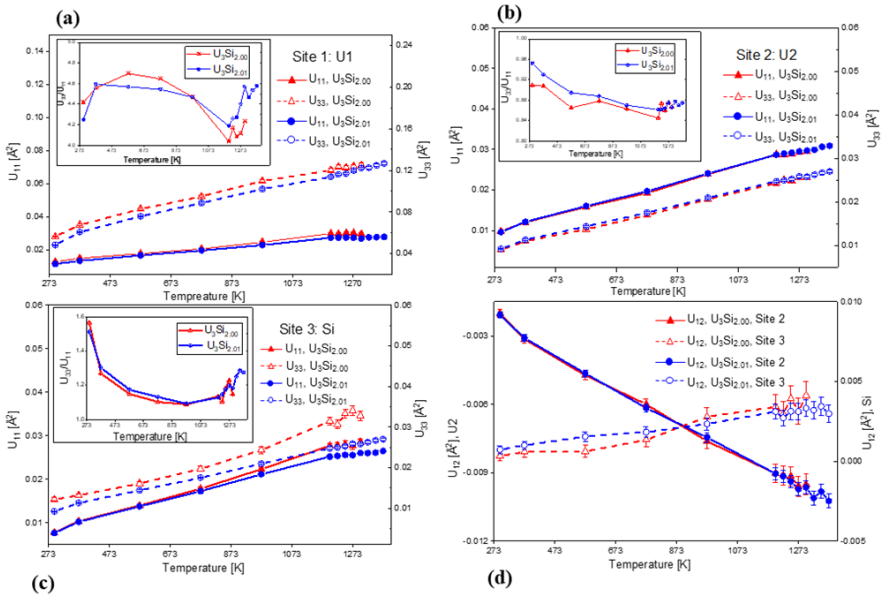

Fig. 2.6. Atomic displacement parameters U_{ij} as a function of temperature. All three atoms are shown in the $U_3Si_{2.00}$ (red) and $U_3Si_{2.01}$ (blue) crystal structure. U_{11} (left axis in a-c) and U_{33} (right axis in a-c) correspond to atomic displacement along the a-axis and c-axis, respectively and U_{12} (d) is the atomic displacement in the a-b plane for U2 (left axis in d) and Si (right axis in d). Note that the error bars are within the symbols and the scale difference in (a) and (d).

The lattice parameters and unit cell volume as a function of temperature for the two U_3Si_2 samples compared to parameters obtained by Obbard *et al*. [12] are shown in Fig. 2.7. While the a-lattice parameters lie within the margin error, the c-lattice parameters and therefore the unit cell volume for the $U_3Si_{2.01}$ sample resulted in slightly smaller values than the $U_3Si_{2.00}$ sample.

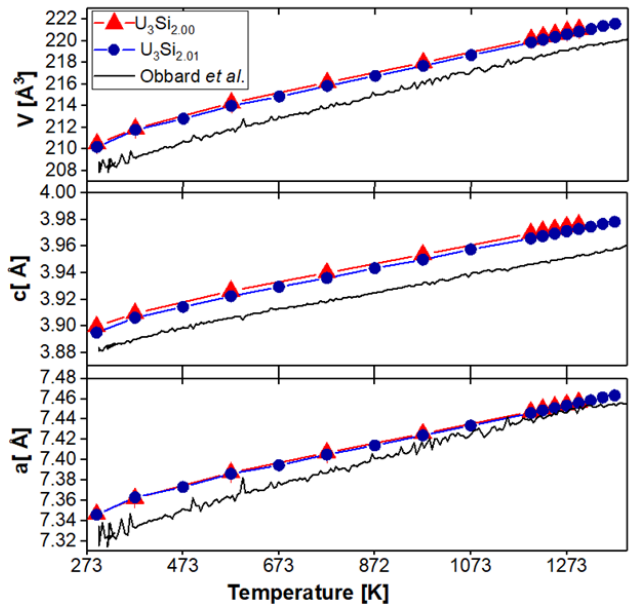

Fig. 2.7. Lattice parameters and unit cell volumes as a function of temperature. Stoichiometric $U_3Si_{2.00}$ is shown in red and hyper-stoichiometric $U_3Si_{2.01}$ in blue. Both are compared to data from [12] in black. The error bars for $U_3Si_{2.00}$ and $U_3Si_{2.01}$ are smaller than the data markers. Lattice parameters and unit cell volume were fit with a 2nd order polynomial with $R^2 > 0.997$.

Bond lengths were computed from the refined lattice parameters and atom positions, indicating Si-Si bonds are the shortest and that there are two symmetry related bond length possibilities for Si-U2 bonds. The uncertainties associated with the Si-Si bond lengths are higher than the uncertainties of the bond lengths and increases with temperature for both compositions. While the absolute bond lengths as a function of temperature displayed in Fig. 2.8 do not show significant trends, a plot of the relative bond lengths (Fig. 2.9) do reveal trends in behavior. The Si-Si bonds show the highest relative change (strain relative to the room temperature bond length) with greater than 2% at the highest temperatures for both compositions. In comparison, the Si-U1 bonds only expand slightly more than 1% during heating from room temperature to ~1273 K. The Si-Si bond strain at temperatures above 1000 K is greater in the $U_3Si_{2.01}$ greater sample.

There were no observable differences in the Si-U1 bond strains between the two samples. The U1-U2 thermal strain is significantly higher for the $U_3Si_{2.00}$ sample, resulting in a difference of 31% at 1298K. At temperatures above ~1200 K, the Si-U2 bond strains for the $U_3Si_{2.00}$ sample is either slightly higher or lower than that of the $U_3Si_{2.01}$ depending on the bond (the Si-U2 bond can be different depending on the plane of the Si atom).

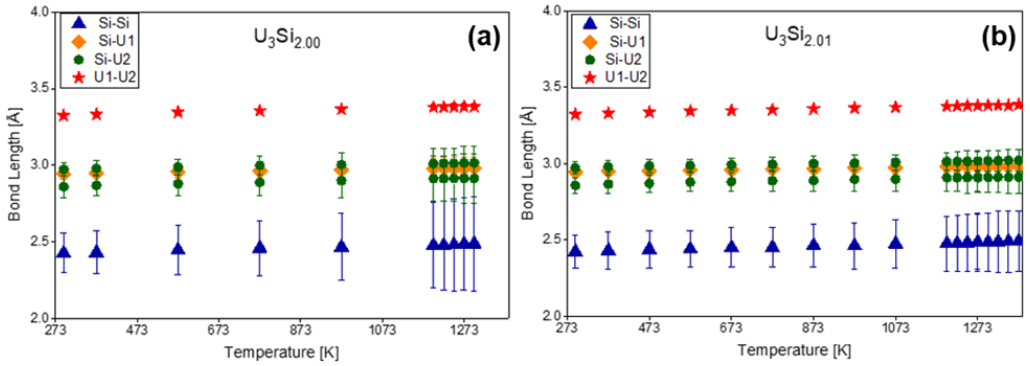

Fig. 2.8. Absolute bond lengths as a function of temperature for $U_3Si_{2.00}$ (a) and $U_3Si_{2.01}$ (b). For the U1-U2 bond the error bars are smaller than the data markers.

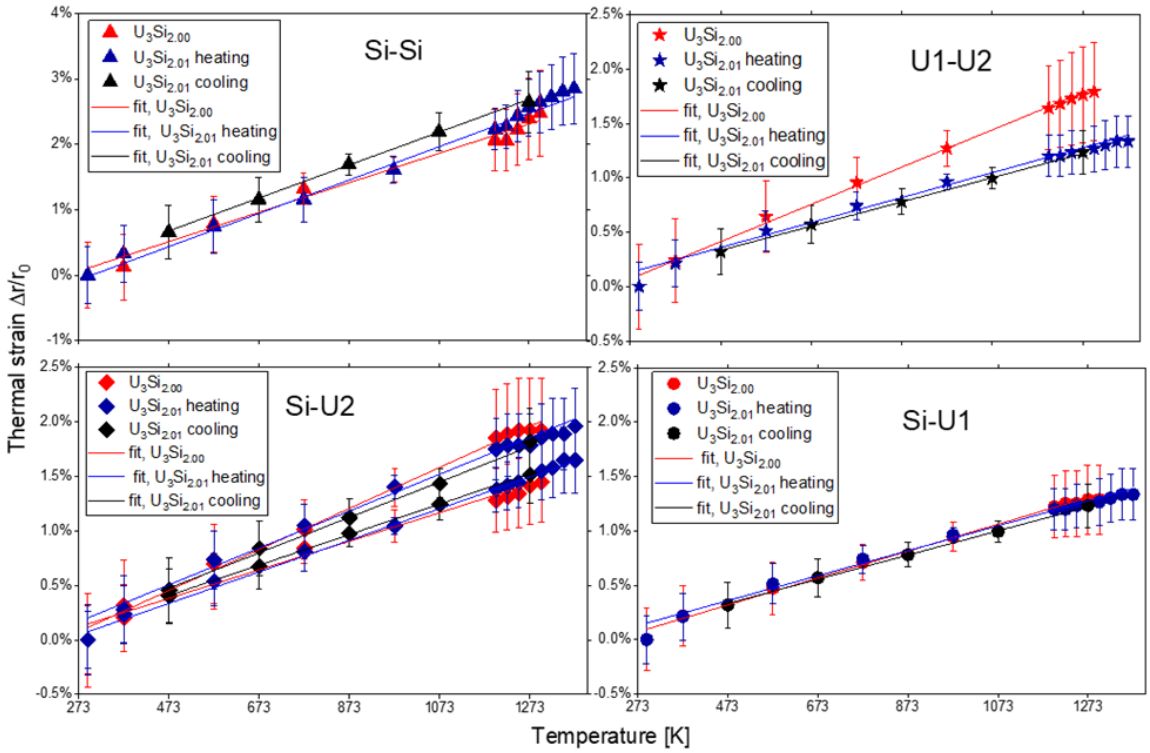

Fig. 2.9. Relative change of each bond lengths (thermal strain) as a function of temperature for $U_3Si_{2.00}$ compared to $U_3Si_{2.01}$. Note the difference in scale for the Si-Si bond.

2.2.2. Thermal Expansion of U_3Si_2 from Crystal Structure Data

The thermal expansion, and coefficient of thermal expansion (CTE) for each unit cell parameter were computed for both $U_3Si_{2.00}$ and $U_3Si_{2.01}$ samples and are shown in Fig. 2.10. The expansion of the a and c-lattice parameters from room temperature to 1273 K were ~1.5 % and ~2.2 %, respectively and is therefore significantly anisotropic. The thermal expansion of both the

a and c-lattices were greater for the $U_3Si_{2.00}$ compared to the $U_3Si_{2.01}$, by approximately 0.5 % and 1%, respectively.

The average linear coefficient of thermal expansion (α) is related to the volumetric coefficient of thermal expansion (β) by the equation:

$$(T) = 3\alpha(T) = \frac{1}{V}\frac{dV}{dT} = b_0 + b_1 T \qquad 2.12$$

where β(T) is the coefficient of volume expansion, α(T) is the average linear coefficient of thermal expansion, V is volume, and T is temperature. The average linear coefficient of thermal expansion is calculated using Eq. 2.12 by taking the derivative of the volumetric strain. The average CTE as a function of temperature for both samples compared to available literature values are provided in Fig. 2.11(a).

The recommended average CTE (Fig. 2.11b) for U_3Si_2 given by:

$$\alpha_{avg}(T) = 2.065 * 10^{-5} - 5.884 * 10^{-9} T \ (R^2 = 0.94) \qquad 2.13$$

and was computed using Regression analysis of the stoichiometric data from this work and those from White *et al.* [13] and Obbard *et al.* [12]. The data from the other studies shown in Fig. 2.11(a) were omitted from the computation for several reasons; 1) they did not follow the general trend (i.e., decrease as a function of temperature); 2) the values were too small compared to values from this work and those in references [12, 13]; and 3) uncertainties about their experimental procedures and sample composition.

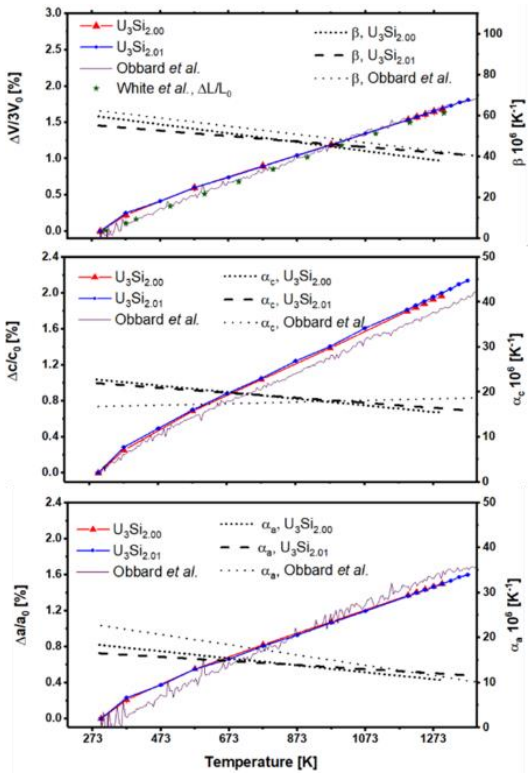

Fig. 2.10. Comparison of thermal expansion, coefficient of thermal expansion for a and c-lattice parameters, and unit cell volume. Collected data is compared with data from Obbard et al.[12]. Data from White et. at. [13] is also used for volumetric expansion comparison.

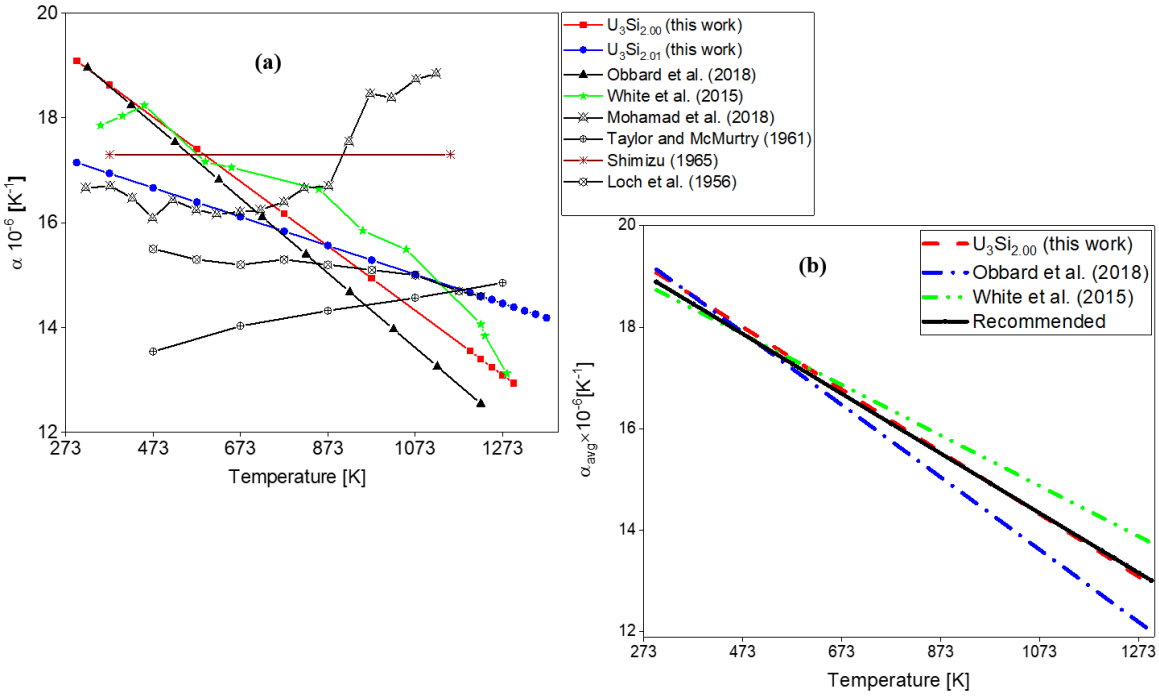

Fig. 2.11. (a) Average CTE for $U_3Si_{2.00}$ (red) and $U_3Si_{2.01}$ (blue) compared to literature CTE values [16, 72, 96-99]. (b) Recommended average CTE computed from $U_3Si_{2.00}$ (this work), Obbard et al. [12] and White et al. [13]. Note that in their work White et al. [13] used a constant to describe the CTE ($16.1x10^{-6}$ K^{-1} ± $1.3x10^{-6}$ K^{-1}). The $\alpha(T)$ provided in (b) was generated by a linear fit to the data in (a).

2.2.3. Results from DFT Calculations of Point Defects in U_3Si_2

The calculated point defect energies and entropies for the nearly stoichiometric, Si-rich and U-rich environments are provided in Table 2.3 and the point defect concentrations are plotted as function of temperature in Fig. 2.12 (near stoichiometric environment), Fig. 2.13 (Si-rich environment) and Fig. 2.14 (U-rich environment). The resulting non-stoichiometry (x in U_3Si_{2+x}) is also shown in the figures (Fig. 2.12-14).

Si interstitials dominate in all three environments, which leads to hyperstoichiometry with respect to Si for all three cases not only for Si-rich conditions. The hyperstoichiometry was accentuated at high temperature, while at low temperature the composition was close to stoichiometric. After Si interstitials, U anti-sites and U interstitials follow as the species with the second and third highest concentration. The U1 (2a site) vacancies had a more negative formation energy and therefore were more stable than the U2 (4h sites) vacancies. However, silicon vacancies are more stable than the U1, except for in the Si-rich environment when both are of similar magnitude. For U-rich environments at high temperature, the uranium anti-site concentration became significant and began to drive the non-stoichiometry back towards x = 0 (i.e., back to U_3Si_2).

Table 2.3. U and Si point defect formation energies and entropies.

	Energies (eV)				Entropies (k_B)		
	Stoich.	Si-rich	U-rich		Stoich.	Si-rich	U-rich
e_U	-9.79	-9.83	-9.79	s_U	-3.11	-1.30	-3.41
e_{Si}	-6.24	-6.19	-6.26	s_{Si}	-5.79	-8.05	-4.88
$E_{V_{U2a,f}}$	1.69	1.65	1.69	$S_{V_{U2a,f}}$	0.45	2.86	0.15
$E_{V_{U4h,f}}$	3.00	2.96	3.00	$S_{V_{U4h,f}}$	2.89	4.70	2.59
$E_{V_{Si,f}}$	1.79	1.84	1.77	$S_{V_{Si,f}}$	6.28	4.01	7.19
$E_{U_{i,f}}$	0.87	0.91	0.86	$S_{U_{i,f}}$	-3.15	-4.96	-2.85
$E_{Si_{i,f}}$	0.55	0.50	0.57	$S_{Si_{i,f}}$	2.19	4.45	1.28
$E_{U_{Si,f}}$	1.02	1.11	1.00	$S_{U_{Si,f}}$	1.32	-2.75	2.53

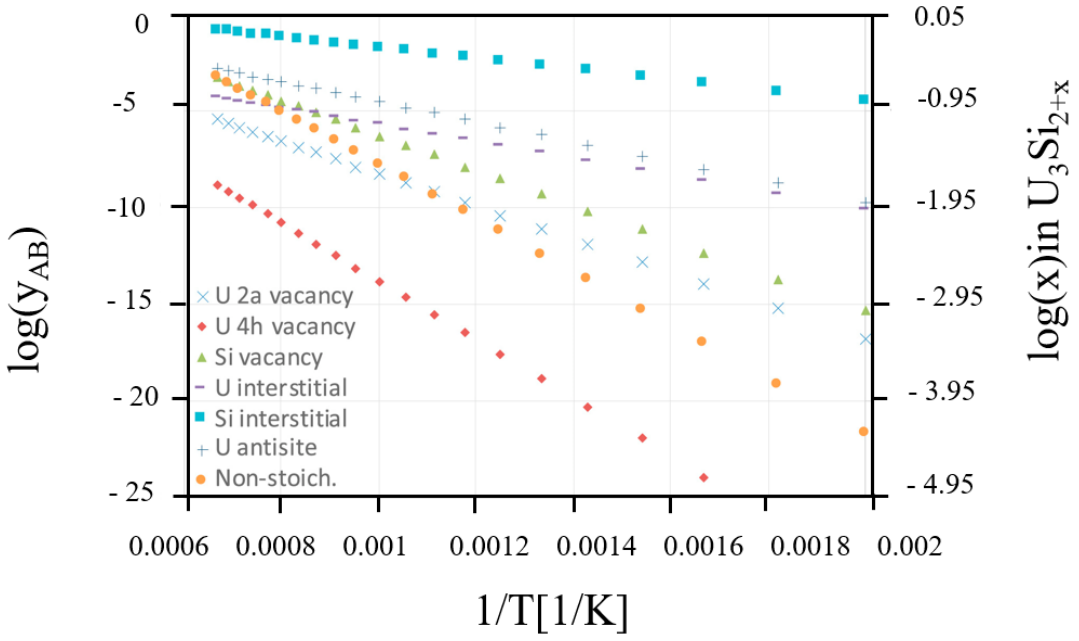

Fig. 2.12. Equilibrium defect concentrations (plotted as site fractions, y_{AB}, left) and non-stoichiometry (x, right) for nearly stoichiometric U_3Si_2.

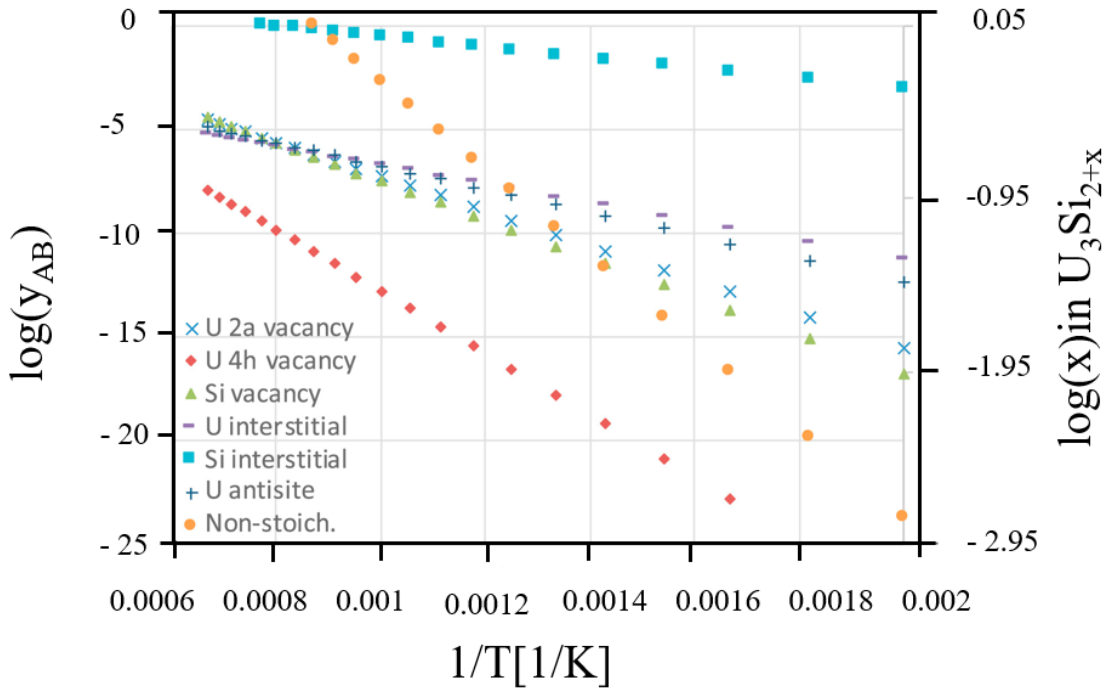

Fig. 2.13. Equilibrium defect concentrations and non-stoichiometry in U_3Si_{2+x} for Si-rich equilibrium. Equilibrium defect concentrations are plotted as site fractions, y_{AB}, on the left-hand axis and non-stoichiometry, x, is plotted on the right-hand y-axis.

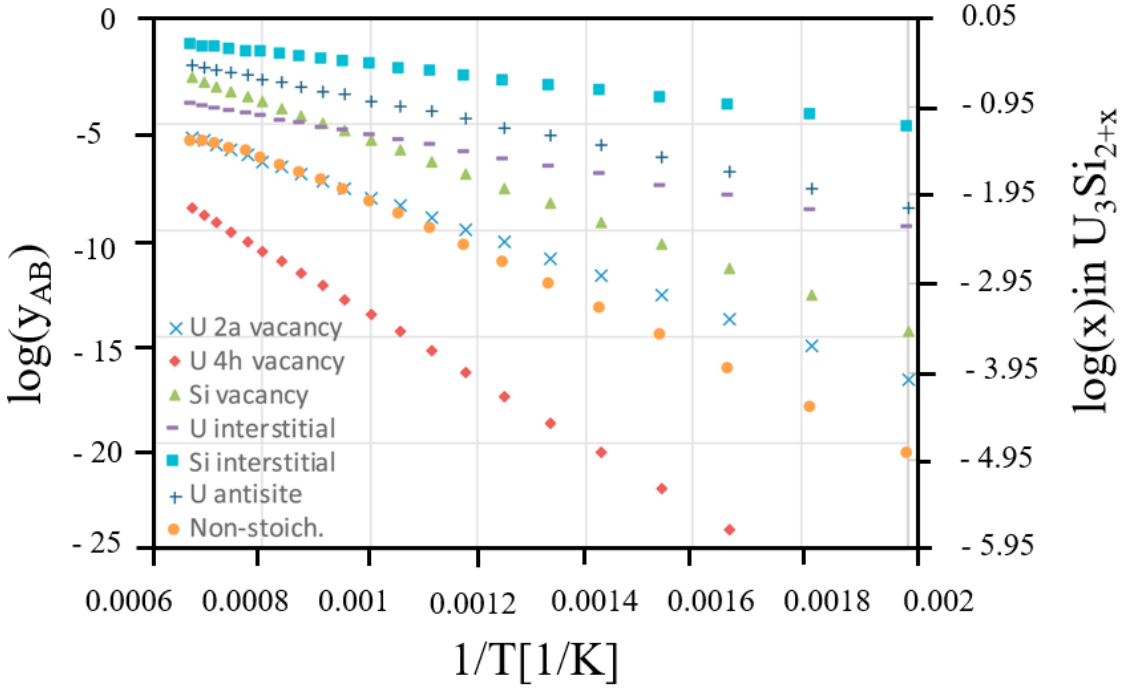

Fig. 2.14. Equilibrium defect concentrations and non-stoichiometry in U_3Si_{2+x} for U-rich equilibrium. Equilibrium defect concentrations are plotted as site fractions, y_{AB}, on the left-hand y-axis and non-stoichiometry, x, on the right-hand y-axis.

2.3. Discussion

2.3.1. Non-Stoichiometry in U_3Si_2 form Si Interstitial Defect

The slightly higher Si content sample ($U_3Si_{2.01}$) has not resulted in an expected second phase when assuming U_3Si_2 is a line compound. This suggests the current phase diagram may not have a sufficiently wide homogeneity range of U_3Si_2 to accommodate current observations. The lack of any secondary phase at temperatures below 1000 K, disagrees with the prediction made by Middleburg *et al.* [14], however they do agree with prediction made here by adding entropic contributions to the analysis of Middleburgh *et al*. [14].

The decrease in the lattice parameters (~0.01% and ~0.1% for a and c-lattices respectively), the observed differences in the thermal strain (Fig. 2.10), atomic displacement parameters (Fig. 2.6), bond length strain (Fig. 2.10) and coefficients of thermal expansion (Fig. 2.11) for $U_3Si_{2.00}$ compared to $U_3Si_{2.01}$ support the conclusion that the extra Si dissolved in the U_3Si_2 lattice because an undetected secondary phase would have resulted in identical structural evolution of U_3Si_2 for both samples. The positive difference in the difference Fourier maps (Fig. 2.5) allow to locate the 4f, 2c and 2d as possible silicon sites. Those sites along with 6 other (2b, 4e, 4g, 4h,8i) Wyckoff positions were tested to identify the most stable silicon interstitial site. Fractional amount of Si atom was added to each site and Rietveld refinement was performed on the high-quality data for $U_3Si_{2.01}$ as described in Section 3.3. The total amount of silicon was constrained to 2.01, and the regular silicon site and the interstitial site occupancies could vary during refinement. The results from the Rietveld refinements are Summarized Table 2.4.

Table 2.4. Summary of Rietveld refinement results at 298 K.

Wyckoff site	**Position**	χ^2	R_{wp} **(%)**	**Initial Si Site Fraction**	**Refined Si Site Fraction**	**Lattice Parameter**
8i	0.75, 0.2, 0	diverged	diverged	0.00125	diverged	diverged
4e	0.5, 0.5, 0.262(2)	56.99	1.66	0.0025	0.026(1)	a = 7.34097(7) Å c = 3.89378(5) Å
4f	0, 0.5, 0.25	diverged	diverged	0.0025	diverged	diverged
4g	0.48, 0.98, 0	diverged	diverged	0.0025	diverged	diverged
4h	0.47, 0.97, 0.5	diverged	diverged	0.0025	diverged	diverged
2b	0.5, 0.5, 0.5	57.51	1.66	0.005	0.043(2)	a = 7.34094(7) Å c = 3.89384(5) Å
2c	0.5, 0, 0.5	59.53	1.69	0.005	0.008(1)	a = 7.34103(7) Å c = 3.89378(5) Å
2d	0, 0.5, 0	diverged	diverged	0.005	diverged	diverged

Results show that the 4e, 2b, and the 2c could be a possible interstitial silicon site, with the 4e site being the most probable. The 4e site was not considered as an interstitial site in DFT calculations; however, it closely relates to the substitutional anti-site solution mechanism investigated by Middleburgh *et al*. [14]. The 2b site (0,0, 0.5) was predicted to be the most stable for interstitial Si atoms by DFT simulations. The position was predicted to be slightly displaced from the actual (0.0, 0.0, 0.5) position, which relates to the 4e site (0, 0, ±z). Therefore, the experimental and DFT predictions are in agreement regarding the stable silicon interstitial site.
The Si interstitial defect extends over the entire temperature range studied for the $U_3Si_{2.01}$ sample. Therefore, the U_3Si_2 compound should not be represented as a line compound but instead a solid

solution. Future work is warranted to study additional $U_3Si_{2\pm x}$ to discover the width of the homogeneity range.

2.3.2. Lattice Parameters of Stoichiometric and Non-stoichiometric U_3S_2 Phase

All refinements showed an excellent agreement with the reported U_3Si_2 crystal structure. For the stoichiometric $U_3Si_{2.00}$ sample the lattice parameters were 7.34664(7) Å and 3.89965(6) Å for the a-lattice and c-lattice respectively at 298 K (values taken from the Rietveld refinement of the 120-minute count time data). The lattice parameters were within 0.4 % of the data by Remschnig *et al.* [10] (a = 7.336(5) Å, c = 3.890(8) Å), Maskova *et al.* [32] (a = 7.336(4) Å, c = 3.892(6) Å), Mohamad *et al.* [33] (a = 7.32(1) Å, c = 3.90(9) Å) and Obbard *et al.*[12] (a = 7.324(3) Å, c = 3.882(2) Å). The lattice parameters obtained for hyperstoichiometric $U_3Si_{2.01}$ at ambient temperature are 7.34589(4) Å and 3.89513(5) Å for the a-lattice and c-lattice, respectively. This would indicate Si atoms substituting for U atoms as interstitial locations of excess Si would lead to a lattice expansion rather than a contraction.

The DFT calculations of non-stoichiometry in U_3Si_2 indicated that the interstitial defect mechanism for accommodating excess silicon in the crystal structure is the most favored. The simulated structure with excess silicon atoms on the interstitial sites shows that the a-axis contracted by 0.097%, while the c-axis expanded by 0.35% and the overall unit cell expanded by 0.15%. Even though the volume expansion and the change in lattice parameters were small, the simulation results exhibited a slightly different trend than the neutron diffraction measurements. This could be related to the higher defect concentration used in the simulation, finite temperature effects not accounted for in the simulations, or a structural difference between simulations and experiments.

The silicon substitutional defect mechanism was predicted to be less stable than the interstitial mechanism by Middleburgh *et al.* [14] and consequently was not included in the initial analysis of this work. In view of the experimental results, additional calculations were performed following the methodology in Section 3.3.4. Those calculations concluded that the substitutional mechanism would cause a contraction of the parameters. It was found that the substitutional mechanism lead to a lattice contraction of 0.22% for $U_3Si_{2.11}$. The difference between the two mechanisms was significant, but only 0.02eV.

Another possibility suggested and investigated by Andersson [private communication] is the ability of forming a bound cluster from an interstitial and substitutional Si atom. It was found that even though the cluster was weakly bound (-0.37 eV), it still caused volume expansion of the lattice. Investigations of the accommodation of excess Si atoms will be the subject of future research.

2.3.3. Thermal Expansion of U_3Si_2

The volumetric expansion relative to the room temperature volume to 1273 K was found to be 1.65(6) % and 1.65(5) % for $U_3Si_{2.00}$ and $U_3Si_{2.01}$, respectively. This is in good agreement with results by White *et al.* [13], who found the thermal expansion of ~1.589% at 1273 K for U_3Si_2 from dilatometry measurements and by Obbard *et al.* [12], who calculated a volumetric thermal expansion of ~1.662% at 1273 K for U_3Si_2 from neutron diffraction refinement. The expansion of the a and c-lattice parameters from room temperature to 1273 K were 1.5 and 2.2 %, respectively and is therefore significantly anisotropic. This indicates that the existence of preferred orientation in a U_3Si_2 fuel pellet could lead to anisotropic thermal expansion of the bulk, which in turn could lead to cracking.

The average CTE for both $U_3Si_{2.01}$ and $U_3Si_{2.00}$ was found to vary linearly with temperature and decrease with increasing temperature. The CTE values for $U_3Si_{2.00}$ varied more widely with temperature with a greater slope as compared to $U_3Si_{2.01}$.

The CTE values for $U_3Si_{2.01}$ also agrees well with those of Loch *et al*. [34] and values obtained by Mohamad *et al*. [33] from 273-800 K, above which their values started to increase with temperature. Although Mohamad *et al*. [33] did not mention anything about their samples oxidizing, with the good agreement between their data and Taylor and McMurtry [35], it can be speculated that their sample oxidized at some point during their analysis. The CTE values reported by Taylor & McMurtry [35] were significantly lower than that for $U_3Si_{2.01}$ and $U_3Si_{2.00}$ and their values increased with temperature. These results were associated with the oxidation of their samples during analysis. From this work it is evident that composition and sample environment plays a role in the accuracy of CTE value obtained for U_3Si_2.

The CTE values for $U_3Si_{2.00}$ agreed well with those reported by Obbard *et al*. [12]. Although White *et al*. [13] reported a constant CTE value, a linear fit to their data was done in this work that agreed well with the $U_3Si_{2.00}$ values. The CTE for U_3Si_2 is best describe by the line $\alpha_{avg}(T) = 2.065 * 10^{-5} - 5.884 * 10^{-9}T$ ($R^2 = 0.94$).

3. Phase Stability of U_5Si_4, USi, and U_2Si_3

The gaps and uncertainties in understanding of U-Si phase relations and thermodynamic representations are especially a problem for the Si-rich region where many questions had remained [24, 36, 37]. The extant phase diagram [37] indicates seven intermetallic compounds; USi_3 (Cu_3Au-type), USi_2, $USi_{1.88}$ (defect $ThSi_2$-type), U_3Si_5 (defect AlB_2-type), USi (USi-type), U_3Si_2 (U_3Si_2-type) and U_3Si. The phase represented as U_3Si_5 was previously identified as U_2Si_3 by Kaufmann et al., [13[38] or β-USi_2 by Zachariasen [19]. In 1959, Brown and Norreys [39] suggested that the U_2Si_3 phase was a modification of the α-USi_2 phase; however, the composition was located between 62-63 at.% silicon (U_3Si_5).

In 1998, Noel et al. [40] reported a new phase, U_5Si_4, having a hexagonal unit cell (*P6/mmm* space group) with lattice parameters a=10.468 Å and c=3.912 Å. Although the work of Noel et al. [40] presents a full crystallographic description, the reported data are limited, and the X-ray diffraction (XRD) pattern has never been reported. Berche et al. [37] and Hoggan et al. [41] also reported a U_5Si_4 phase based on scanning electron microscopy (SEM) backscatter images and energy-dispersive X-ray spectroscopy (EDS) analysis. Considering the observed microstructure, Berche et al. [37] proposed that the U_5Si_4 phase is formed through a peritectic reaction [U_3Si_2 + liquid → U_5Si_4], however they could not determine the temperature of the peritectic transition using their differential thermal analysis (DTA) technique. As no events were observed in the DTA measurements, the phase was not included in their thermodynamic assessment. The U_5Si_4 phase was considered in the thermodynamic assessment performed by Wang et al. [24], but due to the limited experimental data, no crystal structure model was provided, and the Neumann-Kopp rule was used to describe the formation enthalpy, entropy, and heat capacity. It was emphasized by Wang et al. [24] that more work is still required to confirm the stability of the U_5Si_4 phase. Previous density functional theory calculations with a Hubbard correction (DFT+U) for the U_5Si_4 phase using the structure reported by Noel et al. [40] have found that the phase is stable with respect to the decomposition reaction $U_5Si_4 \rightarrow 2USi + U_3Si_2$, requiring only 0.02 eV more positive energy to cause decomposition [14, 15, 22, 42]. Middleburgh et al.[14] have further pointed out that the small energy of formation barrier could be negated by entropic factors, thus no conclusion was made about U_5Si_4 phase stability. This present work is aimed at contributing to the solution of this issue.

As USi is compositionally adjacent to U_3Si_2 and U_3Si_5, USi could be a potential minor phase generated in silicide fuel during fabrication or as uranium is consumed under irradiation and therefore, understanding the phase is important. The primary concern about the USi phase is its crystal structure, there are four proposed structure in the literature [19, 22, 42-44]. Bihan et al. [44] found that the USi phase exhibits a tetragonal structure (*I4/mmm* space group) and inferred that the USi crystal structure with *Pbnm* space group reported by Zachariasen [19] was not the equilibrium structure because it was oxygen stabilized (U_8Si_8O). DFT calculations by Noordhoek et al. [45] demonstrated that neither of these USi structures are the most stable, but instead suggested that USi is orthorhombic adopting the *Imma* space group. Further DFT work by Lopes et al. [22] and Kocevski et al. [42] showed that USi with the *Cmcm* space group is the most stable structure. Kocevski et al. [42] further showed that USi with the *Imma* structure is less stable than the *Pnma* phase. In this work neutron diffraction is used to characterize the USi phase, previous experiments by Ulrich et al. [46] and Obbard et al. [12], showed that this technique can sufficiently characterize atom positions, thermal motion and anisotropic coefficient of thermal expansion.

3.1. Methodology

3.1.1. Sample Fabrication

Three samples with nominal compositions of U/Si = 5/4, U/Si =1/1, and U/Si = 2/3, were prepared by arc melting uranium and silicon using a tri-arc furnace (5 TA Reed Tri Arc, Centorr Vacuum Industries, USA). The arc melter was equipped with non-consumable 2% thoriated tungsten electrodes and a water-cooled copper hearth. Arc melting was conducted under an atmosphere of high purity, gettered argon. The depleted uranium rods (99.9+% purity, AeroJet Rocketdyne, Jonesborough, TN, USA) were manually

cleaned using a SiC grinding disc to remove the oxide layer and rinsed with acetone and methanol before being weighed. Chemical analysis on the uranium feedstock using Inductively Coupled Plasma-Mass Spectrometry (ICP-MS) by MCL Inc. (Oak Ridge TN) revealed 8.3 ppm Co, 3.6 ppm Ni, and 2.7 ppm Cu impurities. All other transition metals and rare earth impurities were below the instrument's detection limit of 0.05 ppm. Silicon with 99.999% purity (irregular shaped pieces, 3-6mm in size, Cerac Inc., Milwaukee, WI) was used. A 5 mg excess of Si was added to each sample before arc melting to compensate for expected Si volatilization.

Arc melting was conducted in an inert glovebox where the oxygen and water concentration were less than 0.1 ppm. The O_2 concentration at the inlet and outlet of the arc melting system was monitored with oxygen sensors (Rapidox 3100 OEM, Cambridge Sensotec, UK) and the oxygen level was less than 10^{-15} ppm before the start of each sample melt. Each ingot was remelted 5 times, being turned over after each melt to ensure homogeneity. Compositions were calculated based on mass difference assuming that any mass loss was due to silicon volatilization. Targeted and actual compositions of the cast ingots are summarized in Table 3.1.

Table 3.1. Target and actual compositions of samples along with identified phases and lattice parameters. The space group and lattice parameters for the identified phases are compared to those from Remschnig et al. [47] and Bihan et al. [44].

Target U/Si	Actual U/Si	Target at.% Si	Actual at.% Si	[1]Identified Phases	Space Group	Lattice Parameters (Å)			Reference
						a	b	c	
5/4	5/4.23	44.44	45.83	U_3Si_2	*P4/mbm*	7.32(4) 7.33(5)	7.32(4) 7.33(5)	3.90(2) 3.89(8)	This Work [22]
				USi ($U_{34}Si_{34.5}$)	*I4/mmm*	10.60(8) 10.58(3)	10.60(8) 10.58(3)	24.34(2) 24.34(2)	This Work [22]
2/3	2/3.36	60.00	63.69	USi ($U_{34}Si_{34.5}$)	*I4/mmm*	10.59(1) 10.58(3)	10.59(1) 10.58(3)	24.39(5) 24.31(5)	This Work [22]
				U_3Si_5	*P6/mmm*	3.84(1) 3.84(7)	3.84(1) 3.84(7)	4.06(2) 4.08(1)	This Work [22]
1/1	1/0.98	50.00	49.49	USi	*I4/mmm*	10.622(1) 10.587(3)	10.622(1) 10.587(3)	24.389(7) 24.310(5)	This work [30]

[1]The phase identified for the U/Si = 5/4 and U/Si = 2/3 samples were done by XRD while that for the U/Si = 1/1 was done by neutron diffraction.

Pieces of the ingots from the U/Si = 5/4.23 and U/Si = 2/3.36 samples were annealed in a W-mesh metal furnace in a glovebox for 48 hours at 1250 °C under a flowing gettered Ar with a heating rate of 20 K min^{-1} and a cooling rate of 100 K min^{-1}.

The U/Si = 1/0.98 sample was prepared for neutron diffraction by grinding the ~5 g ingot using a mortar and pestle and sieving between a -200 and -325 mesh in an Ar glovebox maintained below 30 ppm O_3. Immediately after grinding, the sample was placed in a W-mesh metal furnace and annealed at 1250 °C for 20 hours under flowing gettered argon. The shorter annealing time has been shown to be sufficient for equilibrating the silicides post size reduction [46]. Immediately following annealing the sample was loaded into a vanadium container to limit oxygen exposure.

3.1.2. SEM-EDS and XRD

Samples for SEM-EDS were prepared by mounting 3-5 pieces of an ingot in epoxy and polishing them using #600, #800, #1200 grit SiC grinding discs and then using 9 μm, 3 μm, and 1 μm diamond suspension for final polishing. A Tescan Vega-3 SEM equipped with an electron backscatter and an EDS detector was used for imaging and analyzing phase composition. Fiji (ImageJ) software was used to compute the volume fraction of each phase from the backscatter images of the annealed sample.

XRD samples were prepared by grinding ingot fragments using a mortar and pestle in the Ar atmosphere glovebox previously described. An approximately 100 mg powdered sample was mounted on a Si single-crystal zero-background plate using a thin layer of vacuum grease and sealed inside a polymer dome inside the glovebox to reduce the risk of oxidation. The polymer dome had an air scatter shield to minimize the background contribution to the diffraction signal. XRD spectra were collected on a Bruker X-ray diffractometer (D2 Phaser, Bruker AXS, Madison, WI, USA), from 15° to 90° 2θ with a 7s dwell time and a 0.01° step size. The XRD patterns were analyzed using Bruker DIFFRAC.SUITE EVA software, and MDI Jade pro software. The phase fractions of the annealed samples were estimated by whole pattern function (WPF) Refinement with the reference intensity ratio (RIR) method implemented in the Jade software. Rietveld analysis on the XRD data was performed using the GSAS-II software package to determine lattice parameters.

3.1.3. High Temperature Time-of-Flight Neutron Diffraction

The High Pressure-Preferred Orientation (HIPPO) time-of-flight neutron diffractometer, utilizing the pulsed neutron spallation source at the Los Alamos Neutron Science Center, was used for neutron diffraction measurements. An Institute Laue-Langevin (ILL)-type furnace with vanadium heating elements and heat shields and operated at a vacuum of $<10^{-4}$ Pa was used for controlling sample temperature.

Neutron diffraction measurements were recorded every 200 °C as the temperature increased from room temperature to 1100 °C with a temperature dwell time equivalent to 120 minutes at 100 μA proton current to compensate for fluctuations in proton current (Table 3.2). Data were recorded at ~30 °C, 100 °C, 300 °C, 500 °C, 700 °C, 900 °C, and 1100 °C, as the sample was heated and at 1000 °C, 800 °C, 600 °C, and 400 °C, as the sample cooled.

Rietveld analysis on the neutron diffraction data was performed using the GSAS software with scripts written in gsaslanguage. The USi structure belonging to the *I4/mmm* space group as reported by Bihan et al. [44] was used as the initial model. The room temperature structure was subsequently used to refine the high temperature data, where the maximum number of parameters was 103, including background parameters, diffractometer constants, lattice parameters, isotropic displacement parameters for Si atoms, anisotropic displacement parameters for U atoms (constrained to be constant for each atom), atomic positions, peak width parameters, absorption parameters, and atom site occupation parameters for the Si atoms.

Table 3.2. Neutron diffraction data temperatures, goodness of fit (χ2), and the weighted profile factor (R_{wp}).

Temperature [°C]	U/Si = 1/0.98	χ^2	R_{wp} (%)
30	Heating	14.77	1.05
100	Heating	9.683	0.84
300	Heating	8.491	0.81
400	Cooling	5.177	0.85
500	Heating	10.78	0.91
600	Cooling	8.538	0.80
700	Heating	7.533	0.76
800	Cooling	7.743	0.77
900	Heating	7.036	0.74
1000	Cooling	7.002	0.74
1100	Heating	6.331	0.72

3.2. Results

3.2.1. U_5Si_4 and U_2Si_3

The samples with compositions U/Si = 5/4.23 (45.83 at.% Si) and U/Si = 2/3.36 (63.69 at.% Si) were used to investigate the existence of the U_5Si_4 and the U_2Si_3 phases. Representative SEM backscatter images of the as-cast and annealed samples are provided in Figs. 3.1-3. They indicate two phases are present; a Si-rich phase and a U-rich phase, identified as $USi_{0.9}$ and $U_3Si_{1.9}$ in the U/Si = 5/4.23 sample and $USi_{1.7}$ and $USi_{1.0}$ in the U/Si = 2/3.36 sample based on EDS analysis. The elemental analyses are summarized in the supplementary material (Table 3.3**)**. The phase fractions for $USi_{0.9}$, $U_3Si_{1.9}$, $USi_{1.7}$ and $USi_{1.0}$ were calculated as approximately 60 mol%, 40 mol%, 80 mol% and 20 mol%, respectively from SEM backscatter images.

The XRD patterns for the as-melted and annealed U/Si = 5/4.23 sample are provided in Fig. 3.3. The U_3Si_2 (*P4/mbm* space group) and USi (*I4/mmm* space group) were identified as the two phases present with no additional phases indicated by additional diffraction peaks. The XRD pattern of the annealed U/Si = 2/3.36 sample (Fig. 3.4) indicate solely the $USi_{1.67}$ (*P6/mmm* space group) and USi (*I4/mmm* space group) phases. The U/Si = 5/4.23 sample is composed of ~39 mol% U_3Si_2 and ~61 mol% USi determined using RIR method with the MDI JADE software. The U/Si = 2/3.36 sample has a phase fraction of ~19 mol% USi and ~81 mol% $USi_{1.67}$, respectively. The phases, space groups and lattice parameters found from Rietveld refinement are compared to those previously reported by Remschnig et al. [47] (Table 3.1).

Table 3.3. EDS data for the 45.83 at.% Si and 62.69 at.% Si samples.

45.83 at.% Si Sample (Phase 1)	**at.% Si**	**at.% U**	**wt.% Si**	**wt.% U**
	48.05	51.95	9.84	90.12
	47.86	52.14	9.77	90.23
	48.12	51.88	9.86	90.14
	47.76	52.24	9.74	90.26
	48.42	51.58	9.97	90.03
	48.01	51.99	9.83	90.17
	45.65	54.39	9.02	90.98
	45.79	54.21	9.06	90.94
	47.50	52.50	9.65	90.35
	47.68	52.32	9.71	90.29
	48.41	51.59	9.97	90.03
	47.48	52.52	9.64	90.36
	47.70	52.30	9.71	90.29
Average	**47.7±0.8**	**52.4±0.8**	**9.7±0.3**	**90.3±0.3**
45.83 at.% Si Sample (Phase 2)	**at.% Si**	**at.% U**	**wt.% Si**	**wt.% U**
	39.10	60.90	7.04	92.26
	39.38	60.62	7.12	92.88
	38.80	61.20	6.96	93.04
	39.78	60.22	7.23	92.77
	38.81	61.19	6.96	93.04
	39.30	60.70	7.10	92.90
	39.77	60.23	7.23	92.77
	38.39	61.61	6.85	93.15
	38.63	61.37	6.91	93.09
	39.31	60.69	7.10	90.90
	39.77	60.23	7.23	92.77
Average	**39.19±0.46**	**60.81±0.46**	**7.24±0.59**	**92.69±0.60**
62.69 at.% Si Sample (Phase 1)	**at.% Si**	**at.% U**	**wt.% Si**	**wt.% U**
	62.55	37.45	16.47	83.53
	62.45	37.55	16.41	83.59
	62.51	37.39	16.5	83.5
	62.89	37.11	16.66	83.34
	62.88	37.12	16.66	83.34
	62.59	37.41	16.49	83.51
	62.59	37.41	16.9	83.51
	63.09	36.91	16.78	83.22
	63.32	36.68	16.98	83.08
	63.25	36.75	16.88	83.12
	62.95	37.07	16.70	83.30
	62.7	37.30	16.55	83.50
	62.55	37.45	16.46	83.54
	62.27	37.73	16.3	83.70
	63.15	36.85	16.82	83.18
	63.16	36.84	16.83	83.17
Average	**62.81±0.31**	**37.19±0.31**	**16.65±0.20**	**83.38±0.20**
62.69 at.% Si Sample (Phase 2)	**at.% Si**	**at.% U**	**wt.% Si**	**wt.% U**
	49.83	50.17	10.49	89.51
	50.30	49.70	10.67	89.33
	49.95	50.05	10.53	89.47
	50.15	49.85	10.61	89.39
	50.50	49.50	10.75	89.25
	49.46	50.54	10.35	89.65
	50.78	49.22	10.85	89.15
	50.57	49.43	10.77	89.23
	50.34	49.66	10.68	89.32
	50.46	49.54	10.73	89.27
	50.47	49.33	10.84	89.19
	50.81	49.19	10.86	89.14
	49.99	50.01	10.55	89.45
	50.66	49.34	10.81	89.19
	49.65	50.35	10.42	89.58
	50.57	49.43	10.77	89.23
Average	**50.28±0.39**	**49.71±0.40**	**10.67±0.15**	**89.33±0.15**

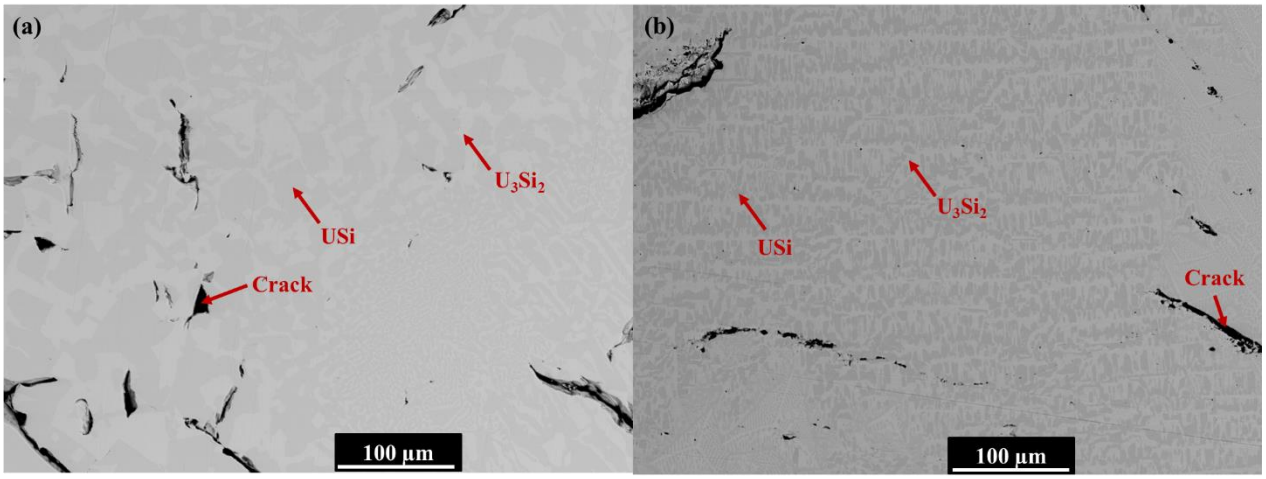

Fig. 3.1. SEM backscatter images of the U/Si = 5/4.23 sample. The as-cast (a) and annealed (b) sample. Magnification 500x and an acceleration voltage of 20.0kV. Phases identified by EDS analysis.

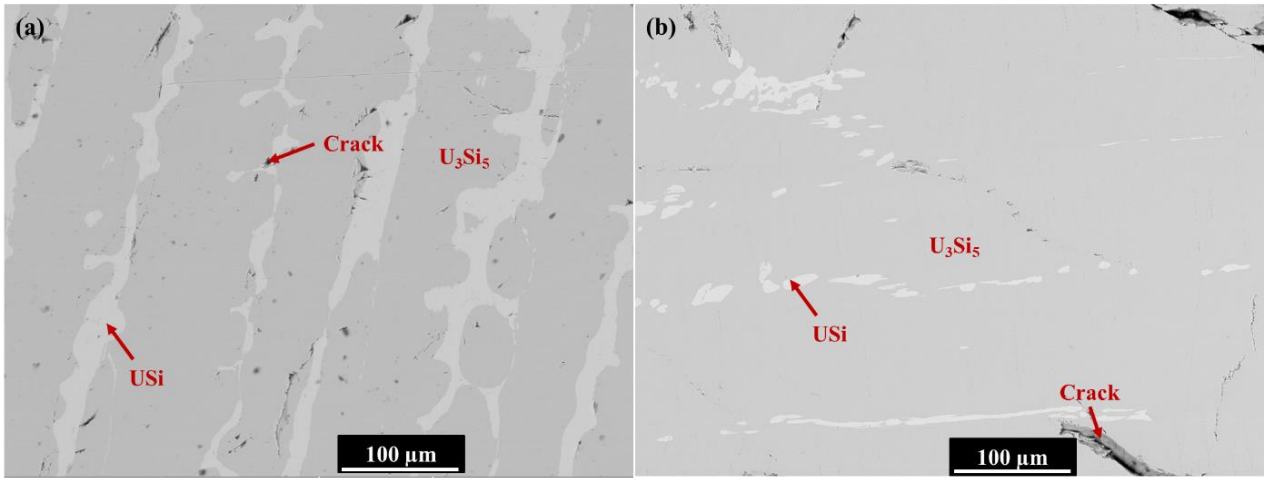

Fig. 3.2. SEM backscatter images for the U/Si = 2/3.36 sample as-cast (a) and annealed (b). Magnification 500x and an acceleration voltage 20.0 kV.

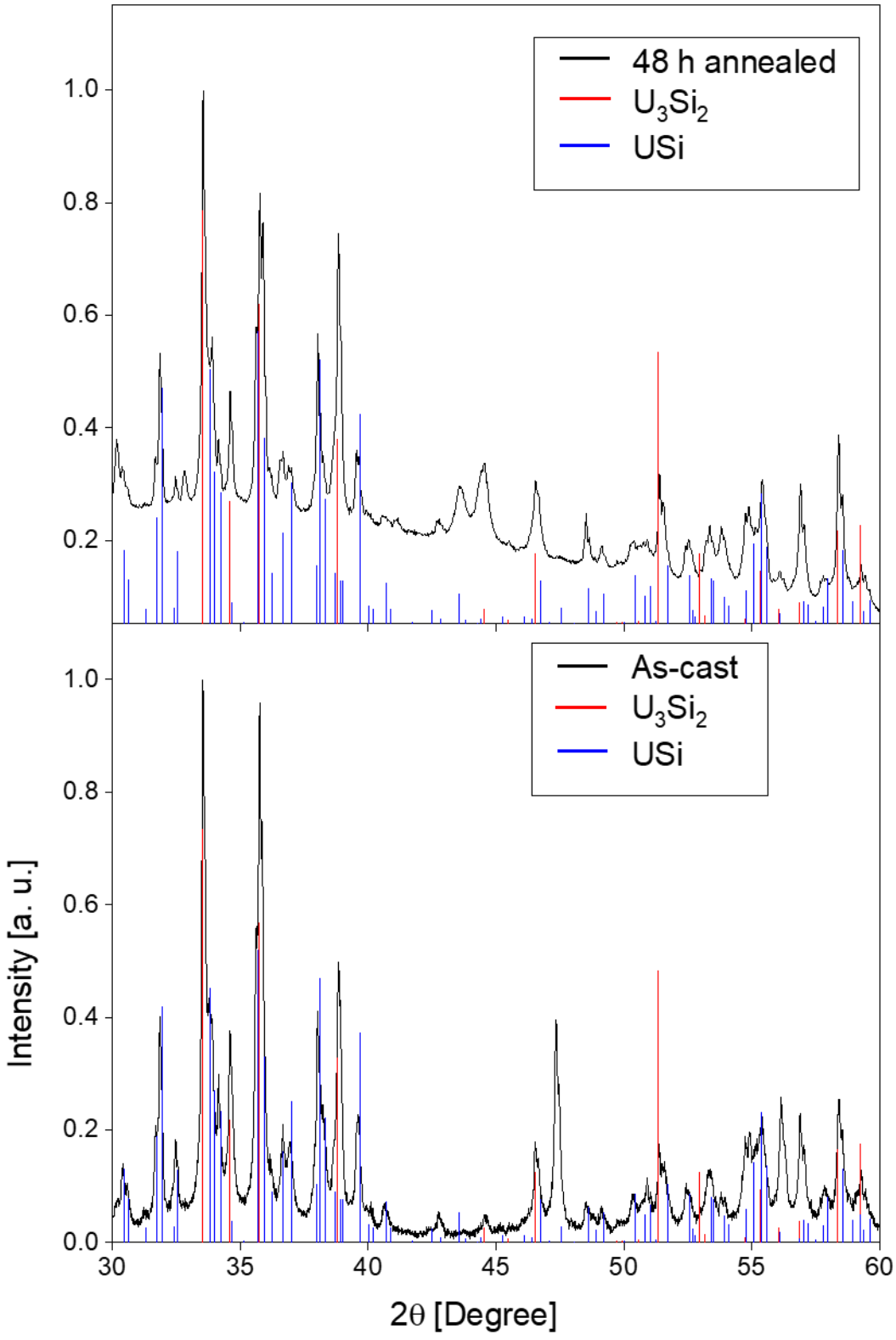

Fig. 3.3. XRD pattern for the U/Si = 5/4.23 Si samples-cast (bottom) and annealed (top), indexed with PDF-01-081-2241 for U_3Si_2 (red) and PDF-01-082-0854 for USi (blue) [47]. Note that the background is subtracted from the as-cast pattern.

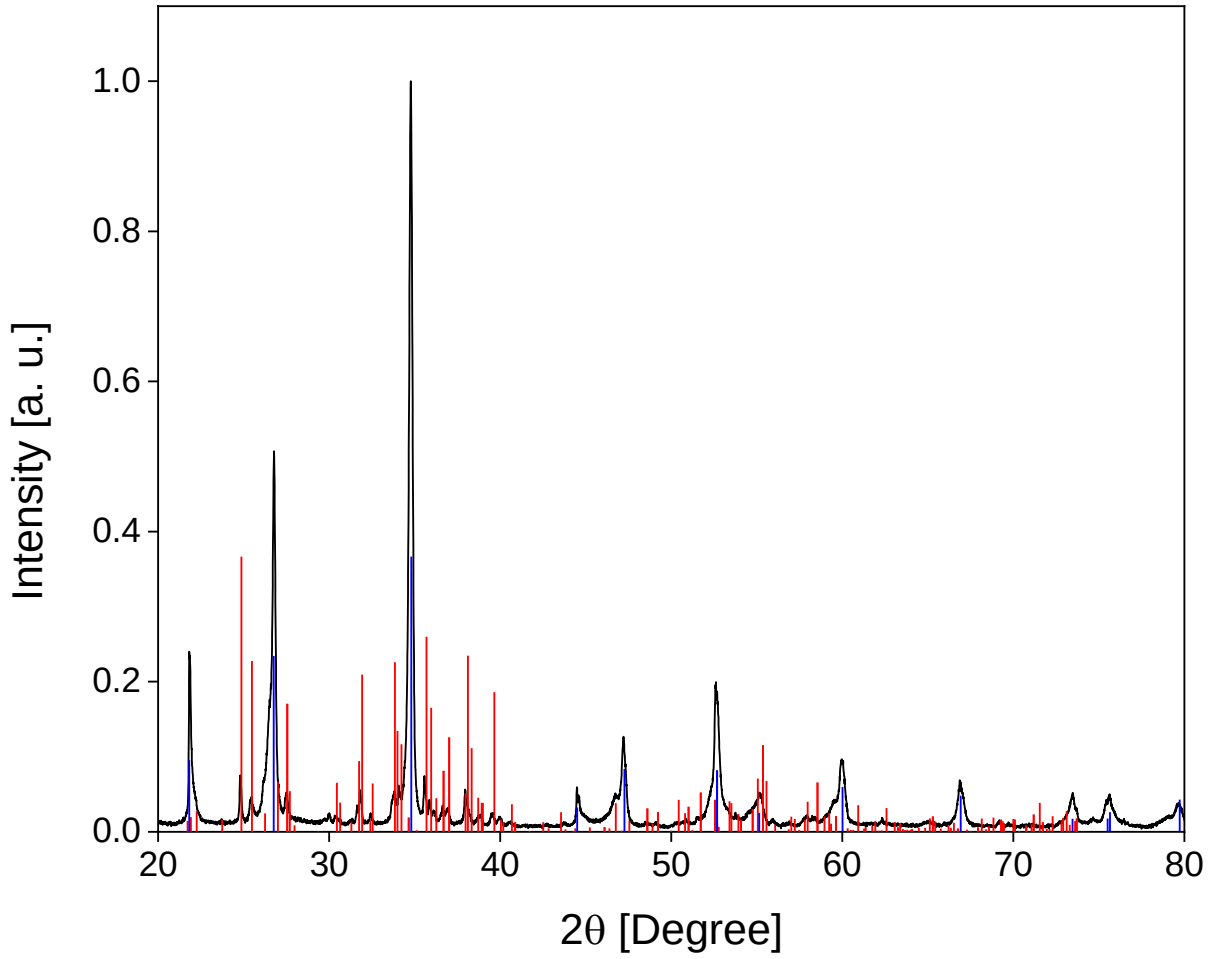

Fig. 3.4. XRD pattern for the U/Si =2/3.36 sample indexed with PDF-01-082-0854 for USi (red) and PDF-01-071-3912 for U_3Si_5 (blue) [47].

The DFT-computed energy of formation for relaxed U_5Si_4 ($U_{20}Si_{16}$) and U_2Si_3 are compared to those of U_3Si_2, USi and U_5Si_4 proposed by Noel et al. [40] in Fig. 3.5. The relaxed U_5Si_4 ($U_{20}Si_{16}$) agrees with the structure reported by Noel et al. [40] and lies on the U-Si convex hull implying the phase is energetically stable at the 0 K. The lowest energy structure for U_2Si_3 has a *P6/mmm* space group, however its energy is above the convex hull, indicating that this phase is energetically unstable. Phonon calculations suggest that both the U_5Si_4 and U_2Si_3 phase are dynamically unstable, i.e., they have imaginary (negative) phonon frequencies, as seen in Fig. 3.6. A closer look at the negative phonon modes show that the U_5Si_4 can be stabilized by introducing interstitial atoms at the 3g [(0.5, 0, 0.5), (0, 0.5, 0.5), (0.5, 0, 0.5)] sites, between the U atoms. On the other hand, the negative phonon modes of the U_2Si_3 causes distortion of the structure in all directions, indicating that (1) a lower symmetry structure is dynamically more favorable or (2) U_2Si_3 will dissociate forming two different phases.

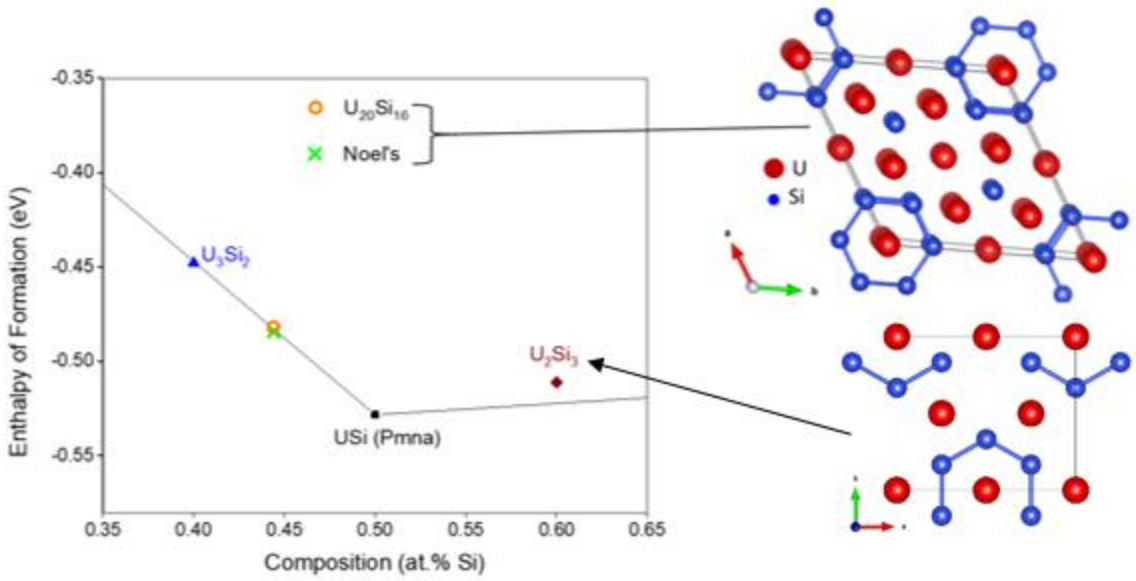

Fig. 3.5. Enthalpy of formation for relaxed U_2Si_3 and U_5Si_4 phases. A $U_{20}Si_{16}$ unit cell was used for the U_5Si_4 phase, and its crystal structure (right) agreed with the experimentally reported structure of Noel et al. [23].

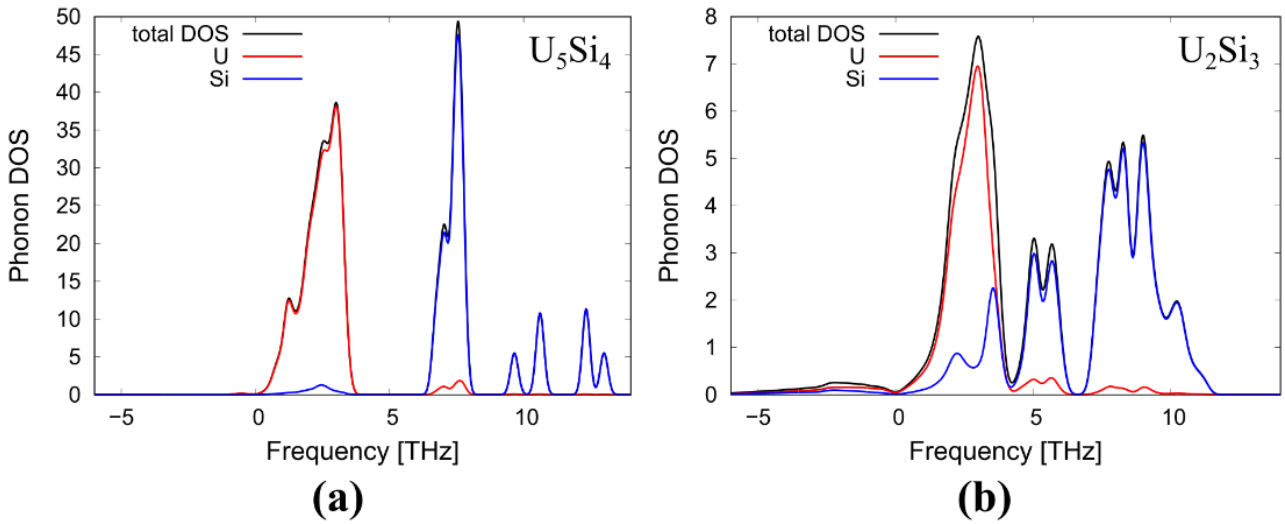

Fig. 3.6. Phonon density of states (DOS) and the contribution from the U (red) and Si (blue) atoms to the phonon DOS of the U_5Si_4 (a) and U_2Si_3 (b), calculated using U_{eff} = 1.5 eV.

3.2.2. USi

The final goodness of fit, χ^2 and R_{wp} at each temperature for the Rietveld analysis of the neutron diffraction spectra for U/Si = 1/0.98 are listed in Table 2.2. The U/Si = 1/0.98 sample was single phase with no unidentified peaks in the diffraction pattern, with the refinement results from the high resolution (144°) and the medium resolution (90°) detectors at room temperature and 1100 °C provided in Fig. 2.7 with the simultaneously refined data from the 120°, 60°, and 40° detectors omitted. Although good agreement was obtained between the calculated and experimental spectra, there were observed differences in the intensities and the profile shape of the peaks.

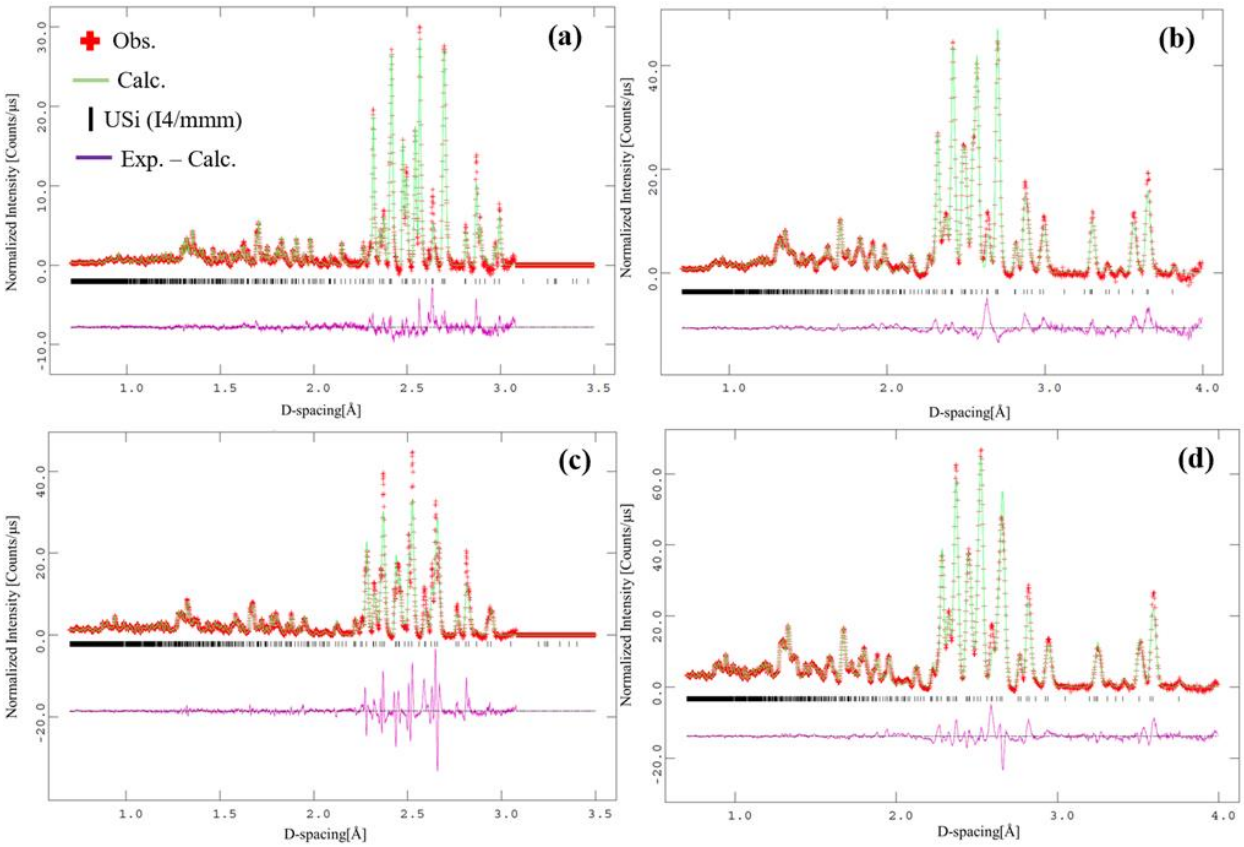

Fig. 3.7. Rietveld fit for the U/Si = 1/0.98 sample. At 1100°C (a,b) and 30°C (c,d) from the high resolution 145° (a,c) and medium resolution 90° detector rings (b,d). The raw data points are shown in red and the calculated profile as green solid curve. The modeled I4/mmm USi is indicated by the black tick marks and the difference curve (y_{obs}-y_{calc}) is the solid purple curve.

The crystal structure of the U/Si = 1/0.98 sample at room temperature is overlaid with the difference Fourier map in Fig. 3.8. The lattice parameters and cell volume are plotted in Fig. 3.9 as a function of temperature with the unit cell parameters fitted with a second order polynomial. There are 6 uranium atoms occupying the 4e, 8f, 8j, 16n, and 16m Wyckoff sites and 8 silicon atoms occupying the 2a, 4c, 4e, 8h, 16n, and 16m Wyckoff sites. The silicon atoms on the 2a and 4e sites both have partial occupancies from our refinement of 0.69(2) and 0.41(2), respectively, with Rietveld refinement indicating an $U_{68}Si_{67}$ ($USi_{0.99}$) stoichiometry, in agreement with the composition determined during synthesis (Table 3.1). The Wyckoff sites and atomic positions for each atom in U/Si = 1/0.98 from our Rietveld refinement are provided in Table 3.4. The atomic displacement for U and Si atoms are plotted in Fig. 3.10 and Fig. 3.11, respectively.

Table 3.4. Wyckoff sites, atom position, and site occupancies for the USi structure from the 30°C diffraction spectra.

Atom Type	Wyckoff Position	x	y	z	Site Occupancy
U1	4e	0	0	0.2580(2)	1
U2	8f	0.25	0.25	0.25	1
U3	8j	0.2660(2)	0.25	0	1
U4	16n	0	0.2607(2)	0.06181(7)	1
U5	16n	0	0.3573(2)	0.19268(9)	1
U6	16m	0.3137(1)	0.3137(1)	0.11595(8)	1
Si1	2a	0	0	0	0.69(2)
Si2	4c	0	0.5	0	1
Si3	4e	0	0	0.0892(7)	0.41(2)
Si4	4e	0	0	0.4264(3)	1
Si5	8h	0.2318(3)	0.2318(3)	0	1
Si6	16n	0	0.2593(4)	0.3014(1)	1
Si7	16n	0	0.3828(3)	0.3988(1)	1
Si8	16m	0.1279(2)	0.1279(2)	0.1576(2)	1

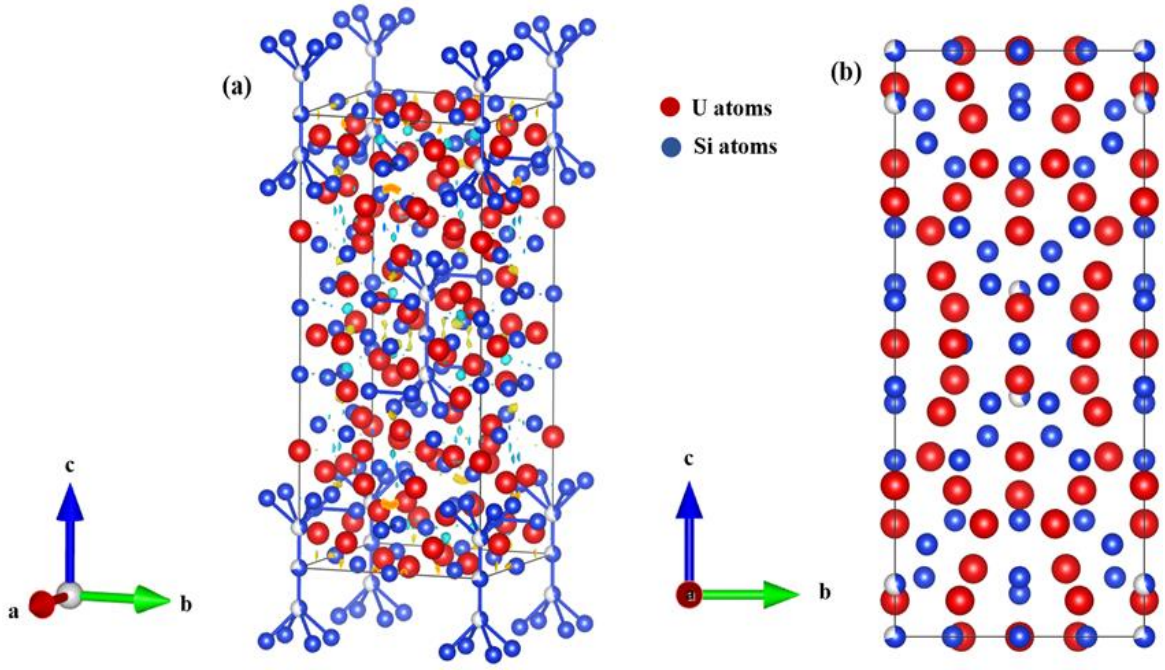

Fig. 3.8. The refined crystal structure of USi (I4/mmm) (a) overlaid with the crystal structure is the difference Fourier map for ~60% of the maximum density (yellow positive difference, blue negative difference). The uranium atoms are shown in red, while Si atoms are shown in blue. Some of the Si atomic sites are partially occupied shown by the white space. (b) A different view of the USi structure with the supercell more evident.

The thermal expansion and the resulting determined coefficient of thermal expansion (CTE) are provided in Fig. 3.12 and illustrate anisotropy in the thermal expansion of USi, where the a- and c-lattice parameter increase by approximately 1.2% and 3.4% respectively over the temperature range, while the volumetric expansion was ~1.7% from room temperature to 1100°C. The fitted CTE, α, and relations for the a- and c-lattice parameters are provided in Eq. (3.1) and (3.2).

$$\alpha_a = 15.6972(5) - 0.0047200(8)T/°C \quad 3.1$$

$$\alpha_c = 22.7768(4) - 0.0033400(5)T/°C \quad 3.2$$

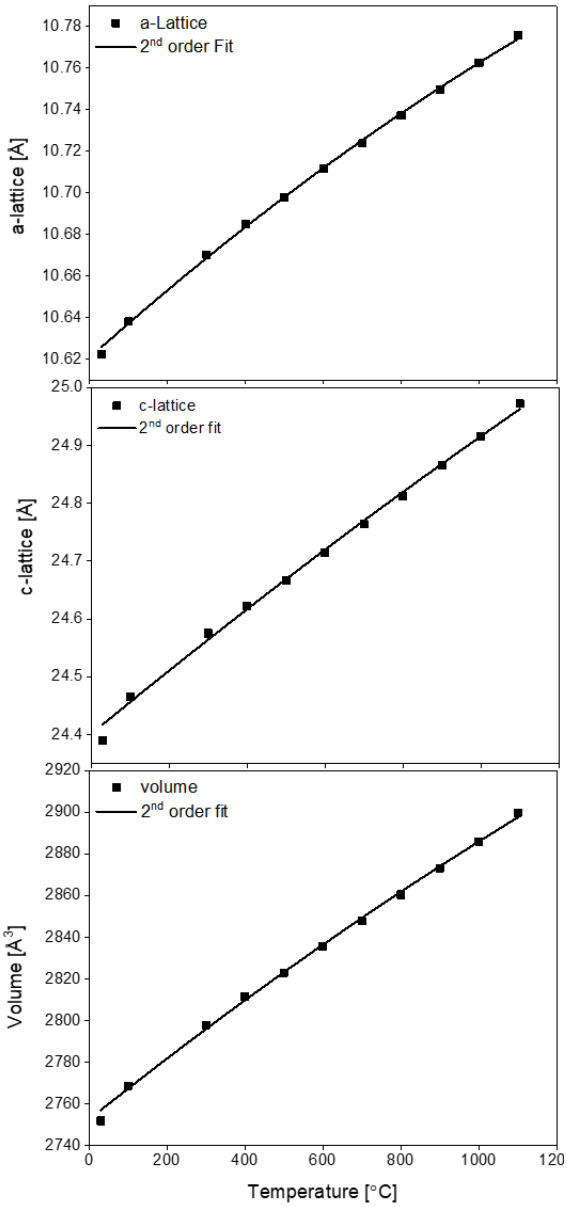

Fig. 3.9. Lattice parameters and unit cell volume as a function of temperature for U/Si = 1/0.98.

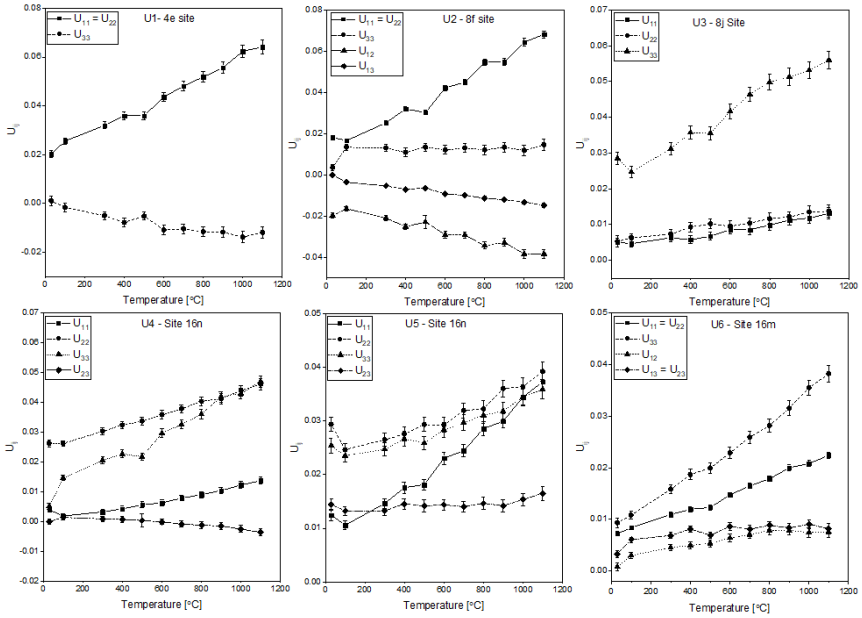

Fig. 3.10. Anisotropic atomic displacement parameters U_{ij} as a function of temperature. U_{11}, U_{22} and U_{33} correspond to atomic displacement along the a, b and c direction, respectively. U_{12} and U_{13} correspond to the thermal motion in the a-b and a-c planes, respectively. Note the different scales for the y-axis.

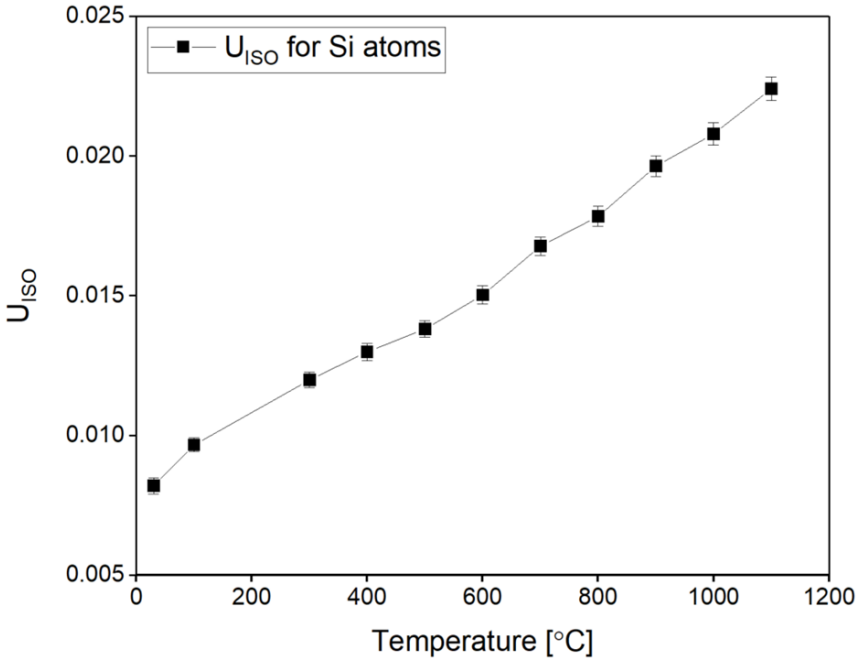

Fig. 3.11. Isotropic atomic displacement parameter U_{ISO} as a function of temperature for Si atoms.

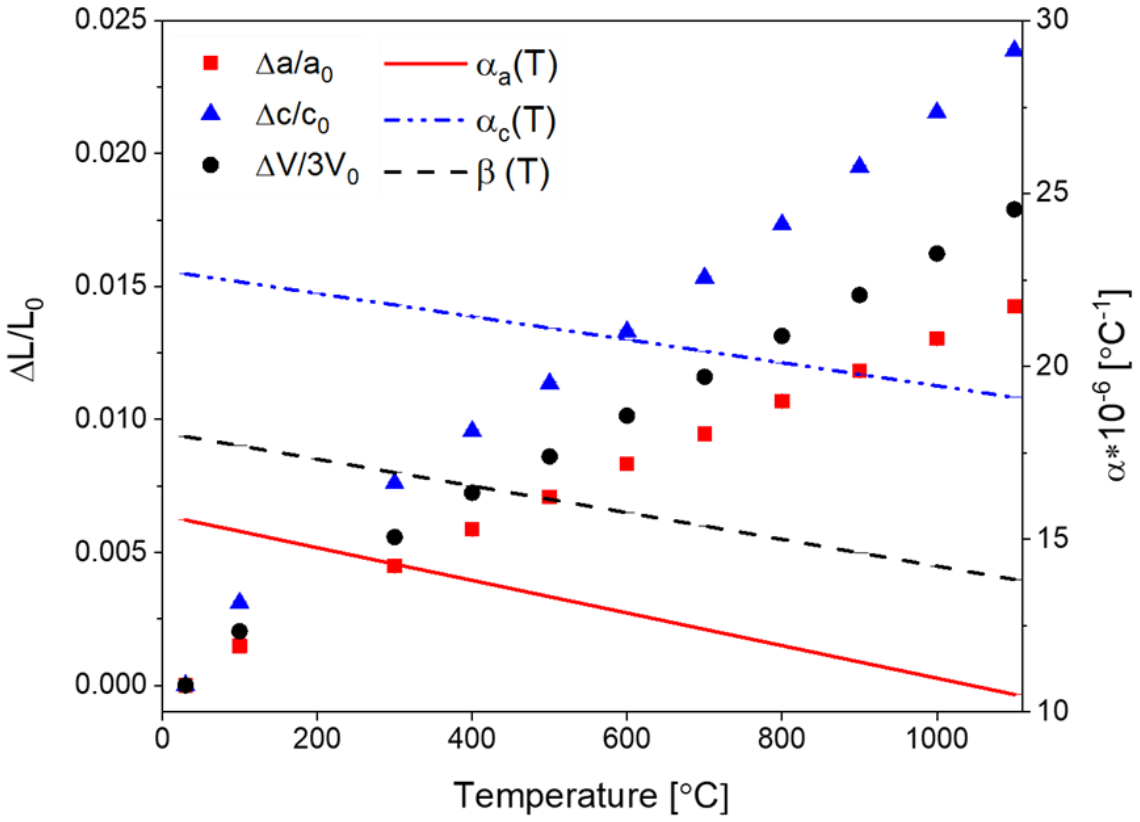

Fig. 3.12. Thermal expansion of the a and the c axis and the unit cell volume as a function of temperature (left axis) and the coefficient of thermal expansion (right axis).

3.3. U-Si Phase Relations Evaluation

Based on the experimental and computational results of this and related studies [40, 47, 48] the U_2Si_3 cannot be considered an equilibrium phase in the U-Si system. The U_2Si_3 phase was reported by Kaufmann et al. [38] and the details of the experimental technique was not presented.

The sample with composition U/Si = 5/4.23 (45.83 at.% Si) should have provided indications of the U_5Si_4 phase first reported by Noël et al. [40], however, it was found to contain$USi_{0.91}$ (USi structure) and $U_3Si_{1.93}$ (U_3Si_2 structure), suggesting that U_5Si_4 is not an equilibrium phase in agreement with other experimental studies [13, 38, 47-50]. The result is further supported by the DFT calculations, where although the phase may have a small but sufficiently negative free energy of formation at 0K, the computed phonon spectra suggest that it is dynamically unstable.

It is possible that the U_5Si_4 compound is a metastable phase and thus it was observed in samples that did not achieve equilibrium, or that it was stabilized by one or more impurities. The report of a U_5Si_4 phase by Berche et al. [37] is dismissed due to the inconsistency of their DTA measurements. Given that there is a stable isostructural ternary phase, $U_{20}Si_{16}C_3$ (P*6/mmm*), it is possible that the experimentally reported U_5Si_4 could be stabilized by contaminant oxygen or carbon, which is plausible as there are several reported U-Si-containing ternary phases (U_8Si_8O, $U_3Si_2C_2$, U_2Si_3Fe, and $USi_2Fe_{0.8}$) [44, 51, 52].

The structure of the USi phase from room temperature to 1100˚C is tetragonal with the *I4/mmm* space group, in agreement with Bihan et al. [44]. The sample with a composition slightly less than U/Si = 1/1 (i.e., U/Si = 1/0.98) did not allow formation of U_3Si_5, suggesting a narrow if any homogeneity range

for the phase. A unit cell containing 68 uranium atoms and 67 silicon atoms is proposed, indicating a stoichiometry of $USi_{0.99\pm0.4}$. In their work, Bihan et al. [44] were only able to refine one of the eight Si sites, whereas in this study all possible Si sites were considered, and where two of the Si sites, 2a and 4e, were found to be only partially filled.

Thermal expansion in the USi structure is observed to be anisotropic, with greater expansion along the c-direction. The volumetric expansion was found to be ~1.7% from room temperature to 1100 °C, which is in good agreement with White et al. [50], who measured the thermal expansion of USi using dilatometry to be ~2.0% at 1100 °C.

4. Assessment of U-Si Thermodynamics and Phase Equilibria

To better understand the U-Si phase equilibria and produce necessary data for an assessment, computational and experimental analyses were performed over the U_3Si_2-USi_3 phase region. The FactSage thermochemical software and database package [53] was used to perform a CALPHAD (Calculation of Phase Diagram) optimization of the U-Si system resulting in a self-consistent database, which was used to calculate the equilibrium phase diagram and other thermodynamic properties.

The U-Si phase equilibria was previously assessed in 2009 by Berche *et al*. [37] and again in 2016 by Wang *et al*. [24], using the CALPHAD methodology. In their assessment, Berche el al. [37] did not account for the following in their optimization:

- The allotropic phase transition at 770 ˚C for the U_3Si phase determined by Kimmel *et al*. [54] and was confirmed by Dwight [55] and Remschnig *et al*. [10].
- The U_5Si_4 phase discovered by Noel *et al*. [40] and the USi_2 phase by Brown and Norreys [38].
- The solubility of U in silicon at high temperatures and the homogeneity ranges proposed for U_3Si_2, U_3Si_5, and $USi_{1.88}$ [48].

Furthermore, new calorimetric measurements for the heat capacities of the U_3Si, USi, U_3Si_2 and U_3Si_5 phases [13, 16, 50, 56] and enthalpy of formation for the USi (tetragonal structure), U_3Si_2 and U_3Si_5 (63.10 at.% Si) phases [57] occurred after their assessment, which prompted the re-assessment by Wang *et al*. [24]. Although Wang *et al*. [24] included the USi_2 and U_5Si_4 phases in their assessment, they suggested further experimental work was needed to determine if these phases were in equilibrium or if they were metastable phases. Like the assessment by Berche *et al*. [37], Wang *et al*. [24] represented the U_3Si_2 and the U_3Si_5 phases as line compounds and new experimental measurements were made after their assessment. In this work, before the optimization was performed, the non-stoichiometry of the U_3Si_2 and U_3Si_5 phases and the stability of the U_5Si_4 were determined.

The non-stoichiometry of the U_3Si_2 phase was determined by high temperature neutron analysis and DFT predictions of point defect concentration and formation energies and was discussed in Chapter 3. Experimental results indicated that $U_3Si_{2.01}$ was indeed single phase from room temperature to 1100 ˚C and DFT predicted that interstitial Si concentration can lead to non-stoichiometry in U_3Si_2 in a U-rich (i.e. in equilibrium with U_3Si), Si-rich (equilibrium with USi), and near stoichiometric environment. Middleburg el at. [14] also showed the non-stoichiometry in U_3Si_2 ($U_3Si_{1.97}$ to $U_3Si_{2.05}$) starting at 1000 °C using only the enthalpy of formation and applying a scaling factor. Therefore, in this work, the U_3Si_2 phase is modeled as a nonstoichiometric solution phase.

The phase stability of the U_5Si_4 phase was investigated experimentally by using XRD, SEM-EDS, and Rietveld refinement techniques as detailed Section 3 of the current report. It was verified computationally by phonon density of state calculations and by the energy of formation relative to all other potential phases [22]. The formation energy of U_5Si_4 phase was located only 2 meV above the convex hull yet was dynamically unstable. This suggested that, depending on the experimental technique, it may be possible to form it as a metastable phase. Since both experimental and computational analyses are in agreement regarding metastability of U_5Si_4, it was not included in our optimization of the phase diagram.

Work described in Section 3 indicates the U_3Si_5 composition can range from 62.4 < at.% Si < 64. A sample with the composition 64.63 at.% Si contained USi_3, U_3Si_5, and $USi_{1.84}$ in the as-melted condition; however, after annealing the composition equilibrated to single-phase $USi_{1.84}$. Compositions greater than 64.63 at.% Si were a two-phase mixture of $USi_{1.84}$ and USi_3. Therefore, the $USi_{1.84}$ will be modeled as a line compound while U_3Si_5 will be modeled as a solid solution.

4.2. CALPHAD Methodology

CALPHAD [58] method is a commonly used for calculating phase diagrams and predicting thermodynamic properties of a given system through critical assessment of available experimental and/or theoretical data. The CALPHAD method uses mathematical models with adjustable parameters to represent Gibbs energy functions of the phases as a function of temperature, pressure, and composition and calculates the thermodynamic equilibrium by minimizing the Gibbs energy of the system [59, 60]. These functions are stored in a database and are used to calculate phase diagrams and thermodynamic properties. These databases are constructed by incorporating phase diagram data, thermochemical data, and physical and crystallographic properties of the phases [61].

The first step in the CALPHAD method is to perform a thorough literature search and critically evaluate all the available data. The type of data to search for include; (i) experimentally measured thermodynamic quantities such as enthalpies and heat capacity data, (ii) the phase diagram data such as the liquidus temperatures and the phase transition reactions, (iii) crystallographic information of solid phases [62], and first-principles calculations of total energies [63]. When evaluating the experimental data, critical attention is payed to the experimental technique, experimental conditions, sample purity, quantities measured, phases present within the system, and accuracy of the measurements as there are many types of equipment utilized to collect the same information. First-principles data are normally used when there are no available experimental data. During the literature search, the possibility of finding previous assessments for the system of interest exists. In such cases, careful examination of the Gibbs energy models used for describing the system is necessary as it may be possible to improve the system. The second step is to develop a mathematical model for G (T, P, composition) for each phase (liquid, solid phases, gas …) and to optimize model parameters simultaneously using all available thermodynamic and phase equilibrium data obtained from the first step. The third step is to use the models to calculate phase diagrams and other thermodynamic properties by minimization of the Gibbs energy. The fourth and final step is to use the calculated phase equilibria to develop a database.

4.3. Thermodynamic Models

The Gibbs energy of a phase can be expressed as follows:

$$G_m = {}^{ref}G_m + {}^{id}G_m + {}^{E}G_m + {}^{phy}G_m \quad (4.1)$$

$${}^{id}G_m = -T{}^{id}S \quad (4.2)$$

where ${}^{ref}G_m$ is the "surface of reference", which represents the Gibbs energy of the mechanical mixture of the constituents of the phase. ${}^{id}G_m$ is the contribution of configuration entropy to the Gibbs energy. *T* is the absolute temperature in Kelvin and ${}^{id}S$ is the configuration entropy, which is determined by the number of possible arrangements of the constituents in a phase. ${}^{E}G_m$ is the excess Gibbs energy, the Gibbs energy change from the ideal solution to the real solution. ${}^{phy}G_m$ represents the Gibbs energy contribution of physical phenomena, such as magnetic transitions.

4.3.1. Gas Phase

The gases in the U-Si system are S_g, U_g, $Si_{2(g)}$ and $Si_{3(g)}$ gases. The Gibbs energy functions for the gases are taken from the SGTE database compiled by Dinsdale [64].

4.3.2. Elements

The molar Gibbs energy °G_i of a pure element i in a phase at Temperature and pressure of 10^5 Pa, relative to the "Standard Element Reference" H_i^{SER}, is described by a power series such as:

$$^\circ G_i - H_i^{SER} = a_0 + a_1 T + a_2 T ln(T) + a_3 T^2 + a_4 T^3 + a_5 T^{-1} + \cdots, T_1 < T < T_2 \quad 4.3$$

a_1, a_2, a_3, … are coefficients, H_i^{SER} is the enthalpy of the pure element i in its reference state. Since the Gibbs energy has no absolute value, it is necessary to refer the Gibbs energy of all phases to the same reference point for each element. It is common practice to choose the reference state to be the most stable phase at 298.15 K, 10^5 Pa. the temperature of T_1 and T_2 determines the range of the power series.
In this work, the molar Gibbs energy of the pure uranium and silicon are the recommended SGTE values compiled by Dinsdale [64].

4.3.3 Stoichiometric Phases

The molar Gibbs energies for stoichiometric phases can be described by

$$^\circ G_T = {}^\circ H_T - T^\circ S_T \quad 4.4$$

$$^\circ H_T = \Delta^{298.15K} H_f^\circ + \int_{298.15\,K}^{T} C_p dT \quad 4.5$$

$$^\circ S_T = \Delta^{298.15K} S_f^\circ + \int_{298.15\,K}^{T} (C_p/T) dT \quad 4.6$$

4.3.4. Two Sublattice Partial Ionic Liquid (TSPIL) Model

The partially ionic two sublattice model [60] is used to model liquid phases as: $(C_i^{+v_i})_P (A_j^{-v_j}, VaB_k^0)_Q$ where C, A, VA and B denotes cation, anion, vacancy, and neutrally charged specie, respectively. Charge neutrality necessitates that Q and P vary such that:

$$P = \sum_A \upsilon_A y_S + Q y_{VA} \quad 4.7$$

$$Q = \sum_C v_C y_C \quad 4.8$$

v_A and y_A are the charge and site fractions of the anion species and v_C and y_C are the charge and site fraction of the cation species C, respectively.

The Gibbs energy of an ionic liquid can be expressed as:

$$G_m = \sum\sum y_{C_i} y_{A_i} {}^\circ G_{C_i:A_i} + Q\left(y_{Va} \sum y_{C_i} {}^\circ G_{C_i} + \sum y_{B_k} {}^\circ G_{B_k}\right) + RT\left[P \sum y_{C_i} ln y_{C_i} + Q\left(\sum y_{A_j} ln y_{A_j} + y_{Va} ln y_{Va} + \sum y_{B_k} ln y_{B_k}\right)\right] + {}^E G_m \quad 4.9$$

where $^\circ G_{C_i:A_i}$ is the Gibbs energy of formation for $v_i + v_j$ moles of atoms of the endmembers C_iA_j while $^\circ G_{C_i:A_i}$ and $^\circ G_{C_i:A_i}$ are the formation values for C_i and B_k.

4.3.5. Solid Solutions

The compound energy formalism (CEF) was introduced by Hillert [65] to describe the Gibbs energy of solid phases with sublattices. These phases have two or more sublattices and at least one of these sublattices has a variable composition. Ideal entropy of mixing is assumed on each sublattice. This model is generally used to model crystalline solids; but, it can also be extended to model ionic liquids.
Here, a solution phases with two sublattices, (A,B)a(C,D)b, will be used as an example to illustrate the compound energy formalism. In this model, components A and B can mix randomly on the first sublattice, as do the components C and D on the second sublattice. a and b are the corresponding stoichiometric coefficients. Site fraction y_i^s is introduced to describe the constitution of the phase and is defined as follows:

$$y_i^s = \frac{n_i^s}{N^s} \tag{4.10}$$

n_i^s is the number of component *i* on sublattice (s) and Ns is the total number of sites on the same sublattice. When vacancies are considered in the model, the site fraction becomes:

$$y_i^s = \frac{n_i^s}{n_{VA}^s + \sum_i n_i^s} \tag{4.11}$$

n_{VA}^s is the number of vacancies on sublattice (s). The site fraction can be transferred to mole fraction (x_i) using the Eq. below:

$$x_i = \frac{\sum_s n^s y_i^s}{\sum_i n^s (1 - y_{VA}^s)} \tag{4.12}$$

When each sublattice is only occupied by one component, then end-members of the phase are produced. In the present case, four end-members exist. They are A_aC_b, A_aD_b, B_aC_b and B_aD_b. The surface of reference ${}^{ref}G_m$ is expressed as:

$${}^{ref}G_m = y^1 y^{2\circ} G_{A:C} + y^1 y^{2\circ} G_{A:D} + y^1 y^{2\circ} G_{B:C} + y^1 y^{2\circ} G_{B:D} \tag{4.13}$$

The ideal entropy (${}^{id}S_m$) and the excess free energy are expressed as follows:

$${}^{id}S = -R[a(y_A^1 ln y_A^1 + y_B^1 ln y_B^1) + b(y_C^2 ln y_C^2 + y_D^2 ln y_D^2)] \tag{4.14}$$

$${}^{E}G_m = y_A^1 y_B^1 \left(y_C^2 L_{A,B:D} + y_D^2 L_{A,B:D}\right) + y_C^2 y_D^2 \left(y_A^1 L_{A:C,D} + y_B^1 L_{B:C,D}\right) \tag{4.15}$$

The binary interaction parameters $L_{i,j:k}$ represent the interaction between the constituents *i* and *j* in the first sublattice when the second sublattice is only occupied by constituent *k*. These parameters can be further expanded with Redlich-Kister polynomial as follows:

$$L_{i,j:k} = \sum_\nu (y_i^1 - y_j^1)^\nu \cdot {}^\nu L_{i,j:k} \tag{4.16}$$

In the case of a three sublattice model:

$$G_m = \sum_i y_i^I \sum_j y_j^{II} \sum_k y_k^{III\circ} G_{i,j,k} + RT \sum_s \sum_i a^s y_i^s ln y_i^s + {}^E G_m \tag{4.17}$$

$$\begin{aligned} {}^{E}G_m = {} & \sum_i y_i^I \sum_j y_j^{II} \sum_k y_k^{III} \left[\sum_{l>i} y_l^I \sum_\nu {}^\nu L_{i,l:j:k} (y_i^I - y_l^I)^\nu \right. \\ & + \left[\sum_{l>j} y_l^{II} \sum_\nu {}^\nu L_{i:j,l:k} (y_j^{II} - y_l^{II})^\nu + \left[\sum_{l>k} y_l^{III} \sum_\nu {}^\nu L_{i:j:k,l} (y_k^{III} - y_l^{III})^\nu \right. \end{aligned} \tag{4.18}$$

4.4. Modeling U-Si Thermodynamics and Phase Equilibria

Summarized in Table 4.1 are the phases, with their crystal structure, space groups, prototypes, composition, and the thermodynamic model of the U-Si phases studied in this work. The optimized parameters for the compounds and solid solutions are provided in Table 4.2, and the phase diagram is provided in Fig. 4.1.

Unlike the previous two models [24, 37], the liquid phase is modeled using the TSPIL model, where the first sublattice contains the U^{+4} and Si^{+4} cations and the second sublattice is occupied by a neutral vacancy.

$$(U^{+4}, Si^{+4})(VA) \qquad 4.18$$

This model was chosen because it is the mostly commonly used for modeling liquid phases and will therefore make incorporation of other elements into the U-Si database (example fission product) a straightforward process. The excess energy parameters from Berche *et al*. [37] were used for the initial point and adjusted as necessary.

Table 4.1. Phase, crystal structure, and thermodynamic model used in this work.

Phase	at.% Si	Pearson Symbol	Space Group	Struktur-bericht designation	Prototype	[i]Model
Liquid	0 to 100					TSPIL
Bcc (U)	0 to 3	*cI2*	*Im-3m*	*Ab*	α-U	CEF
Tetragonal (U)	0 to 1	*tP30*	*$P4_2/mmm$*	*A2*	B-U	CEF
Orthorhombic (U)	0	*oC4*	*Cmcm*	*A20*	W	R-K/Muggianu
Diamond (Si)	100	*cF8*	*Fd-3m*	*A4*	C (Diamond)	R-K/Muggianu
U_3Si (High T)	75	*cP4*	*Pm-3m*	*$L1_2$*	Cu_3Au	ST
U_3Si (Low T)	75	*tl16*	*I4/mcm*	….	….	ST
U_3Si_2	~40 to ~41.5	*tP10*	*P4/mbm*	*D5a*	U_3Si_2	CEF
USi ($U_{68}Si_{67}$)	~50	….	*I4/mmm*	….	USi	ST
U_3Si_5	~61.5-~63	*hP3*	*P6/mmm*	*C32*	AlB_2	CEF
$USi_{1.84}$	64.5	*tl12*	*$I4_1/amd$*	*C_c*	$ThSi_2$	ST
USi_3	75	*cP4*	*Pm-3m*	*$L1_2$*	Cu_3Au	ST

[i]TSPIL is the two sublattice partially ionic liquid model. ST is stoichiometric compound and CEF is the compound energy formalism. R-K/Muggiaun is the one sublattice Redlich-Kister Muggiaun solution model.

The USi_3, $USi_{1.84}$, $U_{68}Si_{67}$, and U_3Si compositions were modeled as stoichiometric phases. The USi phase was previously assessed with the FeB-type structure; however, neutron diffraction confirmed that the phase has a tetragonal structure with *I4/mmm* space group. Therefore, the phase was modeled to reflect this information. The recent enthalpy of formation data collected in 2018 [66] for the USi phase with tetragonal structure was used in the optimization. The composition of the USi_{2-x} phase was adjusted from $USi_{1.88}$ to $USi_{1.84}$ to reflect the experimental findings [10].

The U_3Si_5 and U_3Si_2 phases were modeled as a solid solution using the CEF model. The U_3Si_2 phase was modeled with 3 sublattices $(U)_3(Si)_2(Si,VA)$. Originally, a four sublattice model was applied to the system based on Wyckoff positions of the atoms; however, the model was simplified by adding a third sublattice to its stoichiometric representation (i.e., $(U)_3(Si)_2(Si,VA)$). This is justified as the nonstoichiometry in U_3Si_2 is primarily driven by silicon interstitials defects (see Chapter 3). Modeling the phase in this manner will facilitate modeling incorporation of light elements that are known to dissolve in

the U_3Si_2 lattice such as hydrogen and carbon forms a U_3Si_2X phase (X= H or C). All one would need to do is add these elements to the third sublattice. The model can also be expanded on the first and second sublattices, which will be useful for CALPHAD assessment of fission products with U_3Si_2 fuel.

The U_3Si_5 phase was also modeled using CEF model with 3 sublattices, $(U)_3(Si)_5(Si,VA)$. Although, this phase could have been modeled using 2 sublattices by using the relationship; U_3Si_5 = AlB_2-type USi_{2-x}, modeling with the three sublattice was simpler as there is the $ThSi_2$-type USi_{2-x} structure (i.e., $USi_{1.84}$) close in composition to U_3Si_5, which makes the phase equilibria calculations more difficult.

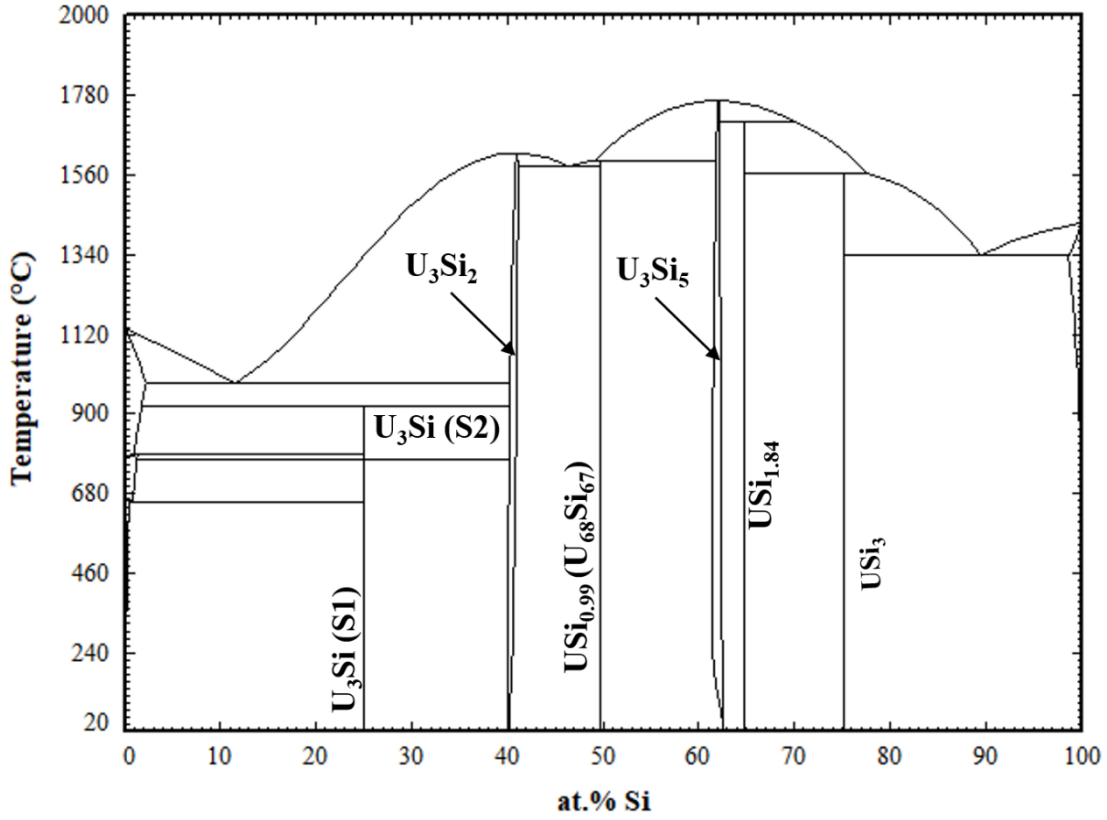

Fig. 4.1. U-Si Phase Diagram calculated from optimization of available experimental data. Both U_3Si_2 and U_3Si_5 are represented with a homogeneity range.

Table 4.2. Optimized thermodynamic parameters for the U-Si system.

Phase	Thermodynamic Parameter (J/mol)	Reference
Liquid: (U^{+4}, Si^{+4})(VA)	$G^{Liq}_{U+4:VA} = G^{Liq}_{U} - {}^{\circ}H^{SER}_{U} = G^{Liq}_{U}$	[64]
	$G^{Liq}_{Si+4:VA} = G^{Liq}_{Si} - {}^{\circ}H^{SER}_{Si} = G^{Liq}_{Si}$	[64]
	${}^{\circ}L_{U+4,Si+4:VA} = -185536.75 + 26.417124T$	[37]
	${}^{1}L_{U+4,Si+4:VA} = -98477.584 + 52.787132T$	[37]
	${}^{2}L_{U+4,Si+4:VA} = 47133.465 - 10.794531T$	This work
BCC_A2: (U, Si)(VA)	$G^{BCC_{A2}}_{U:VA} = G^{BCC_{A2}}_{U} - {}^{\circ}H^{SER}_{U} = G^{BCC_{A2}}_{U}$	[64]
	$G^{BCC_{A2}}_{Si:VA} = G^{Diamond}_{Si} + 49999 + 22.5T$	This work
	${}^{\circ}L_{U,Si:VA} = -96136.807$	[37]
Tetragonal_U: (U, Si)	$G^{Tetragonal}_{U} = G^{Tetragonal}_{U} - {}^{\circ}H^{SER}_{U} = G^{Tetragonal}_{U}$	[64]
	$G^{Tetragonal}_{Si} = G^{Tetragonal}_{Si} - {}^{\circ}H^{SER}_{Si} = G^{Diamond}_{Si} + 4000$	[37]
	${}^{\circ}L_{U,Si:VA} = -78915.524$	This work
Orthorhombic_A20: (U, Si)	$G^{Orthorhombic_{A20}}_{U} = {}^{\circ}H^{SER}_{U}$	[64]
	$G^{Orthorhombic}_{Si} = G^{Orthorhombic}_{Si} - {}^{\circ}H^{SER}_{Si} = G^{Diamond}_{Si} + 4.2$	[24]
	${}^{\circ}L_{U,Si:VA} = -78590 + 13.25T$	This Work
Diamond_A4: (U, Si)	$G^{Diamond_{A4}}_{U} = G^{Orthorhombic_{A20}}_{U} + 31860.9 + 0.2T$	This work
	$G^{Diamond_{A4}}_{Si} = {}^{\circ}H^{SER}_{Si}$	[64]
	${}^{\circ}L_{U,Si:VA} = -100000 - 18 * T$	This work
D5A_U_3Si_2: $(U)_3(Si)_2$(Si, VA)	$G^{D5A_{U3Si2}}_{U:Si:VA} = G^{D5A_{U3Si2}}_{U:Si:VA} - 3{}^{\circ}H^{SER}_{U} - 2{}^{\circ}H^{SER}_{Si}$ $= -189929 - 36T + 3G^{Orthorhombic_{A20}}_{U} + 2G^{Diamond_{A4}}_{Si}$	This work
	$G^{D5A_{U3Si2}}_{U:Si:Si} = G^{D5A_{U3Si2}}_{U:Si:Si} - 3{}^{\circ}H^{SER}_{U} - 3{}^{\circ}H^{SER}_{Si}$ $= -202967 + 7T + 3G^{Orthorhombic_{A20}}_{U} + 3G^{Diamond_{A4}}_{Si}$	
	${}^{\circ}L_{U+4,Si+4:VA} = 1000 - 10.245T$	
	${}^{1}L_{U+4,Si+4:VA} = 32023 + 58.3232T$	
C32_U_3Si_5: $(U)_3(Si)_5$(Si, VA)	$G^{D5A_{U3Si5}}_{U:Si:VA} = G^{D5A_{U3Si5}}_{U:Si:VA} - 3{}^{\circ}H^{SER}_{U} - 5{}^{\circ}H^{SER}_{Si}$ $= -354955.897 - 30T + 3G^{Orthorhombic_{A20}}_{U} + 5G^{Diamond_{A4}}_{Si}$	This work
	$G^{D5A_{U3Si5}}_{U:Si:Si} = G^{D5A_{U3Si5}}_{U:Si:Si} - 3{}^{\circ}H^{SER}_{U} - 3{}^{\circ}H^{SER}_{Si}$ $= -222204.02 + 116.89T + 3G^{Orthorhombic_{A20}}_{U} + 3G^{Diamond_{A4}}_{Si}$	
	${}^{\circ}L_{U+4,Si+4:VA} = 5000 - 205.297T$	
	${}^{1}L_{U+4,Si+4:VA} = 90000 + 78.3232T$	
	${}^{2}L_{U+4,Si+4:VA} = 9800 + 10.215T$	
$U_{68}Si_{67}$	$G_{U68Si67} = G_{U68Si67} - 68{}^{\circ}H^{SER}_{U} - 67{}^{\circ}H^{SER}_{Si}$ $= -56410000.288 - 672.027T + 68G^{Orthorhombic_{A20}}_{U} + 67G^{Diamond_{A4}}_{Si}$	This work
$U_{12}Si_{22}$	$G_{U12Si22} = G_{U12Si22} - 12{}^{\circ}H^{SER}_{U} - 22{}^{\circ}H^{SER}_{Si}$ $= -1544000.01007 - 55T + 12G^{Orthorhombic_{A20}}_{U} + 22G^{Diamond_{A4}}_{Si}$	This work
U_3Si	$G_{U3Si} = G_{U3Si} - 3{}^{\circ}H^{SER}_{U} - {}^{\circ}H^{SER}_{Si}$ $= -1544000.01007 - 55T + 3G^{Orthorhombic_{A20}}_{U} + G^{Diamond_{A4}}_{Si}$	This work
	$\Delta H^{\alpha\rightarrow\beta} = 12600 \ @ \ 1043K$	
USi_3	$G_{U3Si} = G_{USi3} - 3{}^{\circ}H^{SER}_{U} - {}^{\circ}H^{SER}_{Si}$ $= -99650.289 - 16.79T + G^{Orthorhombic_{A20}}_{U} + 3G^{Diamond_{A4}}_{Si}$	This work

4.5. Discussion

The U-Si phase equilibria was modeled using the CALPHAD methodology and for the first time the U_3Si_2 and U_3Si_5 phases were modeled as nonstoichiometric phases using the CEF 3 sublattice model. The optimized diagram is displayed in Fig. 4.2 and is compared to experimental data and calculated diagram by Berche el al [37]. The diagram is in good agreement with respect to melt point and the terminal solutions. Table 4.3. provides the invariant reactions obtained from the optimized Gibbs energy and are compared to reported values.

Table 4.3. Invariant reactions in the U-Si system calculated in the work and compared to literature values.

Reaction	Reaction Type	Temperature (°C)	Composition (at. %U)			Reference
$liquid \leftrightarrow U_3Si_5$	Congruently melting	1770 ± 10			37.5	[38]
		~ 1700			37.5	[19]
		1773			37.5	[24]
		1762			38	This work
$\alpha U_3Si \leftrightarrow \beta U_3Si$	Allotropic	770			75	[55]
		770			75	[24]
		769.85			75	This work
$liquid + U_3Si_5 \leftrightarrow USi$	Peritectic	1580 ± 10		37.5	50	[48]
		1576	~50	37.5	50	[24]
		1597.4	51	38.3	50.4	This work
$liquid \leftrightarrow U_3Si_2$	Congruently melting	1540 ± 10			60	[48]
		1665			60	[38]
		1664			60	[24]
		1618.9			59.1	This work
$liquid + U_3Si_5 \leftrightarrow USi_{1.88}$	Peritectic	1710 ± 10		37.5	34.7	[48]
		1715	28.5	37.5	34.7	[24]
		1706.54	30.2	37.9	35.3	This work
$liquid \leftrightarrow bcc\ U + U_3Si_2$	Eutectic	985	92.1	98.4	60	[38]
		985	88.5	98.2	60	[24]
		982.5	88.6	97.8	59.8	This work
$\beta U_3Si \leftrightarrow bcc\ U + U_3Si_2$	Eutectoid	930	75	98.2	60	[38]
		929	75	98.6	60	[24]
$liquid \leftrightarrow dia.Si + USi_3$	Eutectic	1315	10.7	1.4	25	[44]
		1317	9.7	1.1	25	[24]
		1335.71	10.6	0.014	25	This work
$tetra\ U + \alpha U_3Si$	Eutectoid	665	~100	75	~100	[38]
$\leftrightarrow ortho\ U$		665	~99.4	75	~99.5	[24]
$liquid + USi_{1.88} \leftrightarrow USi_3$	Peritectic	1510 ± 10	19.1	34.7	25	[48]
		1511	17.8	34.7	25	[24]
		1560.43	22.5	35.3	25	This work
$bcc\ U + \alpha U_3Si \leftrightarrow tetra\ U$	Eutectoid	795	98.6	75	97.7	[38]
		794	99.4	75	98.7	[24]
		784.24	99.2	75	98.8	This work
$liquid \leftrightarrow U_3Si_2 + USi$	Eutectic	1583.2	53.8	59.0	50.4	This work
$liquid \leftrightarrow dia.Si$	Melting	1425.26			0	This work
$liquid \leftrightarrow bcc\ U$	Melting	1134.84			100	This work
$bcc\ U + U_3Si_2 \leftrightarrow U_3Si$	Eutectoid	920.06	98.3	59.8	75	This work
$tetra\ U + U_3Si_2 \leftrightarrow U_3Si$	Eutectoid	769.85	98.8	59.9	75	This work
$tetra\ U \leftrightarrow ortho\ U + U_3Si$	Eutectoid	655.99	99.2	99.7	75	This work

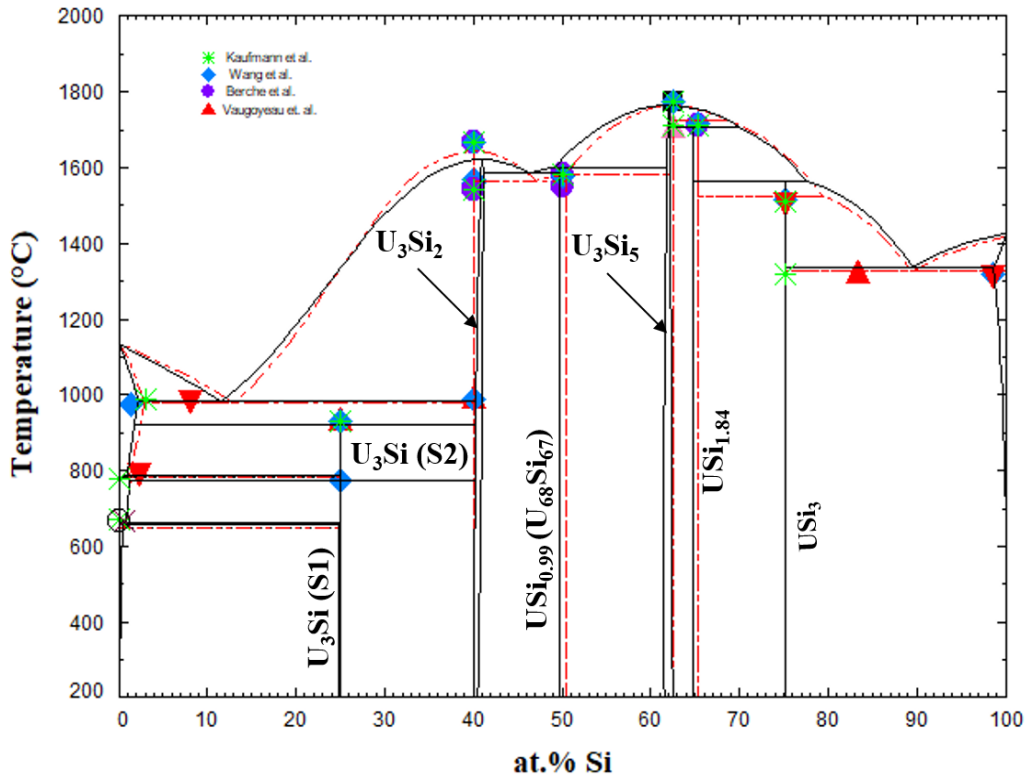

Fig. 4.2. U-Si phase diagram calculated in the work (black) and super-imposed with the one from Berche et al. [37]. The markers are experimental point from [24, 48, 55].

Displayed in Fig. 4.3 is a zoomed in region of the U_3Si_2 (a) and U_3Si_5 (b) phases. The U_3Si_2 phase is modeled with a homogeneity range of $U_3Si_{1.95}$ to $U_3Si_{2.05}$, which is in agreement with the neutron and experimental results of this work; however, it disagrees with the work of Middleburgh *et al*. [14] at low temperatures (I.e., any temperature below 1000 °C). Further experimental work is suggested on samples with a wider homogeneity range to determine the exact width of the solubility range. However, this work shows that modeling the U_3Si_2 phase with the 3 sublattice model is sufficient enough to mimic the experimental composition. Furthermore, it will serve as a starting point for incorporating elements with the affinity for dissolving into U_3Si_2.

Experimentally, it has been shown that the U_3Si_5 phase can exist between the 62.5-63.4 at.% Si phase region; however, since it exists with an unknow phase, the exact composition of the phase is unknown. Although the phase diagram showed an overall good agreement with experimental data, the model for this phase could use further optimizing as the composition range (Fig. 4.3) is narrower than the experimental composition. However, before further optimization of the phase, further experiments and computational analysis would prove useful for understanding the nature of the phase transition associated with the composition.

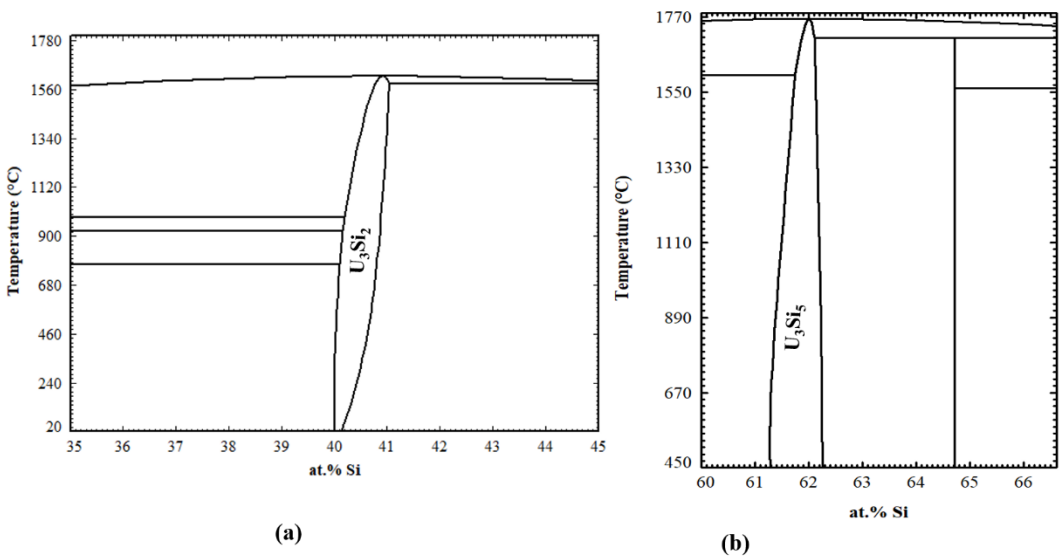

Fig. 4.3. Zoomed in region of the U_3Si_2 (a) and U_3Si_5 (b) phase regions.

Table 4.4. Comparison of Enthalpies of formation for various U-Si phases.

Phase	ΔH_f (kJ/mol-atom) 298K	Method	References
USi_3	-33.02 ± 0.13	Direct comb. Calorimetry	[67]
	-32.19 ± 0.84	Tellurium calorimetry	[67]
	-35.53 ± 4.18	Activity meas.	[68]
	-32.60	Estimation	[69]
	-32.90	Modelling	[37]
	-32.90	CALPHAD	This work
USi_2	-43.47 ± 0.42	Direct comb. Calorimetry	[67]
	-42.64 ± 1.25	Tellurium calorimetry	[67]
	-43.89 ± 4.18	Activity meas.	[68]
	-43.19	Estimation	[69]
	-43.33	Modelling	[37]
	-45.12	CALPHAD	This work
U_3Si_5	-44.26	Estimation	[69]
	-42.9	Modelling	[37]
	-43.8 ± 9.0	Oxidative drop calorimetry	[66]
USi	-40.13 ± 0.84	Direct comb. Calorimetry	[67]
	-43.47 ± 1.67	Tellurium Calorimetry	[67]
	-41.8 ± 4.18	Activity meas.	[68]
	-42.22	Estimation	[70]
	-41.18	Modelling	[37]
	-43.2 ± 6.2	Oxidative drop calorimetry	[66]
	-41.78	CALPHAD	This work
U_3Si_2	-33.2 ± 3.1	High Temp Drop calorimetry	[66]
	-33.86 ± 0.42	Direct comb. Calorimetry	[71]
	-35.95 ± 3.34	Activity meas.	[69]
	-34.11	Estimation	[68]
	-34.32	Modelling	[37]
U_3Si	-26.02 ± 4.8	Fluorine bomb calorimetry	[70]
	-22.99	Estimation	[69]
	-24.93	Modelling	[37]
	-24.91	CALPHAD	This work

5. Compatibility of U_3Si_2 Fuel with Zr-, FeCrAl- and SiC/SiC-Based Cladding

The reassessment of U-Si phase relations described in the previous section was utilized in the effort to understand potential interactions between U_3Si_2 and cladding materials together with the reported relevant binary and ternary systems. For the Fe-Si system the stoichiometric compounds Fe_5Si_3, Fe_2Si, FeSi, $FeSi_2$ and Fe_3Si_7 were considered. Solid solutions on the Fe-rich side have both fcc and bcc crystal structures, with significant Si solubility (up to almost 25 at.%) in bcc-Fe, where the fcc phase is restricted by a γ-loop. A Fe-Si phase diagram based on the thermodynamic assessment of Lacaze and Sundman [72] is presented in Fig. 5.1.

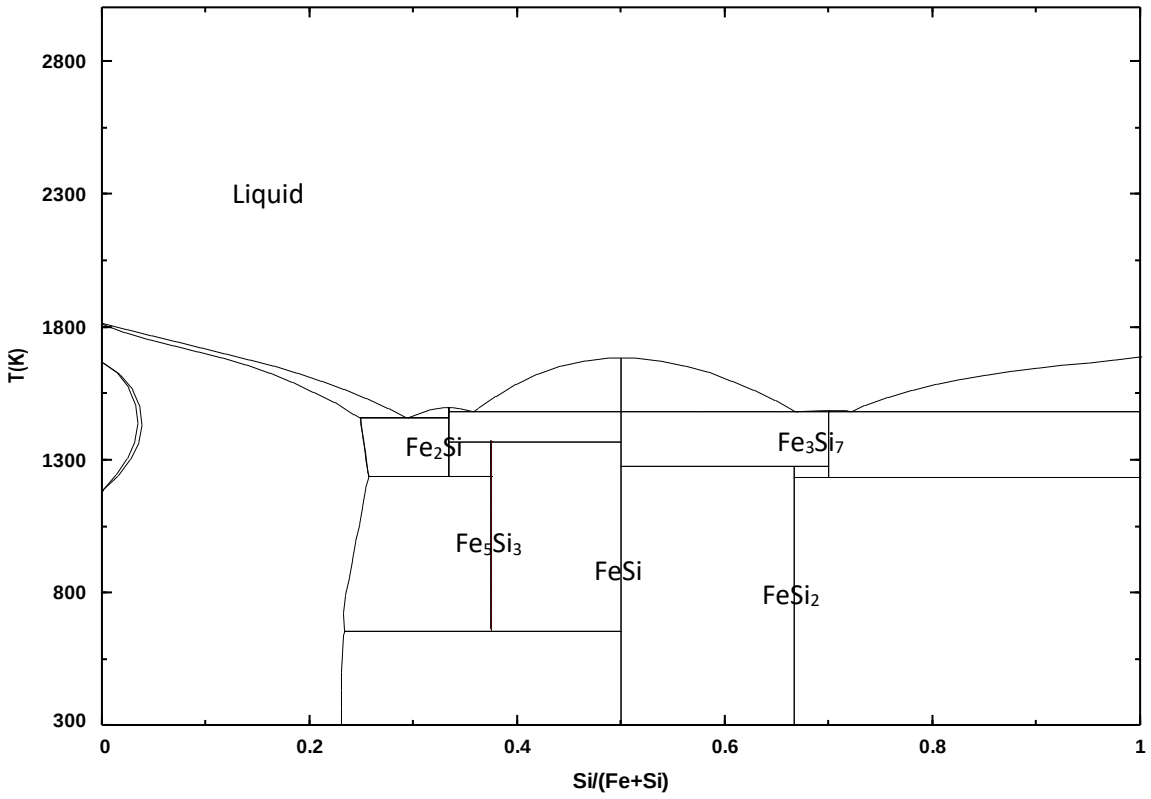

Fig. 5.1. Computed Fe-Si phase diagram based on Lacaze and Sundman [72].

The U-Fe phase diagram contains two stoichiometric intermetallic compounds, UFe_2 and U_6Fe, which have a low eutectic temperature of ~805 °C. There is limited solubility between the metals. A computed phase diagram based on Chatain et al. [73] is seen in Fig. 5.2.

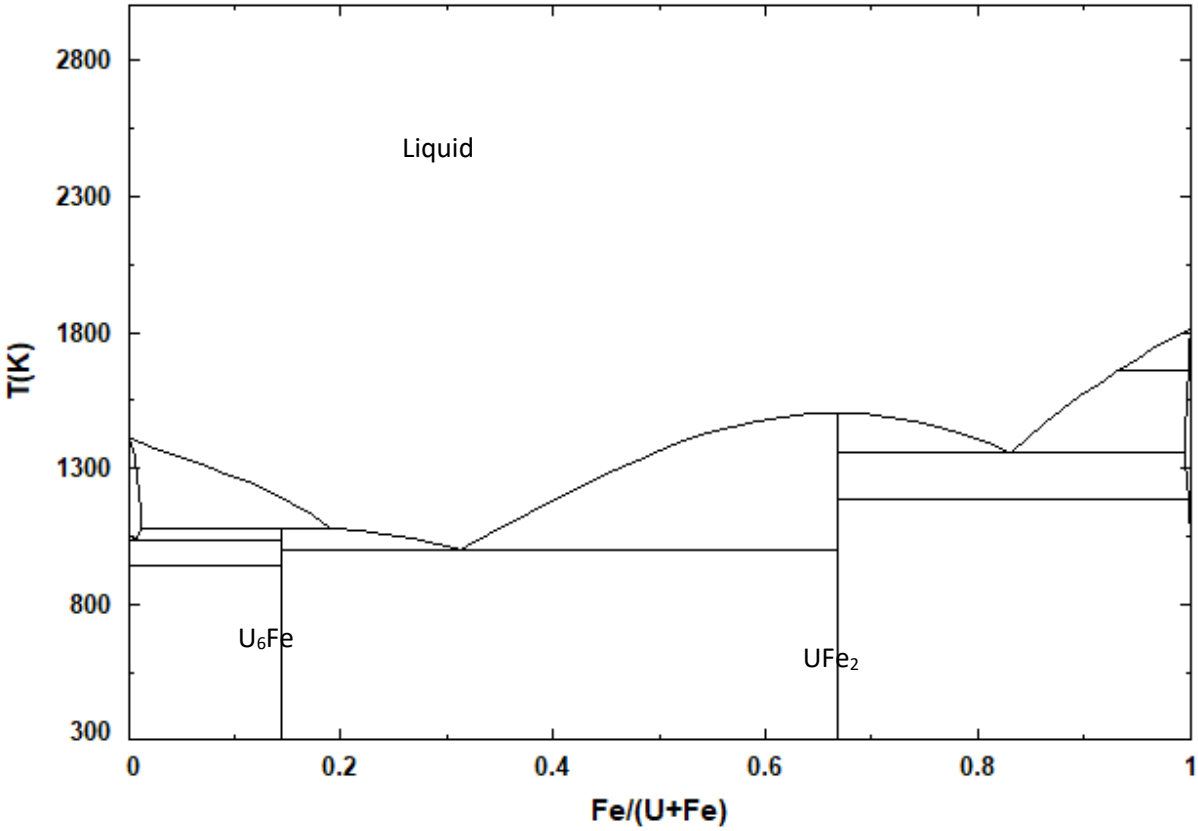

Fig. 5.2. Computed U-Fe phase diagram based on Chatain et al. [73].

The U-Si-C ternary system is well-studied with a recent thermodynamic assessment performed by Dupin[74]. It is characterized by the stability of two ternary phases $U_3Si_2C_2$ (I4/*mmm*) and $U_{20}Si_{16}C_3$ (P6/*mmm*), with extended solubility of carbon (~4 at.%) in U_3Si_2. Despited the current thermodynamic assessment some uncertainties remain, such as a homogeneity range in $U_3Si_2C_2$ that could extend to $U_3Si_2C_3$ that was not considered by Dupin.

Use of ferritic (FeCrAl-based) cladding alloys requires understanding the thermodynamics of the U-Fe-Si system. The phase equilibria has been experimentally investigated by Berthebaud et al. [75] and is a complex assemblage of stoichiometric compounds (7) and solid solutions (4) identified at 900°C: U_3FeSi_3(AlB_2-type), UFe_2Si_2 (Al_4Ba-type), $U_3Fe_2Si_7$ ($La_3Co_2Sn_7$-type), U_2Fe_3Si($MgZn_2$-type), $UFe_{12-x}Si_x$ ($ThMn_{12}$-type), UFeSi (TiNiSi-type), $U_{1.2}Fe_4Si_{9.7}$ ($Er_{1.2}Fe_4Si_{9.7}$ type), $U_2Fe_3Si_5$ ($Lu_2Co_3Si_5$-type), $U_2Fe_3Si_5$ ($Lu_2Co_3Si_5$-type), $U_2Fe_{17-x}Si_x$ (Th_2N_{17}-type) and $UFe_{0.8}Si_2$ (CeNiSi2-type). Significant amounts of alloying chromium and aluminum in the ferritic alloy will further increase the complexity of the system, shifting phase boundaries. While the extensive effort to obtain U-Fe-Si phase equilibria has provided a worthwhile ternary diagram (Fig. 5.3), there are no reports of ternary phase thermodynamic measurements and reported free energies.

A recent experimental study of compatibility of U_3Si_2 with a FeCrAl alloy was performed by Hoggan et al. [76] at ≤1000ºC. Their results indicated significant interactions only at the highest temperature they investigated, 1000ºC, with formation of UFe_2 and the ternary phases UFeSi and U_2Fe_3Si.

The binary systems U-Si and U-Zr are well studied with accepted phase equilibria. The same is not true for the U-Zr-Si system, for which no ternary phases are reported. He et al. [77] performed a compatibility study of U_3Si_2 fuel with Zircaloy-4 and under the conditions of the current study (1000ºC) observed the main interdiffusion products Zr_2Si, U_6Fe, U-Zr-Fe-Ni, U-Zr, and U.

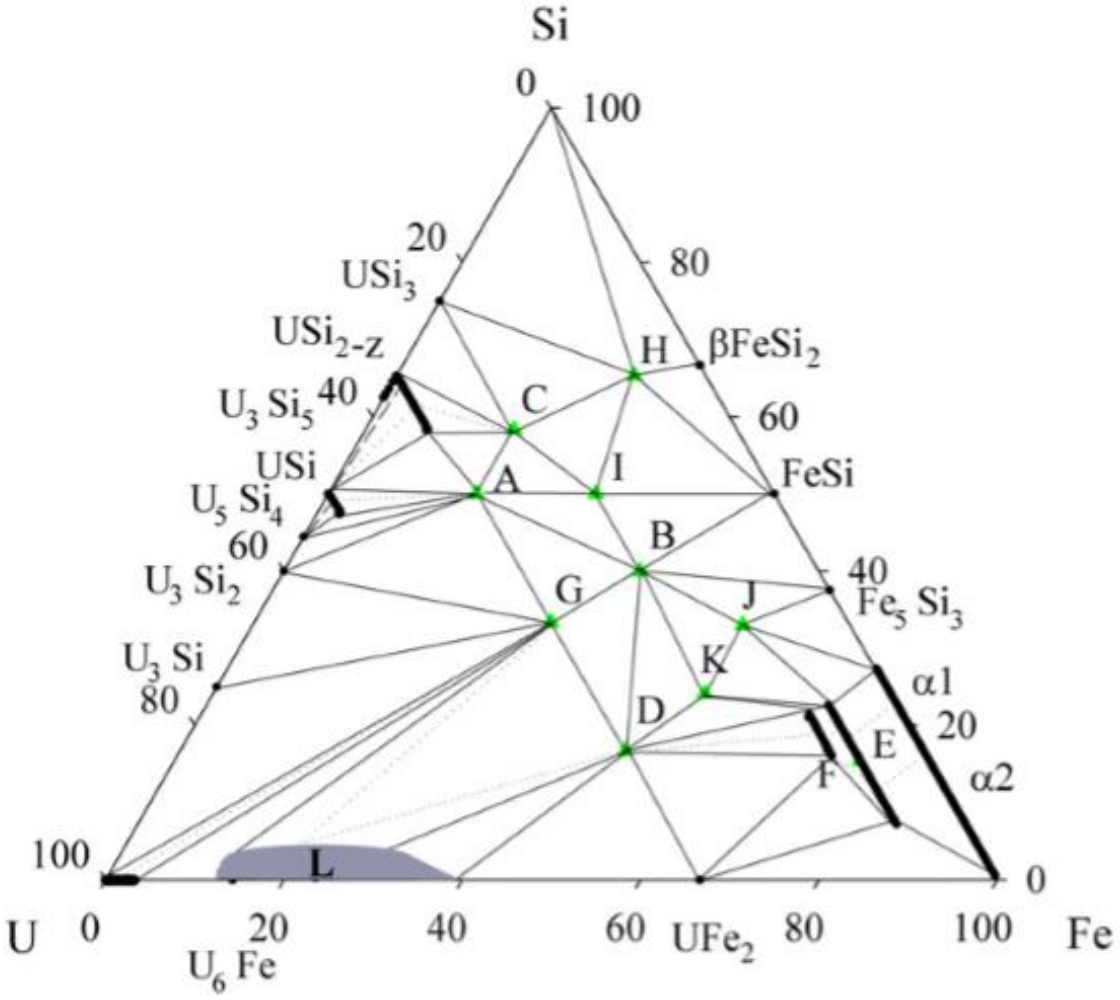

Fig. 5.3. Experimentally determined U-Fe-Si phase diagram by Berthebaud et al. 2008; A=U_2FeSi_3. B=UFe_2Si_2, C=$U_3Fe_2Si_7$, D=U_2Fe_3Si, E=$UFe_{12-x}Si_x$, F=$U_2Fe_{17-x}Si_x$,G=UFeSi, H=$U_{1.2}Fe_4Si_{9.7}$, I=$U_2Fe_3Si_5$, J= UFe_5Si_3 ,K= $U_6Fe_{16}Si_7$

5.1. Methodology

5.1.1. Experimental

The U_3Si_2 material for the current effort was prepared from depleted uranium (Los Alamos National Laboratory, 99.98%) and elemental silicon (Sigma Aldrich, 99.99%) by arc-melting using facilities at the Fuel Research Laboratory at Los Alamos National Laboratory [49]. Arc-melting was conducted inside a glovebox maintained at an oxygen and H_2O level <0.1ppm. Additionally, a copper getter brought the argon gas purging the arc-melter down to 10^{-10} ppm oxygen. The samples were arc-melted 5-6 times to ensure homogeneity and subsequently transferred to the General Atomics Center at the University of South Carolina.

Chemical vapor deposition (CVD) SiC (β-phase) (Morgan Advanced Ceramics, Ultra-pure 99.9995%) was used in the diffusion couples as being representative of SiC-SiC composites as these are expected to be produced via chemical vapor infiltration (CVI) and thus will have a CVS SiC surface in contact with the fuel. For experiments using mixed powders, β-SiC powder (Alfa Aesar, 99.8% purity) was employed. The powder particle size was ~1 μm with a reported surface area of 11.5 m^2/g.

A FeCrAl-based alloy foreseen as a likely cladding candidate was selected for the current effort and had a nominal composition of Fe-12%Cr-6%Al-2%Mo-0.2%Y_2O_3 (wt.%). Sample material was prepared and supplied by Oak Ridge National Laboratory (chemical analyses provided in Table 5.1**)**. The alloy will hereafter be referred to as FeCrAl.

Interactions of U_3Si_2 with Zircaloy-4 were also investigated for comparison of cladding performance. Zircaloy-4 alloy was acquired from American Elements Co. as rod ingot with a diameter of 3.18 cm and length of 20 cm, with the provided analysis in Table 5.2.

Table 5.1. Chemical analysis of FeCrAl alloy (%wt).

Element	Content (Wt.%)
Aluminum	6.11%
Carbon	<0.01%
Suffer	<0.005%
Chromium	12.18%
Molybdenum	2.04%
Silicon	0.2%
Yttrium	0.04%

Sections of U_3Si_2, FeCrAl, SiC and Zircaloy-4 (~2 mm thickness for fuel and ~1 mm for cladding material) were cut using a precision, diamond blade saw. The samples were ground and polished, which for U_3Si_2, FeCrAl and Zircaloy-4 was performed with #600 and #1200 mesh silicon carbide paper. The CVD SiC was ground using diamond lapping plates of #600, #1200, #1800 mesh. All materials were sequentially polished using 9 μm, 3 μm, 1 μm and 0.25 μm diamond suspensions. The final polishing (1 μm and 0.25 μm) was conducted inside of a controlled atmosphere glovebox to minimize the formation of an oxide layer. The U_3Si_2/SiC, U_3Si_2/FeCrAl and U_3Si_2/Zircaloy-4 diffusion couples were fixed in a molybdenum jig (hand tightened) prepared inside the glovebox. Tantalum foil was interposed between the molybdenum plates and the samples to avoid potential reactions (Fig. 5.4).

Table 5.2. Chemical analysis of Zircaloy-4 alloy (%wt).

Element	Content
Titanium	0.012%
Tin	1.45%
Carbon	0.018%
Iron	0.21%
Nitrogen	0.0076%
Chromium	0.091%
Hydrogen	0.001%
Hafnium	0.0003%

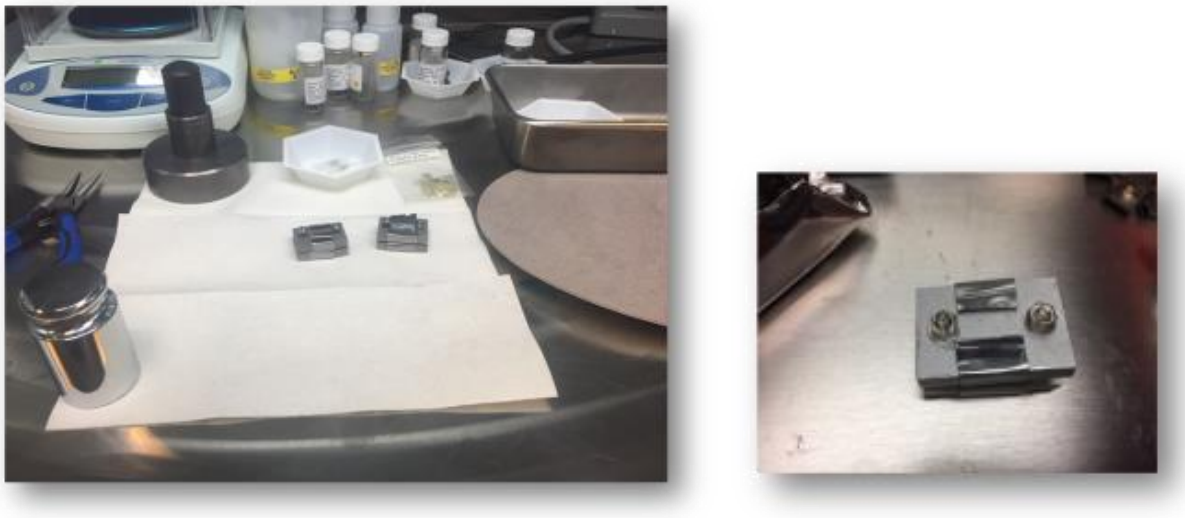

Fig. 5.4. Diffusion couple fixed in a molybdenum-jig inside a glovebox.

Immediately after assembly the samples were transfered to a controlled atmosphere, resistance-heated tube furnace (CM 1730-12HT) for treatment (1000ºC - 1200ºC). High temperature exposures were for times of 10 or 100 hours in flowing argon purified using a GEN'Air oxygen pump (SETNAG) to reduce the gas to 10^{-10} ppm O_2. Additionally, the jig was wrapped in tantalum foil to getter residual oxygen.

To understand the potential for more extensive interactions in the U_3Si_2/SiC system, samples prepared from powder materials were also evaluated. The powder used was a 1:1 molar ratio of mortar and pestle-ground U_3Si_2 and the Alfa Aesar® β-SiC. The powders were blended manually (~ 1 g) and taken to temperature in a simultaneous thermal analyser (STA-409 Netzsch). Exposures were up to 1400ºC for 2h using a heating rate of 5 ºC/min under flowing purified argon (as described for the diffusion couples). The system was used in differential scanning calorimetry mode and the thermal cycle was repeated twice to obtain a base line for correction and detection of the onset temperature of reactions.

Characterization included electron microscopy with phase composition determined by energy dispersive spectroscopy (EDS) using a Tescan Vega 3 scanning electron microscope (SEM) and a Zeiss Ultra plus field emission SEM (FESEM) (Fig. 5.5). Powder X-ray diffraction (XRD) analysis was carried out using a Rigaku Ultima IV instrument with Cu-Kα radiation and a scan of 20-100º at 0.02º/s. Rietveld analyses was performed using MAUD software[78].

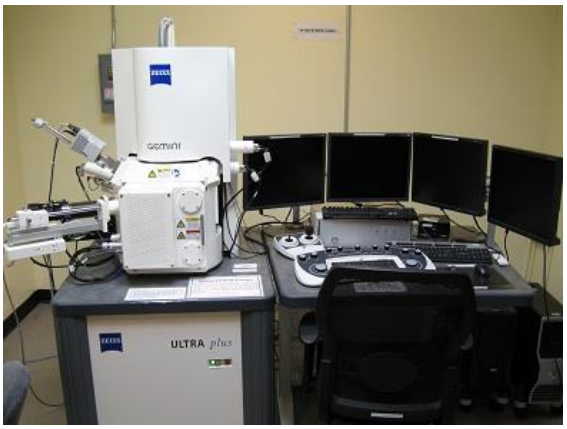

Fig. 5.5. Tescan Vega 2 SEM (a) and Zeiss Ultra plus FESEM (b) instruments used for sample characterization.

5.1.2. Modeling

5.1.2.1. First principles calculations

First principles calculations using density functional theory (DFT) were performed with the Vienna Ab initio Simulation Package (VASP) [79]. The electron exchange correlation was modeled using the PBE approximation[80]. The strong correlation of the 5*f* electrons of uranium required the use of the DFT+*U* method of Dudarev et al. [81]with an effective *U* of 1.5 eV[45]. The unit cells for U_3Si_2, SiC and α-Fe (representing FeCrAl) were fully relaxed using a cut-off energy of 600 eV and forces convergence and total energy electronic convergence criteria of 0.01 eV/Å^{-1} and 10^{-4} eV, respectively. U_3Si_2, SiC and α-Fe supercells were 2x2x4, 3x3x3 and 4x4x4, respectively. A γ-centered Monkhorst-pack k-point spacing of < 0.02 Å^{-1} was used for each structure.

5.1.2.2. Thermodynamic modeling

Computational thermodynamics following the CALPHAD method was used to provide self-consistent Gibbs energy functions optimized using relevant experimental data for a given phase and/or structure[60]. The Gibbs energy functions are combined in a database for use in equilibrium calculations for multi-component systems. Temperature dependent values for the pure elements were obtained from the SGTE database [64] and expressed for a given phase ϕ for element *x* as:

$$ {}^{0}G_x^{\phi} = G_x^{\phi} - H_x^{SER} = a + bT + cT\ln(T) + dT^2 + eT^3 + fT^{-1} + g_nT^n \qquad 5.1$$

where T is temperature in K. In Eq. 5.1 ${}^{0}G_x^{\phi}$ is the Gibbs energy of the element relative to its standard state, G_x^{ϕ} is the Gibbs energy of element *x* in phase ϕ and H_x^{SER} is the molar enthalpy of element *x* in its standard element reference (SER) state at 298.15 K and 10^5 Pa (1 bar). In the case of the elements described here, the standard state phases are α-U (orthorhombic), α-Fe (bcc) and Si (diamond).

Stoichiometric compounds for which there are no reported thermodynamic values have their Gibbs energy, G_{comp}^{ϕ} described by an expression that proportionally combines the values for the elements, adjusted as required to fit observations with an expansion in temperature

$$G_{comp}^{\phi} = a + bT + cTlnT + \sum_i x_i \ {}^0G_i^{\Phi} \quad 5.2$$

where x_i is the mole fraction of element *i* in the phase/compound Φ and the coefficients *a*, *b*, and *c* (when applicable) are adjustable parameters.

The compound energy formalism (CEF) was used to model solid solutions (i.e., those with a finite homogeneity range) by means of a sublattice model. A typical two sublattice model may be described by $(A,B)_m(D,E)_n$, where components A and B mix on the first sublattice and D and E mix on the second sublattice, which are typically exclusively cation or anion containing sublattices, that can also include vacancies. The Gibbs energy includes a term for the reference energy, ideal mixing entropy, energy related to a physical model (e.g., magnetic contribution) and excess mixing energy, which are, respectively, the three right-hand terms below in Eq. 5.3

$$G_m^{\phi} = \sum_i x_i \ {}^0G_i^{\phi} + RT\sum_i x_i \ln(x_i) + \ {}^{phys}G_m^{\phi} + \ {}^{E}G_m^{\phi} \quad 5.3$$

where R is the ideal gas constant. The excess Gibbs energy results from interaction among components *i* and *j* occupying the same lattice sites, and can be expressed as

$${}^{E}G_m^{\phi} = \sum_i \sum_{j>i} x_i x_j \sum_{k=0}^{p} \ {}^kL_{ij}^{\phi} \ (x_i - x_j)^k \quad 5.4$$

where ${}^kL_{ij}^{\Phi}$ are interaction parameters as described by a Redlich-Kister polynomial expansion[82] . The interaction parameters represent additional adjustable parameters for fitting thermochemical data and generally have the form

$${}^kL_{ij}^{\phi} = \ {}^ka_{ij}^{\phi} + \ {}^kb_{ij}^{\phi}T \quad 5.5$$

5.3. Results and Discussion

5.3.1. Experimental

The diffusion tests were conducted in the CM 1730-12HT furnace for 10 h and 100 h at 1000 °C and 1200 °C (Table 5.3). The results for each individual system are presented in the following sections. Where test results are not indicated it is because no interaction was observed.

Table 5.3. List of diffusion couple experiments with annealing times and temperatures.

Sample	Temperature (ºC)	Time (hours)
U_3Si_2/FeCrAl	1000	10
U_3Si_2/FeCrAl	1000	100
U_3Si_2/FeCrAl	1200	10
U_3Si_2/SiC	1000	100
U_3Si_2/SiC	1200	10
U_3Si_2/SiC	1200	100
U_3Si_2/Zry-4	1000	100
U_3Si_2/Zry-4	1200	10

5.3.1.1. Interaction between U_3Si_2 and FeCrAl

The microstructures resulting from the interaction of U_3Si_2 and FeCrAl alloy at 1200ºC/10h and 1000ºC/100h are shown in Fig. 5.6. Phase identification was based on EDS analysis. Significant interactions were observed for both test conditions, resulting in interdiffusion layers with thicknesses of approximately 500μm and 60μm for 1200ºC/10h and 1000ºC/100h, respectively. Both samples show the presence of the ternary phases UFeSi and $UFe_{12-x}Si_x$. Only in the sample annealed at 1200ºC was the U_2Fe_3Si phase observed, which appears as a layer within the interdiffusion zone. These phases appear to progressively form as uranium and silicon are diffusing into the cladding material. At the interface between the interdiffusion zone and U_3Si_2 (area 1, Fig. 5.6a) the U_3Si phase is observed, which indicates that the loss of silicon from the fuel matrix occurs at a faster rate than uranium. The overall result is in general agreement with the observations of Hoggan et al. (2018) of the ternary phases UFeSi and U_2Fe_3Si forming in samples exposed at their higher temperatures of 800ºC-1000ºC. They also state only uranium transports into the FeCrAl, noting indications of the formation of U_6Fe.

In the current work, the sample annealed at 1200ºC/10h exhibits a eutectic phase in the interdiffusion layer adjacent to the cladding (area 2, Fig. 5.6a). EDS analysis indicates this phase has a composition close to UFe_2, as also observed by Hoggan et al.[41], extending into the cladding matrix, perhaps via grain boundary diffusion. This agrees with the report that at >1175ºC γ-Fe + $Fe_2U \rightarrow$liquid[75]. For both test conditions, the interdiffusion layer is seen as symmetric, indicating the diffusion process occurs through mutual elemental exchange between the materials.

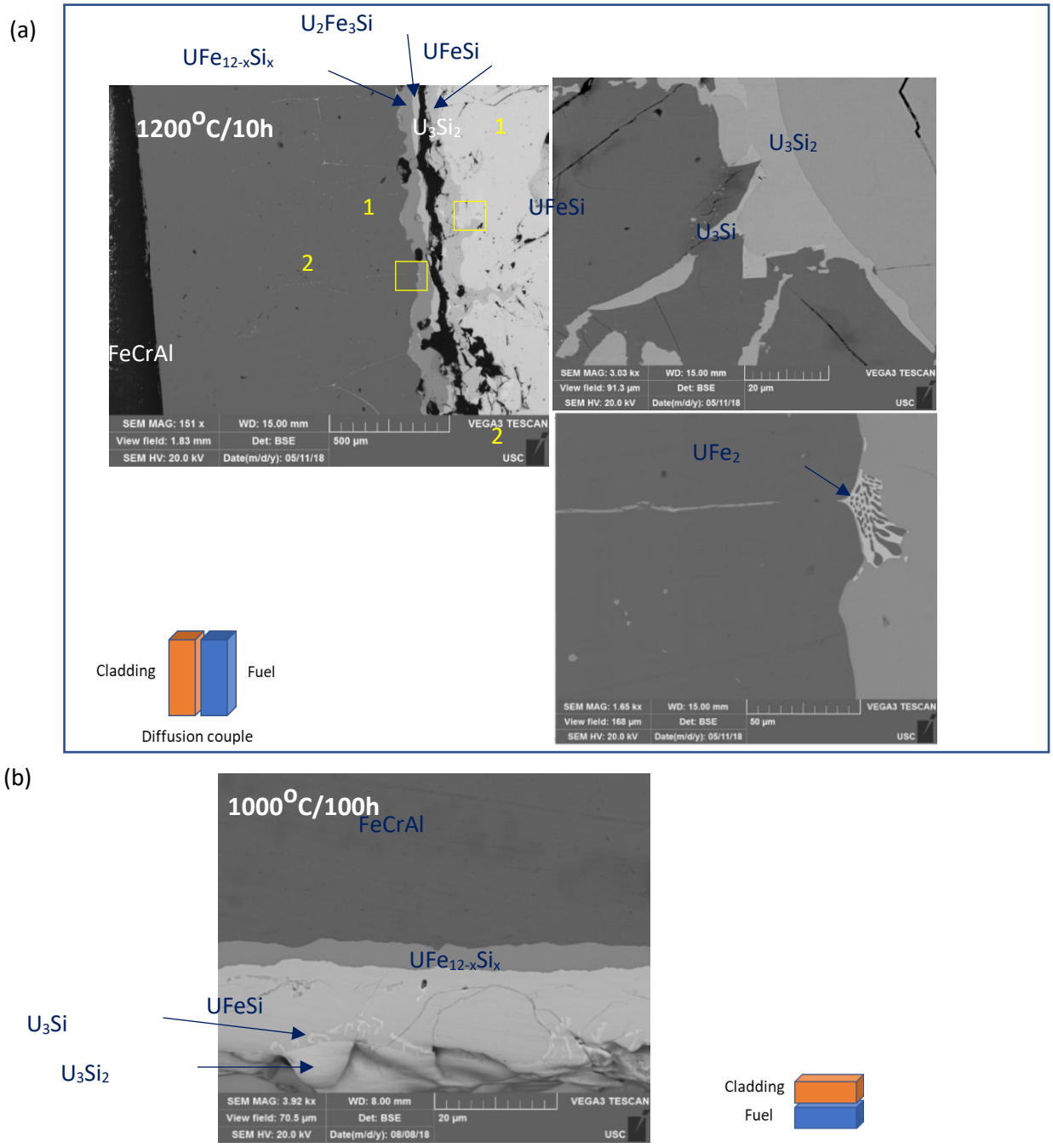

Fig. 5.6. Backscatter electron micrographs of polished cross-sections of the U_3Si_2/FeCrAl diffusion couples held at 1200°C for 10 h (a) and 1000°C for 100 h (b). Illustration of the diffusion couple orientation is shown for reference.

5.3.1.2. Interaction between U_3Si_2 and SiC

The microstructures for the U_3Si_2-SiC diffusion couples annealed at 1200°C/10h and 1200°C/100h are shown in Fig. 5.7. No significant reaction was detected for the sample annealed at 1000°C/100h, and thus it is not shown. The couples separate during the disassembly of the jigs requiring individual analyses

of the interfaces. The interaction between U_3Si_2 and SiC was the least among the fuel-cladding couples evaluated in the present effort. The interdiffusion layer is clearly within the fuel material, implying transport from the cladding into the fuel matrix, which is significantly different from the mechanism for FeCrAl and Zircaloy-4. In the fuel matrix it is possible to observe the presence of U_3Si_5 grains close to the interdiffusion layer surface, with silicon thus diffusing from the SiC. No diffusion into the SiC cladding material was observed, rather only degradation of its surface indicated by it becoming more concave.

To further investigate the phases formed in the representative SiC cladding surface, SEM microstructure analyses and low angle XRD were performed (Fig. 5.8**)**. It is possible to identify two different morphologies (Fig. 5.8b): (i) Large particles with very regular surfaces (10-100μm) and (ii) fine, dispersed material, mainly found in cavities in the SiC surface. Both phases are uranium compounds as they appear in very bright contrast in the SEM images. The larger particles were analyzed by EDS and had an average atomic composition of 52.7%U (±2.8) and 47.3%Si (±2.7). This composition is close to USi, but also possibly the ternary $U_{20}Si_{16}C_3$ as the low atomic number of carbon prevents it from being accessed by EDS. The fine, dispersed phase could not be analyzed by EDS. Low angle XRD yielded peaks that could be related to β-SiC, U_3Si_5, and UC (Fig. 5.8c).

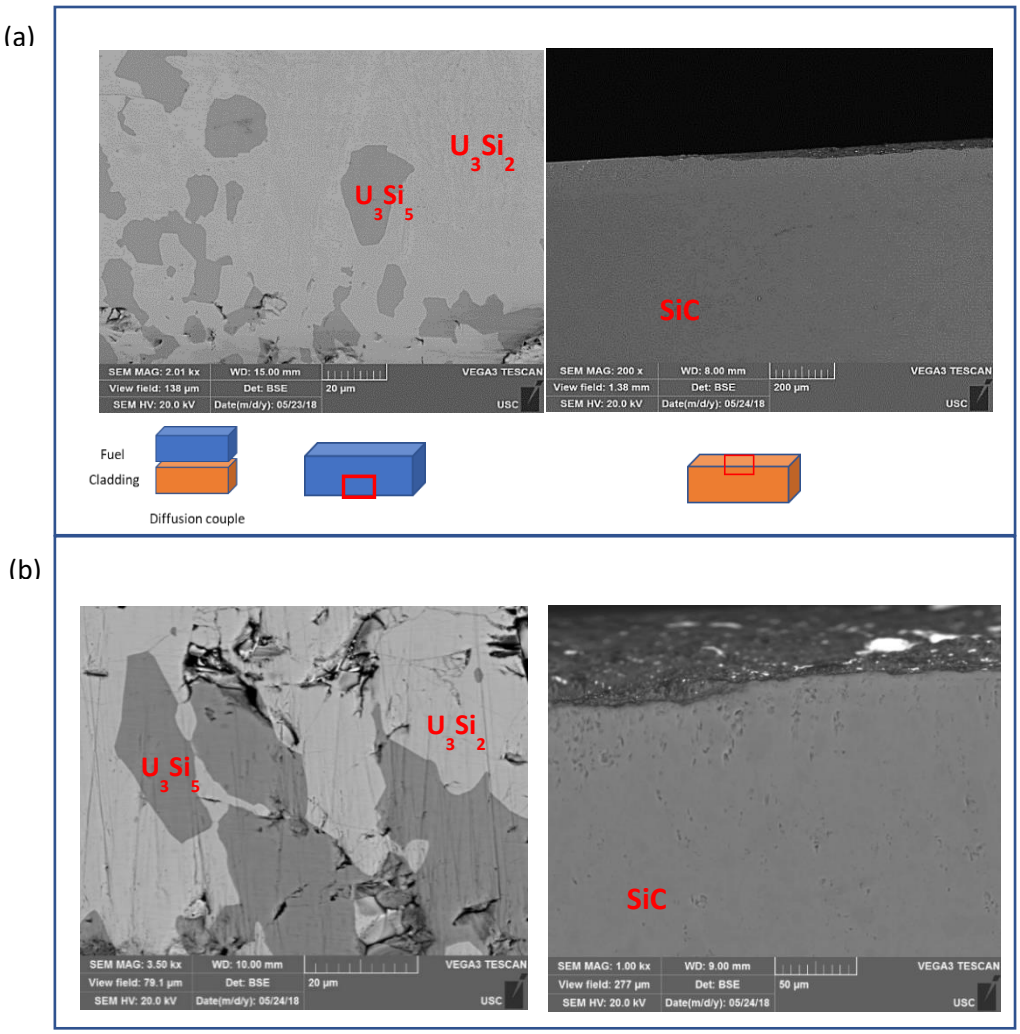

Fig. 5.7. Cross section of the U_3Si_2 and SiC surfaces after exposure at 1200°C for 100 (a) and 10 (b) hours.

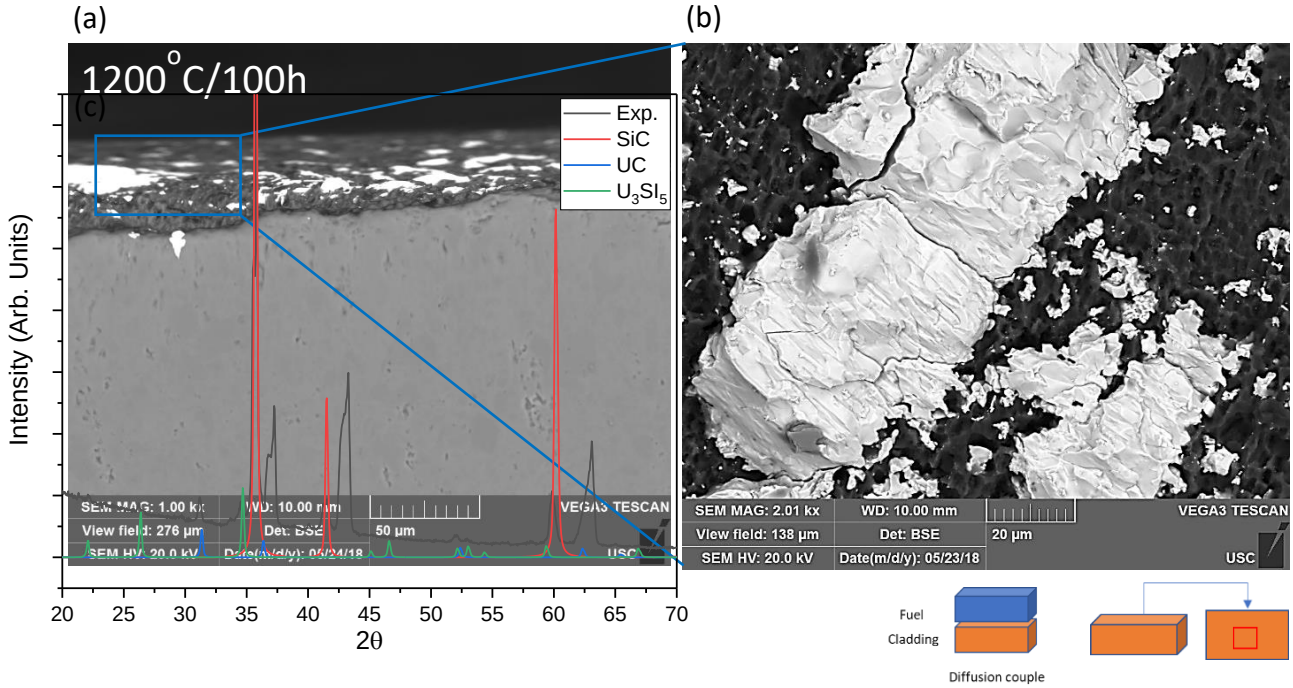

Fig. 5.8. SiC surface SEM micrography (a-b) and low angle XRD (c), for a sample annealed at 1200°C/100h.

It is speculated that the fine, dispersed particles are the UC identified in the low angle XRD patterns as no other features in the SEM images could be so identified. To further investigate the nature of the samples, high resolution SEM images were obtained (Fig. 5.9), revealing the presence of spherical features adhered to the SiC surface. The spherical shape indicates coherent growth with the SiC matrix, and as UC has a fcc lattice similar to that of SiC, it is consistent with such coherent growth. Additionally, the phase is seen to be uranium rich based on the bright contrast found in the backscatter mode.

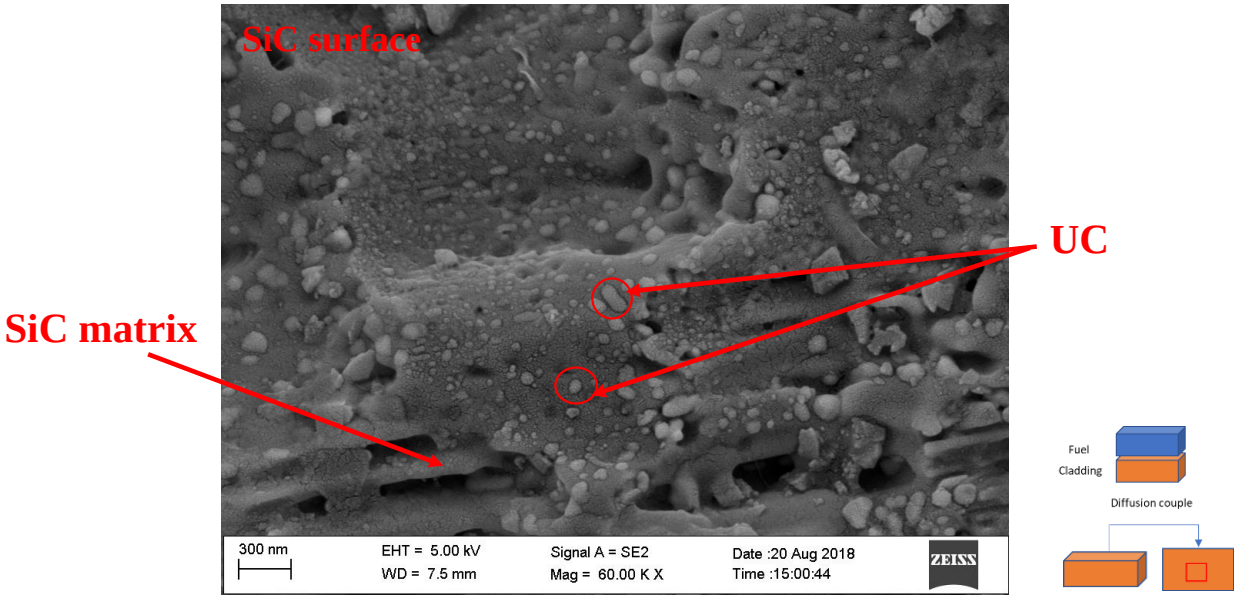

Fig. 5.9. SEM micrograph of a SiC surface after interaction with U3Si2 at 1200oC/100h.

The of 1:1 molar mixture of U_3Si_2:SiC powders was heated to 1400°C and held for 2h in the DSC. Assuming the reactions are irreversible after achieving thermodynamic equilibrium, the samples were subject to two identical thermal cycles, where the second cycle was seen to cause no further reaction. This then provided a baseline for the identification of reaction onset temperatures. XRD analysis was performed before and after the reaction to allow identification of the phases formed. The obtained results are shown in Fig. 5.10 where the thermal trace of Fig. 5.10a indicates an exothermic reaction occurs at ~1135°C, in agreement with the results of the diffusion couple study, and where no significant reaction was observed for the sample heat treated at 1000°C/100h.

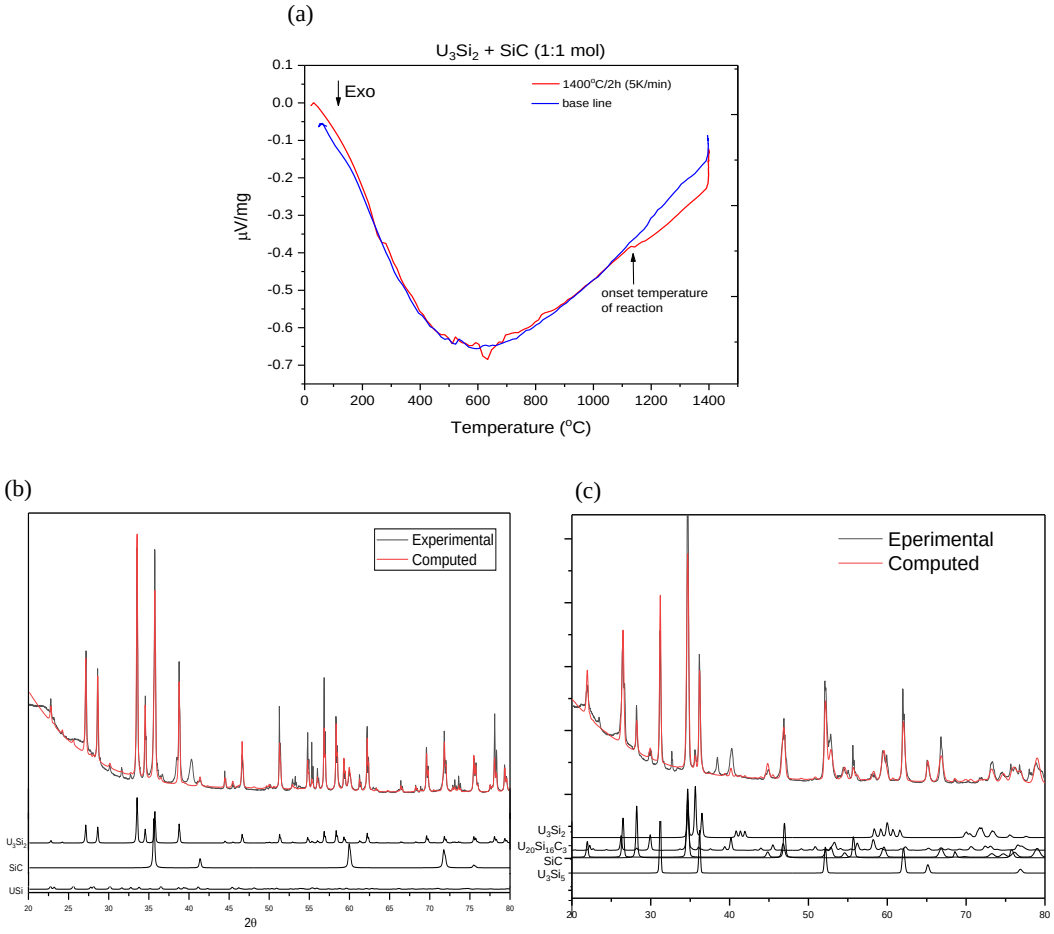

Fig. 5.10. DSC heating profile of U_3Si_2:SiC (1:1 mol) as a function of temperature (a), Rietveld refined x-ray diffraction pattern for the sample before (b) and after (c) thermal cycling.

The XRD analysis before the heating cycle shows major peaks for U_3Si_2 and SiC. A minor amount of USi (FeB-type structure) could be observed, likely the result of the arc-melting of that particular sample. After the heat treatment, the XRD profile indicates U_3Si_5, UC, and a minor amount of $U_{20}Si_{16}C_3$ (~6%) present. This is in good agreement with the phases observed in the diffusion couples and again suggests that the larger particles on the SiC surface might be the ternary phase (Fig. 5.8b**).** Thus results from the mixed powder reactions support formation of $U_{20}Si_{16}C_3$ as a minor phase in high temperature interactions between U_3Si_2 and SiC. Observation of this phase in the diffusion couple sample, however, was difficult to confirm as it likely was contained in the thin brittle layer.

5.3.1.3. Interaction between U_3Si_2 and Zircaloy-4

Representative microstructures of the U_3Si_2/Zircaloy-4 diffusion couples after heat treatment at 1200°C/10h and 1000°C/100h are shown in Fig. 5.11 with very different apparent reactions at the two temperatures. For 1200°C/10h, a temperature above the β-transition of zirconium/Zircaloy-4 [83], a large interdiffusion layer was observed (Fig. 5.11a). Although the samples cracked during the disassembly of the jigs, it is possible to see that there was diffusional bonding of the materials. The fuel surface in contact with the Zircaloy-4 contains the Zr_3Si_2 phase (having the same crystallographic structure as U_3Si_2), illustrating

the stability of this zirconium silicide phase. Uranium significantly diffused into the Zircaloy-4 matrix (~100μm), with the composition of the uranium-containing phase close to that of δ-phase UZr_2 and located mainly in the intergranular regions of the α-Zr (bright phase in Fig. 5.11a). This illustrates the thermodynamic equilibrium favors Zr_3Si_2 and UZr_2 phase formation over the U_3Si_2. The result is important not only in the context of fuel/cladding interaction, but also with respect to the behavior of fission product zirconium, where it can replace uranium lost to fission in the P6/*mmm* lattice and avoid precipitation of a secondary phase.

For the sample annealed at 1000ºC/100h, a temperature below the β-transition of zirconium, significantly less interaction was observed. Only Zr_3Si_2 phase was inidcated at the interface with the fuel (Fig. 5.11b), and no diffusion of uranium into the cladding matrix was detected. Besides the lower temperature reducing mobilities, this may be due to a significantly lower diffusion rate of uranium in hexagonal zirconium as compared to the higher temperature cubic phase, as uranium can more easily diffuse in a bcc structure compared to hcp.

There is some discrepancy between the observations in the current work and those of He et al, [77] for the results at 1000ºC/100h, where He et al. [77]claim substantial uranium mobility and transport into the Zircaloy-4. The main interdiffusion products they indicate are Zr_2Si, U_6Fe, U-Zr-Fe-Ni, U-Zr, and U. Their identification of Zr_2Si, however, could be easily have instead been the Zr_3Si_2 phase observed here as the compositions are not greatly different, and thus agree in this aspect with the current work. Thermochemical calculations at 1000ºC also indicate preferential formation of Zr_3Si_2 over Zr_2Si.

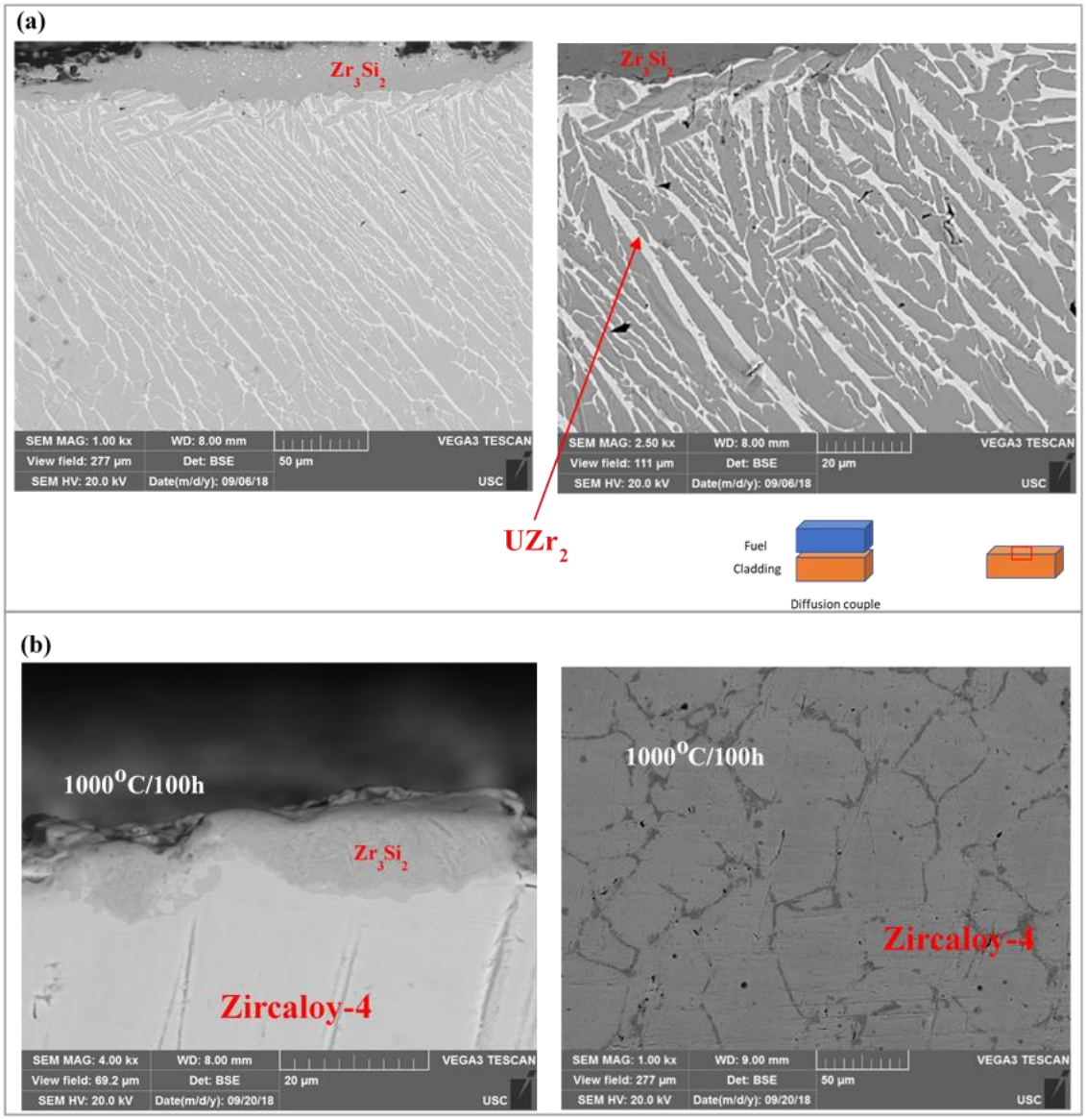

Fig. 5.11. Backscatter electron micrographs from U_3Si_2/Zircaloy-4 diffusion couples annealed at 1200°C for 10 h (a) and 1000°C for 100 h (b). Illustration of the diffusion couple orientation is shown as a reference.

5.3.2. Modeling

5.3.2.1. U-Fe-Si phase diagram modeling

5.3.2.1.1. First principles calculations: *U*-ramping, and Gibbs energy

The lack of DFT+*U* studies of U-Fe-Si ternary phases leaves no reference *U*-value that can be applied[84]. Therefore, it is necessary to determine the *U*-value that best represents the crystal structure (lattice parameters, bond angles, and space group) and magnetic moment of the U-Fe-Si phases. *U*-ramping calculations were thus performed using *U*-values from 0 eV to 3 eV, with a step of 0.2 eV, initially relaxing the structure at $U = 0$ eV. Subsequent calculations utilized the relaxed crystal structure, charge density and

wavefunction from the previous calculation at the lower *U*-value, e.g., for the calculation at $U = 0.2$ eV, the output files from the calculation at $U = 0$ eV are used. The *U*-ramping calculations showed convergence in the lattice parameters and magnetic moment of the U-Fe-Si phases at $U = 1.5$ eV, and thus, the remainder of the calculations used this *U*-value.

DFT calculations provide information for systems only at 0 K, and therefore to evaluate the U-Fe-Si phase diagram at higher temperatures, the phase Gibbs energies needs to be determined at finite temperatures. The total Gibbs energy of a phase is defined as a sum of the DFT calculated total energy at 0 K, *E*, and the entropic contribution to the Gibbs energy, *S*, i.e.,

$$G = E - TS. \tag{5.6}$$

In attempting to determine the Gibbs energy, only the vibrational contribution to the entropy, S_{vib}, was considered, and calculated using:

$$S_{\text{vib}} = k_b \int_0^{\infty} \ln\left[2\sinh\frac{\hbar\omega}{2k_bT}\right] g(\omega)\mathrm{d}\omega \tag{5.7}$$

where ω are the phonon frequencies, $g(\omega)$ is the phonon density of states (DOS), and ħ is the reduced Planck constant. For each of the studied ternary phases, the phonon DOS were calculated using the code Phonopy [85] with the density functional perturbation theory (DFPT) formalism as implemented in VASP. A kinetic energy cut-off of 725 eV helped avoid small negative frequencies around the Γ point in tests run on U-Si systems. The calculated total Gibbs energies, obtained using Eq. 5.6, were subsequently used in thermodynamic modeling to generate a U-Fe-Si phase diagram, as detailed in the next section.

5.3.2.1.2. Chemical thermodynamic modeling

While 11 ternary phases have been identified in the U-Fe-Si system there are no reported thermodynamic values for the phases. As noted, prediction of behavior requires understanding relative stabilities and preferably the ability to compute phase formation, which requires a set of such values. Fortunately, as noted, the constituent binary systems have been well-characterized, including thermodynamic assessments. These provide the basis for modeling the stoichiometric phases using a Neumann-Kopp type algebraic sum of values for the elements. The resultant summed values for each ternary composition was adjusted as needed to reflect its stability relative to other phases, modifying either or both the *a* and *b* terms of Eq. 5.7, to reproduce the phase equilibria of Fig. 5.3.

The solid solution phase $UFe_{12-x}Si_x$ with $1<x<3$ ($ThMn_{12}$ structure) was modeled using the compound-energy formalism based on a three sublattice model analogous to that of Zinkevich et al. [86]considering the composition range investigated by Goncalves et al.[87]. In this case, however, a four sublattice model was seen as necessary to describe dissolution of silicon and the non-stoichiometry generated by site vacancies in the $ThMn_{12}$-structured UFe_{12} end-member

$$(U)_2(Fe)_{16}(Fe,Va)_2(Fe,Si)_6$$

where Va indicates neutral vacancies. The structure is represented by a 26 atom unit cell with two formula units per unit cell. As the third and fourth sublattices can contain either differing elements or an element and a vacancy, they provide for deviation in stoichiometry.

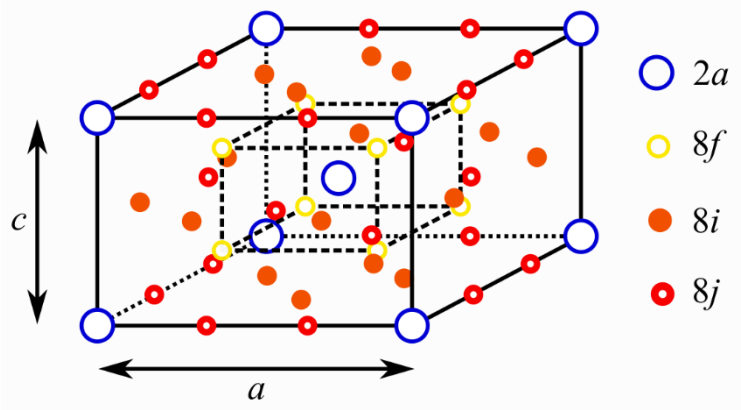

Fig. 5.12. $ThMn_{12}$-type crystal structure for $UFe_{12-x}Si_x$.

The Gibbs energy for the solution phase is described by

$$G = (1-y_{Va})y_{Fe}\,\mathbf{G_{U:Fe:Fe:Fe}} + y_{Va}y_{Fe}\,\mathbf{G_{U:Fe:Va:Fe:Fe}} + (1-y_{Va})y_{Si}\,\mathbf{G_{U:Fe:Fe:Si}} + y_{Va}y_{Si}\,\mathbf{G_{U:Fe:Va:Si}} + 6\,(y_{Fe}\ln(y_{Fe}) + (y_{Si}\ln y_{Si}) + 2\,RT\,[(1-y_{Va})\ln(1-y_{Va}) + y_{Va}\ln y_{Va}] + y_{Fe}y_{Si}(1-y_{Va})\,\mathbf{L_{U:Fe:Fe:Fe,Si}} + y_{Fe}y_{Si}y_{Va}\,\mathbf{L_{U:Fe:Va:Fe,Si}} \quad 5.8$$

The four possible combinations of occupied sites on the four sublattices provide for the four endmembers: $\mathbf{G_{U:Fe:Fe:Fe,}}$ represents the UFe_{12} endmember where U and Fe are occupying the first and second sublattice, respectively, (as is the case for all the endmembers), and the third and fourth are occupied with Fe; $\mathbf{G_{U:Fe:Va:Fe}}$, represents the endmember composition where the third sublattice contains a vacancy and the fourth contains Fe, corresponding to UFe_{11}; $\mathbf{G_{U:Fe:Fe:Si,}}$ has the third sublattice occupied with Fe and the fourth with Si, and thus has the composition UFe_9Si_3; and $\mathbf{G_{U:Fe:Va:Si}}$ is an endmember where Si and Va reside on the third and fourth sublattice, respectively, corresponding to UFe_8Si_3. The interaction parameter **L** represents the energetics of interactions between Fe and Si on the fourth sublattice. The term $y_{Va,}$ is the vacancy site occupancy on the third sublattice and y_{Fe} and y_{Si} are the occupancies of Fe and Si on the fourth sublattice, respectively. The constraint of maintaining charge neutrality is applied to determinations of site occupancies. The Gibbs energies of the four endmembers are determined from algebraic sums of constituent elements and are adjusted together with the **L** terms to achieve optimal agreement with experimental measurements and phase equilibria, together with the results of the first principles calculations.

The derived and fitted Gibbs energy parameters, including those of the stoichiometric line compounds, are listed in Table 5.4, with the corresponding computed ternary phase diagram at 900 ℃ depicted in Fig. 5.13. No interaction parameters have as yet been derived for the solid solution phase, as further work is needed to refine the compositional dependence of the $UFe_{12-x}Si_x$ phase. The tielines in the calculated phase diagram are in relatively good agreement with those observed experimentally as seen in Fig. 5.3.

*Table 5.4. Gibbs energy parameters for U-Fe-Si compositions.**

Label	Phase	Parameter	(values in SI: J,mol,K)
A	U_2FeSi_3	${}^0G_{U:Fe:Si}$	-339,750-3*T + 2*GHSERU + GHSERFE + 3*GHSERSI
B	UFe_2Si_2	${}^0G_{U:Fe:Si}$	-266,100 + GHSERU + 2*GHSERFE + 2*GHSERSI
C	$U_3Fe_2Si_7$	${}^0G_{U:Fe:Si}$	-578,600 + 3*GHSERU + 2*GHSERFE + 7*GHSERSI
D	U_2Fe_3Si	${}^0G_{U:Fe:Si}$	-231,800 + 2*GHSERU + 3*GHSERFE + GHSERSI
E	$UFe_{12-x}Si_x$	${}^0G_{U:Fe:Fe:Fe}$	2GHSERU+GHSERFE+GHSERSI
E	$UFe_{12-x}Si_x$	${}^0G_{U:Fe:Va:Fe}$	-475000 + 325*T + 2*GHSERU + 24*GHSERFE
E	$UFe_{12-x}Si_x$	${}^0G_{U:Fe:Fe:Si}$	-425000 - 390*T + 2*GHSERU + 18*GHSERFE + 6*GHSERSI
E	$UFe_{12-x}Si_x$	${}^0G_{U:Fe:Va:Si}$	+ 2*GHSERU + 16*GHSERFE + 6*GHSERSI
E	$UFe_{12-x}Si_x$	${}^0L_{U:Fe:Fe:Fe,Si}$	0
E	$UFe_{12-x}Si_x$	${}^0L_{U:Fe:Va:Fe,Si}$	0
G	UFeSi	${}^0G_{U:Fe:Si}$	-151,100+ GHSERU + GHSERFE + GHSERSI
H	$U_{1.2}Fe_4Si_{9.7}$	${}^0G_{U:Fe:Si}$	-4,673,700 + 12*GHSERU + 40*GHSERFE + 97*GHSERSI
I	$U_2Fe_3Si_5$	${}^0G_{U:Fe:Si}$	-509,000 + 2*GHSERU + 3*GHSERFE + 5*GHSERSI
J	UFe_5Si_3	${}^0G_{U:Fe:Si}$	-371,300 + GHSERU + 5*GHSERFE + 3*GHSERSI
K	$U_6Fe_{16}Si_7$	${}^0G_{U:Fe:Si}$	-1,192,000 + 6*GHSERU + 16*GHSERFE + 7*GHSERSI

* The standard reference states values are indicated by GHSERFE for G_{Fe}^{FCC},GHSERSI for $G_{Si}^{diamond}$ and GHSER for $G_U^{orthorhombic}$ for α-U.

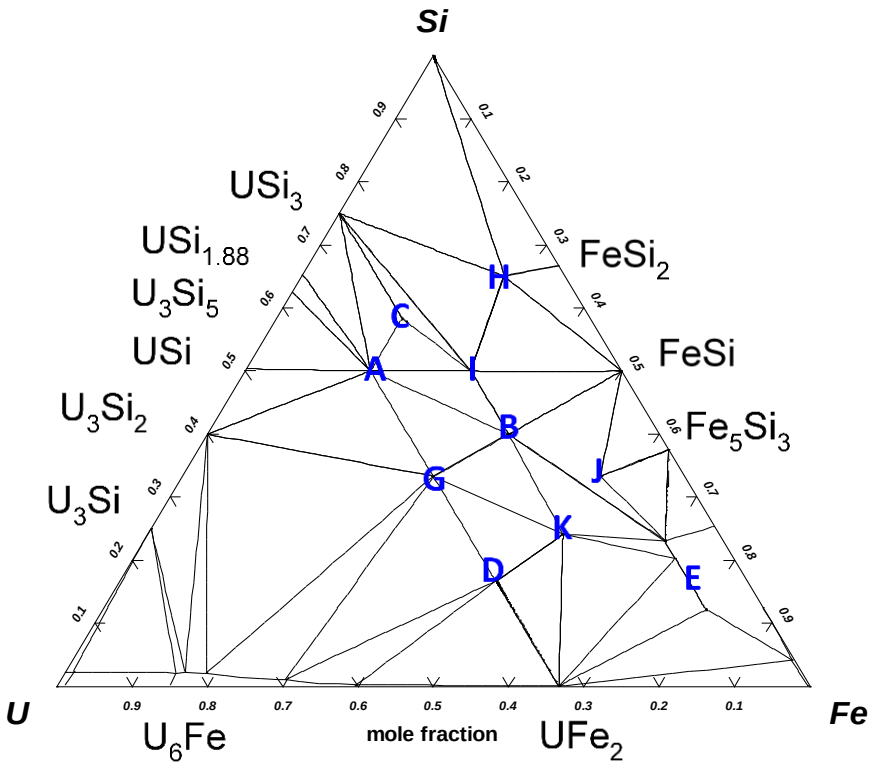

Fig. 5.13. U-Fe-Si ternary isotherm at 900 C calculated using the parameters in Table 5.4.

For comparison, DFT calculated formation enthalpies for 8 of the stoichiometric phases are listed in Table 5.5 (compound H was excluded as partial occupancies in the structure cause the unit cell to be overly large, thus making the calculations prohibitive). For a number of the phases the adjusted Neumann-Kopp estimated values are in good agreement with the *ab-initio* results. Note that the CALPHAD values are reported at the standard state temperature 298.15K, whereas the DFT results are for 0K, which can be the source of some of the discrepancies.

Table 5.5. Comparison of enthalpies of formation for U-Fe-Si compounds calculated using CALPHAD and DFT methods. Units are kJ/mol.

Label	Phase	$\Delta_f H^\circ_{298.15}$ CALPHAD	$\Delta_f H^\circ_{0K}$ (DFT)
A	U_2FeSi_3	-330.6	-216.5
B	UFe_2Si_2	-247.8	-252.3
C	$U_3Fe_2Si_7$	-560.3	-514.1
D	U_2Fe_3Si	-204.4	-224.2
E	$UFe_{12-x}Si_x$	N/A	N/A
G	UFeSi	-142.0	-133.2
H	$U_{1.2}Fe_4Si_{9.7}$	-430.8	N/A
I	$U_2Fe_3Si_5$	-481.6	-481.5
J	UFe_5Si_3	-325.6	-371.7
K	$U_6Fe_{16}Si_7$	-1045.6	-1085.6

5.3.2.1.3. Atomistic modeling of fuel-cladding interactions

Defect formation energies in U_3Si_2, and the SiC and FeCrAl cladding were evaluated by modeling interactions, as well as determining incorporation energies for fuel atoms in the cladding, and cladding atoms in the fuel. The calculations were performed using 2×2×4, 3×3×3 and 4×4×4 supercells of U_3Si_2, SiC and the FeCrAl alloy representated by α-Fe, respectively. Modeling the incorporation of carbon, iron and silicon in the U_3Si_2 structure was performed considering the two uranium sites, a silicon site (only for exchange with carbon and iron), and 10 interstitials sites with Wyckoff positions: 2b, 2c, 2d, 4e, 4f, 4g, 4h, 8i, 8j and 8k (Fig. 5.14a). The incorporation of uranium and excess silicon in SiC were modeled considering the silicon and carbon sites, and two interstitial positions (Fig. 5.14b). The incorporation of uranium and silicon in α-Fe considered the iron site and one interstitial position (Fig. 5.14c). For uranium diffusion into the cladding materials, an on-site correlation with an effective *U*=1.5 eV, was applied for SiC, with no correlation used for α-Fe. The interstitial defects created in the U_3Si_2 and cladding materials SiC and α-Fe are shown as red spheres in Fig. 5.14**.**

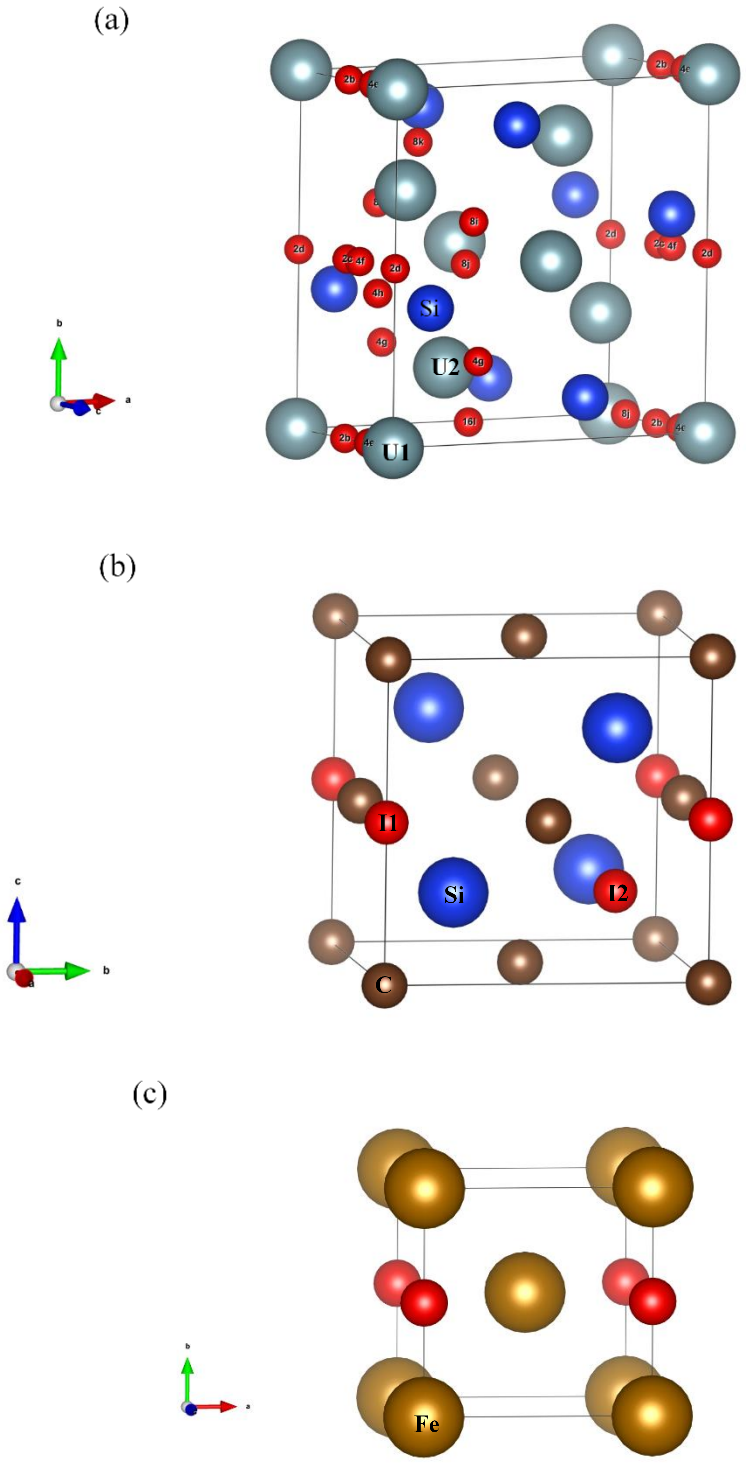

Fig. 5.14. Interstitial sites (red spheres) in U_3Si_2 (a), SiC (b) and α-Fe (c) structures treated as point defects in first principle calculations.

Incorporation, ΔE_{inc}, and point defect, ΔE_D, formation energies were calculated using Eq. 5.9 and Eq. 5.10, respectively:

$$\Delta E_{\text{inc}} = E^D_{\text{tot}} - E^{\text{vac}}_{\text{tot}} - \sum_{i=1}^{N} \Delta N_i^D \mu_i^0 \quad 5.9$$

$$\Delta E_D = E^D_{\text{tot}} - E^0_{\text{tot}} - \sum_{i=1}^{N} \Delta N_i^D (\mu_i^0 + \Delta\mu_i) \quad 5.10$$

where E^D_{tot}, $E^{\text{vac}}_{\text{tot}}$, and E^0_{tot} are the DFT computed total energies of the supercells with a defect, with a defect site vacancy, and without a defect, respectively. The sum in the Eq. 5.10 is over all species, *i*, in the supercell (U, Si, C and Fe depending on the evaluated system/defect). ΔN^D_i is the number of atoms of type *i* added to ($\Delta N^D_i > 0$) or removed ($\Delta N^D_i < 0$) from the perfect supercell to create the defect, with μ^0_i the chemical potential of the standard state elemental species *i*, here α-U, C as graphite, Si in the diamond structure, and α-Fe. $\Delta\mu_i$ is the change in the chemical potential due to changes resulting from defect formation in a *N*-phase equilibrium. The $\Delta\mu_i$ can be calculated using a set of linear equations, as shown in Eq. 5.11

$$\Delta H_{f,k} = \sum_{i=1}^{N} c_{ik} \Delta\mu_i \quad 5.11$$

where the $\Delta H_{f,k}$ is the formation enthalpy of the specific phase *k*, and c_{ik} is the elemental content of the specific phase. The formation enthalpies of the phases used to obtain $\Delta\mu_i$ values in the present work are detailed in Table 5.6.

Table 5.6. Formation enthalpies, ΔH_f, of compounds in U-Si-C and U-Si-Fe phase space used in computing chemical potential change, $\Delta\mu_i$.

Phase	Computed ΔH_f (eV/atom)	Tabulated* ΔH_f (eV/atom)*	Difference (comp. – tab.)	Calculation method
U_3Si_2	-0.3298	-0.3538	-0.0240	GGA+U
USi	-0.4535	-0.4335	0.0200	GGA+U
UC	-0.4459	-0.5055	-0.0596	GGA+U
SiC	-0.2063	-0.3465	-0.1402	GGA
$U_{20}Si_{16}C_3$	-0.4502	-0.4450	0.0052	GGA+U
$U_3Si_2C_2$	-0.3733		0.3733	GGA+U
UFeSi	-0.4824	-0.4581	0.0243	GGA+U
UFe_2	-0.1120	0.1113	0.2233	GGA
$UFe_{11}Si_1$	-0.1998		0.1998	GGA+U
U_2Fe_3Si	-0.3421	-0.4000	-0.0579	GGA+U
U_3Si	-0.2189	-0.3490	-0.1301	GGA+U
U_3Si_5	-0.4808	-0.4480	0.0328	GGA+U
Fe_3Si	-0.3170	-0.3145	0.0025	GGA

*[88]

Optimal total energies require using the *U*-value that best represents the structure and the electron correlation in a system. For example, the total energy for α-U was calculated using just the GGA approximation, i.e., $U = 0$ eV, as it best represents the phase[89], while it has been shown that the lowest value that best represent U_3Si_2 phonons is $U = 1.5$ eV[45]. However, because of the use of different *U*-values, the resulting ΔH_f values cannot be directly compared. Therefore, to allow consistent comparison of ΔH_f for all phases the methodology for correcting ΔH_f developed by Jain et al. [90]was applied.

5.3.2.1.4 Modeling U-Si–Fe interactions

Incorporation energies for Fe in U_3Si_2, and for U and Si in α-Fe were computed and are listed in Table 5.9**.** They indicate that Fe incorporation in crystalline U_3Si_2 as well U and Si in incorporation in α-Fe are energetically favored, i.e., have negative incorporation energies. This affinity for dissolving the elements in these phases is consistent with the reported phase diagram[75].

Table 5.7. Calculated incorporation energies, for Fe in U_3Si_2; and for U and Si in α-Fe. The references states used are the chemical potential of α-U, α-Fe and Si (diamond structure). The relaxations that lead to another position are maked as "Not stable." The ones that converge for a different stable position are shown in the third column, "Other Position." Negative values indicate energetically favorable incorporation.

Point defect in crystalline U_3Si_2	**E_{inc} (eV)**	**Other Position**
Fe substitutional U1	**-0.55**	
Fe substitutional U2	**-1.01**	
Fe substitutional Si	**-1.10**	
Fe interstitial site 2b	**-0.73**	
Fe Interstitial site 2c	Not stable	**-0.30** (relaxed Si-Si interstitial)
Fe Interstitial site 2d	Not stable	
Fe Interstitial site 4e	Not stable	
Fe Interstitial site 4f	Not stable	Relaxed to Si-Si
Fe Interstitial site 4g	Not stable	
Fe Interstitial site 4h	Not stable	
Fe Interstitial site 8i	Not stable	
Fe Interstitial site 8j_1	Not stable	Relaxed to 2b
Fe Interstitial site 8j_2	Not stable	Relaxed to 2b
Fe Interstitial site 8k	Not stable	
Point defect in crystalline α-Fe	**E_{inc} (eV)**	
U substitutional Fe	**-2.37**	
Si substitutional Fe	**-3.41**	
U interstitial	4.66	
Si interstitial	3.62	

It is also evident that Fe can be incorporated in the U_3Si_2 lattice in different existing sites, such as both uranium sites (U1 and U2), the silicon site and in two interstitial sites. Of the two uranium sites, the more stable position for Fe is U2 (where the U atom is surrounded by Si atoms), The energy for Fe substituting for Si is only 84 meV more positive than for it to be incorporated into a U2 site so it too is a good candidate for hosting Fe. Thus, the U2 and Si site vacancies represent very stable traps for iron atoms in U_3Si_2. The results in Table 5.7 also demonstrate that substitution of uranium and silicon for iron in α-Fe is energetically favored, but the formation of interstitials is not. These calculated negative mutual incorporation energies for fuel and cladding elements support the trend of mutual exchange noted in the experiments.

The formation energies of the point defects in U_3Si_2 and α-Fe using chemical potentials derived for the various phase assemblages from Eq. 5.10 and Eq. 5.11, were computed and are shown in Table 5.8.

Table 5.8. Formation energies of point defects in the U_3Si_2 fuel and α-Fe cladding under sets of chemical potentials derived for each of the indicated three-phase equilibria proposed across the interfacial region between the two single-phase fuel and cladding regions.

	Formation energies of point defects (eV)			
	Three-phase equilibria			
Point defect in U_3Si_2	U_3Si_2-αFe-UFeSi	U_3Si_2-αFe-U_2Fe_3Si	U_3Si_2-αFe-$UFe_{11}Si$	U_3Si_2-UFeSi-U_3Si*
U1 vacancy	2.18	**-1.52**	4.48	0.90
U2 vacancy	3.52	**-0.18**	5.82	2.24
Si vacancy	**-0.83**	4.72	**-4.28**	1.08
Fe substitutional U1	1.63	**-2.07**	3.93	0.99
Fe substitutional U2	2.51	**-1.19**	4.81	1.87
Fe substitutional Si	**-1.93**	3.62	**-5.38**	0.63
Fe interstitial site 2b	**-0.73**	**-0.73**	**-0.73**	**-0.09**
Fe intertital site Si-Si	**-0.30**	**-0.30**	**-0.30**	0.34
Point defect in α-Fe	U_3Si_2-αFe-UFeSi	U_3Si_2-αFe-U_2Fe_3Si	U_3Si_2-αFe-$UFe_{11}Si$	αFe -$UFe_{11}Si$-UFe_2*
Fe vacancy	2.06	2.06	2.06	2.06
U substitutional Fe	**-1.56**	2.14	**-3.86**	**-0.92**
Si substitutional Fe	1.34	**-4.21**	4.79	**-1.22**

* Fuel and cladding not in contact.

Phase assemblages that contain both fuel (U_3Si_2) and cladding (α-Fe) together with a third phase assumed to form from initial interactions are listed in the second, third and fourth colums in Table 5.7. The phase space where those with adjacent compositions replace either the fuel or cladding in the three-phase equilibria (marked with * in Table 5.8) are indicated in the fifth column. These phase assemblages represent the condition where the fuel and cladding are no longer in contact due to formation of intermediate phases, with interactions proceeding until incorporation energies approach zero or become positive, and thus there is no longer a driving force for reaction.

From the analysis, it is observed that the same types of defects are favored when the phases UFeSi and $UFe_{11}Si$ are considered in the equilibrium as when the ternary phases are omitted. These phases drive the incorporation of iron in Si sites and 2b and Si-Si interstitial sites of U_3Si_2, as well as incorporation of uranium in α-Fe. These defects the ternary phases by removing Si, thus depleting U_3Si_2, while the cladding moves toward a uranium-containing composition. This drives the system to the equiulibrium phase assemblages of U_3Si_2-U_3Si-UFeSi and UFe_2-Fe-$UFe_{11}Si$, in good agreement with what has been here experimentally observed.

When the formation of U_2Fe_3Si is considered as the intermediate phase phase between U_3Si_2 and α-Fe, a shift in the stability of defects in the fuel and cladding material occurs, where now the substitution of iron for uranium in U_3Si_2, and incorporation of Si in α-Fe are favored. The change in the nature of the stable defects appears related to the U:Si ratio of the ternary phase, where equilibria with $UFe_{11}Si$ and UFeSi favors uranium substitution in α-Fe while formation of U_2Fe_3Si promotes silicon incorporation in α-Fe. The current observed behavior together with the computed results suggest UFeSi and $UFe_{11}Si$ phases are likely initial phases formed due to fuel-cladding interactions, while the U_2Fe_3Si is expected to arise from the interaction with other ternary phases.

When the α-Fe is replaced by U_3Si such that the phase equilibria of U_3Si_2-UFeSi-U_3Si is considered as controlling the chemical potential on the fuel side of the system, the computed defect energies in the fuel approach zero or become positive, removing the driving force for interdiffusion and thus interactions. Similarly, replacement of the U_3Si_2 by UFe_2, and thus formation of the UFe_2-αFe-$UFe_{11}Si$ phase assemblage

as would occure on the cladding side, also results in decreased defect energies, in agreement with the observed absence of the fuel elements uranium and silicon within the FeCrAl cladding.

5.3.2.1.5 Modeling U_3Si_2-SiC interaction

U_3Si_2 and SiC interactions were investigated by determining mutual incorporation energies calculated using DFT (Table 5.9). The results indicate Si can substitute for U in U_3Si_2, occupying the U1 site, and shift the position of the U2 site and the interstitial 2b site. This is consistent with reported U-Si phase equilibria and previous calculations of the slope of the convex hull, with minima close to the high silicon region for U_3Si_5 and USi_2 [45, 91]. The relatively lower interstitial site incorporation energy reflects the lesser energy needed as compared to substitutional mechanisms.

Carbon incorporation in U_3Si_2 was found to occur only at the interstitial 2b site. This was also seen in the relaxation of the 8j interstitial sites (similar incorporation energy). The interstitial position between two Si atoms, termed the Si-Si interstitial, is the second most energetically favorable Si interstitial position, found from the relaxation of the 2c and 4f interstitial sites, with the incorporation energy being slightly positive. The short bond distance and related negative incorporation energies for C in the two interstitial sites can play a key role in carbon transport in the material. Consequently, one of the possible diffusion pathways for C in U_3Si_2 may be via these two interstitial sites, as depicted in Fig. 5.15a.

Table 5.9. Calculated incorporation energies of Si and C in U_3Si_2; and U and Si in SiC. The references states used are the chemical potential of α-U, SiC (fcc) and Si diamond structure. The relaxations that lead to another position are maked as "Not stable". The ones that converge to another stable position are shown in the third column. Negative values indicate the defect is energetically favored.

Type of point defect: U_3Si_2	**E_{inc} (eV)**	**Other Position**
Si substitutional U1	**-1.20**	
Si substitutional U2	Not stable	**-1.28**
Si interstitial site 2b	**-0.97**	
Si interstitial site Si-Si	0.90	
C substitutional U1	Not stable	0.74
C substitutional U2	Not stable	0.37
C substitutional Si	0.46	--
C interstitial site 2b	**- 0.97**	--
C Interstitial site 2c	Not stable	0.08 (Si-Si interstitial)
C Interstitial site 2d	Not stable	0.38
C Interstitial site 4e *	---	---
C Interstitial site 4f	Not stable	0.09 (Si-Si interstitial)
C Interstitial site 4g	Not stable	0.92
C Interstitial site 4h *	---	---
C Interstitial site 8i	Not stable	6.74
C Interstitial site 8j_1	Not stable	**-1.06 (relaxed 2b)**
C Interstitial site 8j_2	Not stable	**-1.03 (relaxed 2b)**
C Interstitial site 8k *	Not stable	---
Type of point defect: SiC	**E_{inc} (eV)**	**Other Position**
U substitutional Si	**-2.97**	---
U substitutional C	Not stable	6.29
Si substitutional C	**- 0.69**	---
C substitutional Si	**- 4.45**	---
U Interstitial_1	Not stable	12.82
U Interstitial_2	14.55	---
Si Interstitial_1	4.87	---
Si Interstitial_2	8.52	---

In SiC, uranium can substitute for Si, forming a chemical environment very similar to that of the UC phase (Fig. 5.15b), and may be the mechanism governing the formation of the observed UC. Anti-site defects are also found to be energetically stable. As other defect formation energies are significantly positive for SiC, the anti-site defect mechanism can play an important role, creating defects to promote interaction/secondary phases.

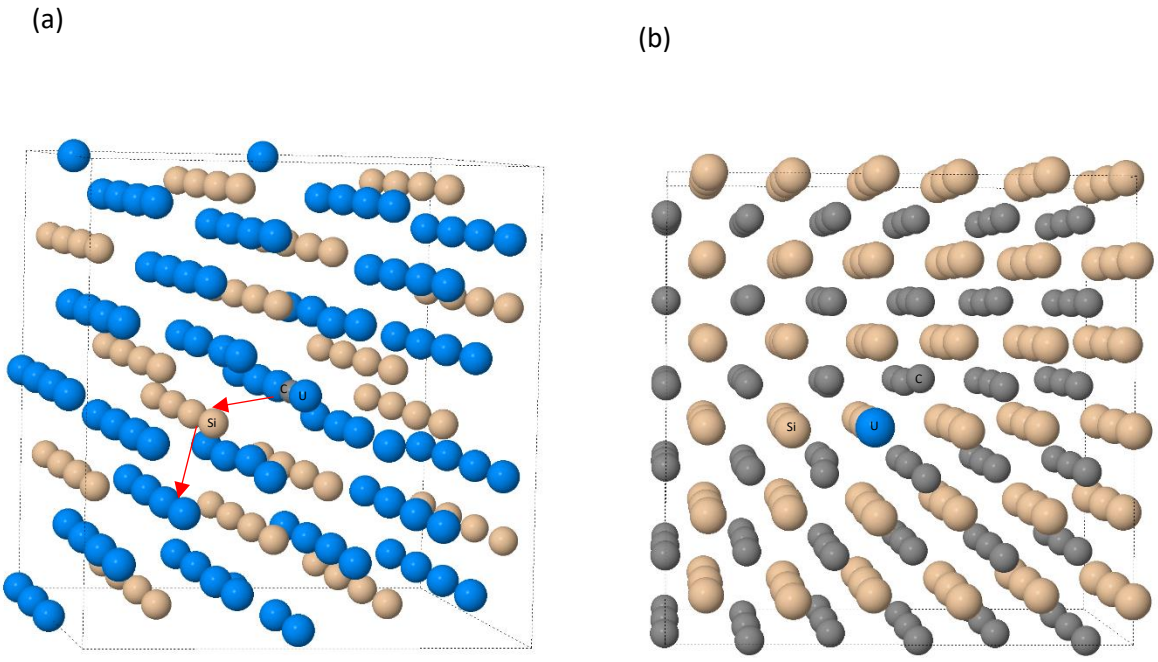

Fig. 5.15. Depictions of possible carbon incorporation in the interstitial position 2b in U_3Si_2 and a possible migration path via 2b and Si-Si interstitials (a); stable position of uranium substituting for silicon in the SiC lattice, creating a chemical environment similar to that for UC (b).

Following the method employed to understand the U_3Si_2/FeCrAl interactions, the chemical potential was allowed to vary at equilibrium to calculate defect formation energies for U_3Si_2 and SiC (Table 5.10)**.** The results demonstrate that for the U_3Si_2-SiC-$U_{20}Si_{16}C_3$ equilibria (second column in Table 10), Si defects in U_3Si_2 matrix should spontaneously form. Excess Si will substitute for the uranium plus occupy two interstitial positions, increasing the silicon content of fuel in contact with the SiC cladding and thus forming phases such as USi and U_3Si_5. The same energetics favor formation of carbon vacancies in SiC, as well as anti-site defects, i.e., Si occupying C sites. The energetics also explain why there is no evidence of diffusion of uranium in SiC, and the observed formation of UC exclusively on the SiC surface.

A shift of the phase equilibria to U_3Si_2-SiC-$U_3Si_2C_2$ (third column in Table 5.10) makes all defects much less favorable in both fuel and cladding. These results may indicate that $U_{20}Si_{16}C_3$ is an intermediate phase in the fuel-cladding system, preventing further interactions. The experimental and modeling results suggest that initially $U_{20}Si_{16}C_3$ forms by interstitial carbon incorporation in U_3Si_2, followed by transport of Si into U_3Si_2. Carbon site vacancies in SiC makes Si anti-site defects possible, which promotes formation of UC in the surface of SiC material.

Table 5.10. Formation energies of point defects in the U_3Si_2 fuel and SiC cladding under sets of chemical potentials fixed by each of the three-phase equilibria in U-Si-C system.

	Formation energies of point defects (eV)			
	Three-phase equilibria			
Type of point defect in U_3Si_2	U_3Si_2-SiC-$U_{20}Si_{16}C_3$	U_3Si_2-SiC-$U_3Si_2C_2$	U_3Si_2-$U_{20}Si_{16}C_3$-U_3Si_5*	U_3Si_2-$U_3Si_2C_2$-U_3Si_5*
U1 vacancy	**-10.27**	0.34	0.87	0.87
U2 vacancy	**-8.93**	1.68	2.22	2.22
Si vacancy	17.84	1.93	1.12	1.13
U substitutional Si	28.52	2.00	0.66	0.66
Si substitutional U1	**-27.45**	**-0.93**	0.40	0.40
Si substitutional U2	**-26.19**	0.33	1.67	1.67
Si interstitial site 2b	**-16.95**	**-1.04**	**-0.24**	**-0.23**
Si interstitiasite Si-Si	**-15.09**	0.83	1.63	1.63
C interstitial site 2b	15.42	**-0.49**	0.56	**-0.49**
C interstitial site Si-Si	16.48	0.57	1.62	0.57
Type of point SiC	U_3Si_2-SiC-$U_{20}Si_{16}C_3$	U_3Si_2-SiC-$U_3Si_2C_2$	SiC-$U_{20}Si_{16}C_3$-UC*	SiC-$U_3Si_2C_2$-UC*
Si vacancy	23.97	8.06	7.78	7.87
C vacancy	**-11.89**	4.02	4.29	4.21
U substitutional Si	32.20	5.68	5.49	5.49
U substitutional C	5.61	10.91	11.27	11.10
Si substitutional C	**-28.56**	3.26	3.81	3.64
C substitutional Si	35.91	4.09	3.54	3.72
U Interstitial_2	24.03	13.41	13.50	13.42

* Fuel and cladding not in contact.

On the fuel side, when the intermediate phase is U_3Si_5, as observed in diffusion couples, forming the equilibrium phase assemblage U_3Si_2-U_3Si_5-$U_{20}Si_{16}C_3$, all defects have positive or close to zero formation energies, removing the thermodynamic driving force for interactions and thus, explaining the lack of elemental transport toward the SiC cladding. On the cladding side, when U_3Si_2 is replaced by UC generating the equilibrium phase assemblage SiC-UC-$U_{20}Si_{16}C_3$, defect formation energies also become positive, restricting the thermodynamic driving force for interactions.

6. U_3Si_2-Fission Product Behavior

In order to assess and further develop U_3Si_2 as a fuel, the impact of the fission process on the fuel must be fully investigated. As part of that effort, our group has experimentally and computationally explored the 40-66 at% Si region of the U-Si binary system in order to better understand the impact of U-Si compositional changes. Through this work, a previously projected homogeneity region of U_3Si_2 [92] was expanded and the phase diagram was refined [93, 94] to reflect new investigations into identified Si-rich phases [16].

While advances made in understanding U-Si phase equilibria allow for improved prediction of the formation and nature of system phases, there remains the need to address interactions between the fuel and fission products (FPs). These must also be investigated to better understand the chemical environment of the fuel as this will impact the thermophysical properties and in turn, fuel performance. FP elements may have limited solubility in the fuel and, as burnup progresses, the concentration may exceed that modest solubility limit and lead to the formation of secondary phases. Thus, there is a possibility of both solute FPs and the formation of additional phases influencing the fuel properties.

Literature that reports investigations of FP interactions in U_3Si_2 fuel is limited. Currently, the only published work in which FP-doped fuel is examined experimentally is that of Ugajin and Itoh [95]. They explored the impact of FPs in fuel at exaggerated burnup (80 and 97%) compositions by arc-melting U_3Si_2 doped with 11 surrogate metals. Phases were characterized by electron probe microanalysis and x-ray diffraction (XRD). The noble metals Mo, Rh, and Ru were determined to form individual quaternary phases with U and Si; rare earth elements (Ce, La, Nd, Pr, Y) formed monosilicide precipitates; and the solid solution phase (RE,Pd)Si formed where RE represents a rare earth element [95]. Strontium did not appear to interact with the fuel before evaporating from the sample and Zr was observed to form an unidentified U-Zr-Si compound [95]. Zirconium was determined to be soluble up to 9.5 at% in the U_3Si_2 [95]. Work conducted by Turner, et. al. investigating the use of Gd as a burnable poison in U_3Si_2 suggests Gd may be soluble up to 4-5 at% in the fuel [96].

Defect formation in U_3Si_2 fuel following the incorporation of select surrogate FPs was computationally considered by Nanopoulos [97] using density functional theory (DFT). It was used to examine the incorporation of Ce, Mo, Pr, Ru, Xe, and Zr into the U_3Si_2 structure, any associated swelling of the fuel as a result, and the formation of any FP-silicide phases. Overall, FPs were energetically favored to dissolve in U_3Si_2 through substitution on the U1 site. The Mo was predicted to be insoluble in the U_3Si_2 matrix and it can be expected to form Mo-Si or U-Mo-Si phase precipitates. Elements Ce and Zr were found to be soluble in U_3Si_2 with the potential for secondary phase formation, and Ce_5Si_3 was calculated to co-exist with a Ce-saturated U_3Si_2 matrix. While computational work broadly supports the formation of individual silicide phases due to the generally observed modest solubility of FPs in U_3Si_2, there are disagreements with experimental observations. In the cases of Ce and Mo, FP-disilicide ($FPSi_2$) is computed to have the most negative formation energy [97] in comparison to CeSi or $U_4Mo(Mo_xSi_{1-x})Si_2$, which are experimentally observed phases [95]. Nanopoulos' computational work was performed assuming only a single point defect in their 72-atom supercell at 0 K [97], which may limit its applicability. The sole experimental effort considered high FP content simulated burnups of >80% with multiple FPs, and thus comparisons between the two evaluations is questionable.

In order to further assess U_3Si_2 fuel behavior, a combined experimental and computational approach was adopted to examine the impact of representative FPs in the fuel. To do this in a systematic fashion, calculated fuel compositions after significant burnup were used to identify higher content FPs which were then grouped with those expected to act similarly in order to reduce the number of FP elements to be considered. Four prominent FP elements (Ce, Mo, Y, Zr) were chosen for examination and were used as dopants in U_3Si_2 samples. The results were used to guide the creation of an FP-silicide thermodynamic database. The database contained 8 FPs (Ba, Ce, Gd, Mo, Pu, Se, Y, Zr) and all known phases in those systems were considered along with any related U alloys and those silicides with the potential to form in the fuel environment. Experimental observations of relative stability were used to estimate the thermodynamic behavior of phases for which values are not available. Predictions for the phase state of

irradiated fuel at a high burnup of 52.5 MWd/kgU and in a possible high burnup region of 116.6 MWd/kgU were used to evaluate irradiated U_3Si_2 fuel behavior. Density functional theory calculations were also used to consider the individual impacts of Ba, Ce, Gd, Y, and Pu on U_3Si_2. Results from DFT were compared with experimental observations and were contrasted with the thermodynamic equilibrium predictions from the generated database.

6.1. Methodology

6.1.1. Experimental

6.1.1.1. Fabrication of Doped U_3Si_2 Ingots

The surrogate radionuclide FPs Ce, Mo, Y, Zr were chosen to represent a variety of abundant FP elements. Undoped ingots of U_3Si_2 were prepared using depleted uranium rods (99.9+%, Aerojet Rocketdyne) and silicon pieces (99.999%, Cerac Inc.). Uranium and silicon pieces were initially mixed in a ratio of 60 at% U and 40 at% Si for ~3 g samples with an additional 5 mg Si added to the mixture to compensate for expected Si loss to volatilization during melting. This mixture was then arc melted under gettered argon (O_2 $<10^{-10}$ ppm) with a tri-arc furnace equipped with 2% thoriated tungsten electrodes (5 TA Reed Tri Arc, Centorr Vacuum Industries). The ingots were flipped and re-melted an additional four times in order to ensure a homogenous composition. Samples were doped with individual FP elements by adding 5 wt% of either Ce, Mo, Y, or Zr to a prepared U_3Si_2 ingot and arc melted an additional five times, again turning the sample between each to aid in homogenization. Due to the difficulty associated with arc-melting powders, Ce pieces (99.95%, Sigma-Aldrich, Inc.), Mo foil (≥99.9%, Sigma-Aldrich, Inc.), Y pieces (99.9%, Alfa Aesar), and Zr wire (99.2% excluding Hf, ≤6.5% Hf, Alfa Aesar) were used for doping purposes. The samples were annealed to promote equilibrium and for further sample homogenization at 1250°C for 48 hours in a tube furnace (1730-12HT, CM Furnaces Inc.) under argon (UHP, Praxair Inc.) purified with an oxygen pump (Gen'Air, SETNAG). Oxygen content was further reduced by a Ta getter in the furnace, reaching an oxygen concentration of less than 10^{-15} ppm measured at the outlet of the furnace.

6.1.1.2. Characterization of FP-Doped U_3Si_2

Once annealed, the ingots were broken and portions were set aside for characterization by XRD and scanning electron microscopy (SEM). Powder XRD was conducted on portions of the ingots with a Rigaku Ultima IV instrument using Cu-Kα radiation to scan 20-100° 2θ at 0.02°/s. Rietveld refinement of powder x-ray diffraction patterns was completed using MAUD software [98] with Crystallographic Information Files (CIF) sourced from The Materials Project [99]. As a CIF was not publicly available for U_4MoSi_3, crystallographic structure information available in literature [100] was used to generate one using Visualization for Electronic and Structural Analysis (VESTA) software [101]. Fig. 6.1 shows the generated unit cell model for U_4MoSi_3.

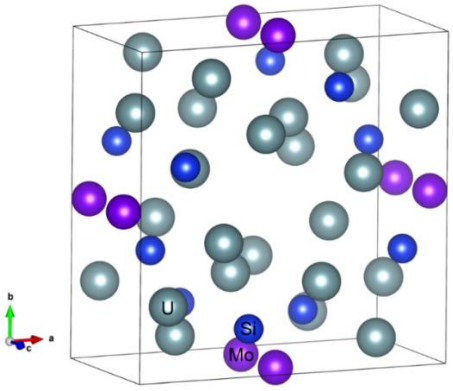

Fig. 6.1. Generated unit cell structure of U_4MoSi_3.

For SEM characterization, a portion of the ingots were mounted in epoxy resin and mechanically ground with wet silicon carbide paper (600 and 1200 grit) and polished with sequential diamond suspensions (9, 3, and 1 µm). Imaging and compositional analysis used back-scatter electron (BSE) microscopy with energy dispersive spectroscopy (EDS) in a TESCAN Vega-3 SBU variable pressure microscope. Multiple points on each sample were imaged and characterized with EDS to confirm that the samples had reached equilibrium.

6.1.1.3. Characterization of Multiple Fission Product Interactions

A diffusion couple was created such that a polished surface of an U_3Si_2 ingot was held in contact that of an arc-melted 1:1 Mo:Zr alloy to study potential FP partitioning. The diffusion couple was designed to identify transport and solubility trends in the presence of two significant FPs. The mating surfaces were ground and polished using the same method noted above for the preparation of SEM samples. This configuration was held in place with a jig consisting of molybdenum plates wrapped in tantalum foil held together by two molybdenum screws, as depicted in Fig. 6.2. The jig was wrapped in additional tantalum foil to further prevent sample oxidation during heating. The couple was heat treated to 1200°C for 24 hours in the tube furnace under gettered argon ($O_2 < 10^{-15}$ ppm). The ingot and alloy easily separated upon removal from the jig and each piece was then mounted in epoxy resin. A cross-section was cut using a low speed circular saw equipped with a sintered diamond blade (SYJ-150, MTI Corporation, Richmond, CA) and the cross-section surface was ground, polished, and characterized as described above.

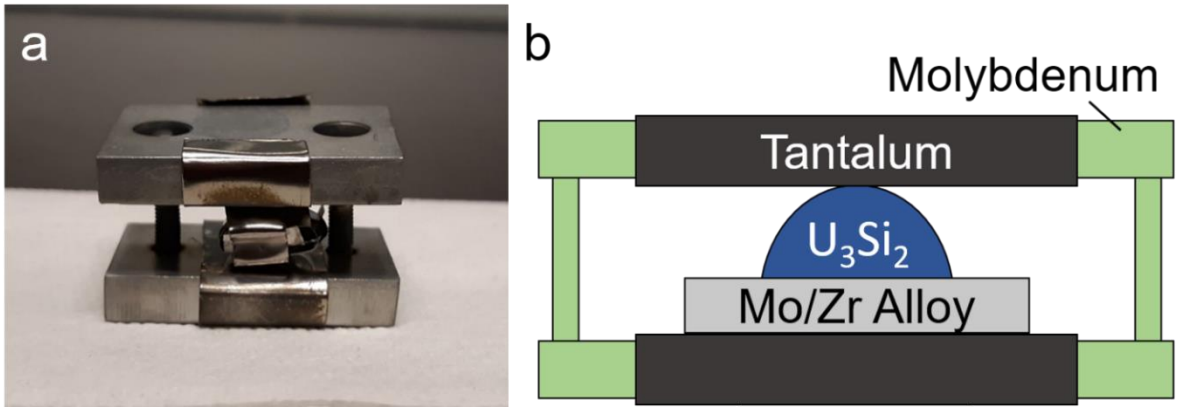

Fig. 6.2. (a) Photo of the assembled diffusion couple prior to heat treatment and (b) a schematic depicting the configuration.

6.2. Modeling

6.2.1. Thermodynamic Calculations

The FactSage™ [102] set of thermodynamic equilibrium codes was used to compute secondary phase development in U_3Si_2 during irradiation through calculating system equilibria (Gibbs energy minimization). Temperature-dependent thermodynamic values for elements and compounds were provided by the Scientific Group Thermodata Europe (SGTE) [64] database and the Thermodynamics of Advanced Fuels – International Database (TAF-ID) [103]. A set of models for solid solution behavior was also obtained from TAF-ID. In addition, thermodynamic values for Ce-Si were taken from Shukla, et al. [104]

The melt solutions for the Ce-Si [105] and Y-Si [106] systems were optimized using a one-sublattice Redlich-Kister Muggianu model [102] model in which, the excess Gibbs energy (g^E) from the mixing of species A and B is represented using the polynomial

$$g^E = \sum {}^{i}L_{AB} X_A X_B (X_A - X_B)^i,$$

wherein the interaction parameter, L_{AB}, is fit to the phase diagram [102]. X_i represents the molar site fraction of each species. Based on experimental observations and the temperature range of interest for reactor performance, emphasis was placed on matching the 400-1700°C, 30-70 mol% Si portion of the diagrams for each system. Final interaction parameters for the Ce-Si and Y-Si systems are listed in Table 6.1. Figs. 6.3 and 6.4 show the Ce-Si and Y-Si phase diagrams, respectively, with the published diagram overlaid for comparison.

Table 6.1. Interaction parameters fit to phase diagram data using the RKMP model

Binary	Redlich-Kister Interaction Parameter
Ce-Si	${}^{0}L_{CeSi}$ = -212300
	${}^{1}L_{CeSi}$ = -14000 + 30T
	${}^{2}L_{CeSi}$ = 37330 - 10T
Y-Si	${}^{0}L_{SiY}$ = -286000 + 58T
	${}^{1}L_{SiY}$ = -600 + 10T

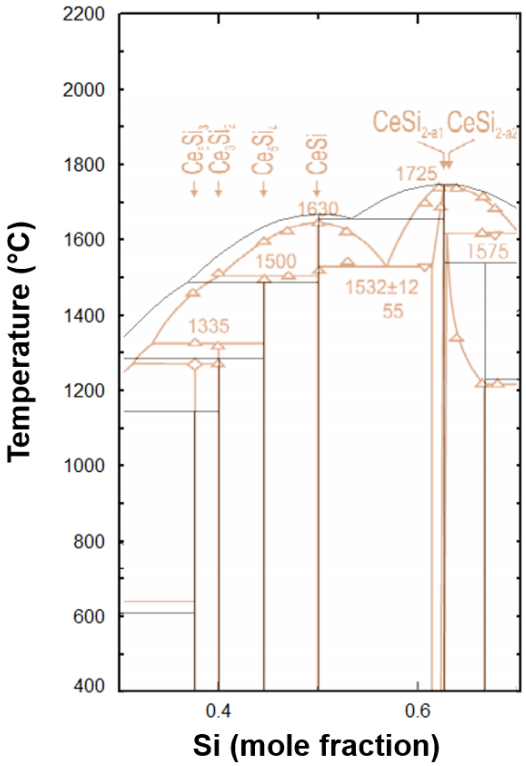

Fig. 6.3. Estimated Ce-Si phase diagram for the region of interest and the diagram of derived from phase change measurements of Bulanova, et al. [105] in orange.

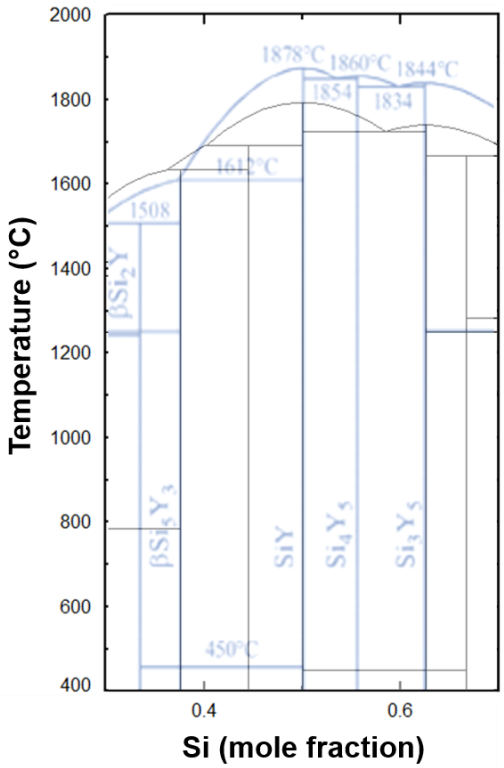

Fig. 6.4. Estimated Y-Si phase diagram for region of interest and the diagram of derived from phase change measurements of Okamoto [106] in blue.

The liquid melt solution also contained Ba, Gd, Mo, Pu, Si, U, and Zr. Interaction parameters for U-(Ba,Gd,Mo,Pu,Zr), Si-(Mo,Pu,Zr), Zr-(Ba,Ce,Mo,Pu,), Mo-(Ba,Ce), and Mo-Pu-U were sourced from TAF-ID [103]. The melt phase of the Gd-Si binary was modeled previously [107] and was included in our liquid solution.

While the U_4MoSi_3 was considered in this effort, the phase has yet to be appropriately characterized thus, thermodynamic values for Mo_5Si_3 [103] as both phases share the same crystal structure protype, W_5Si_3 [100]. The original values were adjusted in order to encourage U_4MoSi_3 formation over Mo_5Si_3 at equilibrium at 1250°C to match experimental results. Final thermodynamic values used in the FPDB are listed in Table 42.

Table 6.2. Determined thermodynamic values for U_4MoSi_3 for equilibrium calculations

Phase	$\Delta_f H^0$ (kJ/mol)	S^0 (J/mol^{-1}K^{-1})	$C_p=a+bT+cT^2+dT^{-2}$				
			a	*b*	*c*	*d*	Temperature (°C)
U_4MoSi_3	-414.34	325.52	208.62	-0.0052	1.90E-05	-2.79E+06	298-6000

In our work on the U-Si system reported elsewhere [94], U_3Si_2 was modeled having a homogeneity range, U_3Si_{2+x}, using the three-sublattice compound energy formalism (CEF) [108]. This solution model was augmented to include Pu, Ce, Gd, and Zr and the phase is represented by the Eq. $(A,B,C,D,E)_k(F)_l(F,Va)_m$ where *k*, *l*, and *m* represent the stoichiometric coefficients and Va represents vacancies in the structure [108]. The metals U, Pu, Ce, Gd, and Zr were considered as residing on the first sublattice wherein *k* is equal to 3 and Si occupies both the second and third sublattice, vacancies on the third sublattice, and the coefficients *l* and *m* equal to 2 and 1, respectively. Excess silicon was thus provided for with the third sublattice that was otherwise occupied with vacancies. The Gibbs energy of each

endmember (e.g., $U_3Si_2Va_1$, $Pu_3Si_2Va_1$, etc.) were used to generate the overall Gibbs energy of the phase. Hyper-stoichiometric compositions (x>0) contained non-zero Si occupancy on the third sublattice, with the Gibbs energy calculated by adding the energy associated with diamond structure Si to that of the relevant 3:2 stoichiometric phase. In the absence of a Gd_3Si_2 structure [96, 107], one was modeled from the thermodynamic values of Gd_5Si_3 is it falls closest in composition to a theoretical Gd_3Si_2. The following Eq. was used to represent the Gibbs free energy associated with the endmember

$$\Delta G_{Gd_3Si_2} = \Delta G^{\circ}_{Gd_5Si_3} - 2\Delta G^{\circ}_{Gd} - \Delta G^{\circ}_{Si}.$$

The solubility of the Pu, Ce, Gd, and Zr hyper stoichiometric phases was limited to 10^{-12} at% to prevent formation. A solubility limit of about 0.013 at% was applied the Ce and Zr end members to prevent overrepresentation of these two fission products in the model. The solubility limit of the Gd end member was set at 0.015 at% based on previous experimental evidence [96]. The complete contents of the solution database included in FPDB are listed in Table 6.3.

Table 6.3. Contents of FPDB solution database.

Solution	Model	Formula	Interactions	Ref.
Liquid	One-lattice RKMP	(Ba,Ce,Gd,Mo,Pu,Si,U,Zr,Y)	U-(Si,Ba,Gd,Mo,Pu,Zr), Si-(Ce,Gd,Mo,Pu,Zr,Y), Mo-(Ba,Ce,Pu,Zr), Zr-(Ba,Ce,Pu), Mo-Pu-U	[94, 103, 107]
α-U	One-lattice RKMP	(U,Mo,Si,Pu,Zr)	U-(Mo,Pu,Zr,Si)	[94, 103]
β-U	One-lattice RKMP	(U,Mo,Pu,Si,Zr)	U-(Mo,Pu,Si,Zr), Pu-(Mo,Zr)	[94, 103]
γ-U	One-lattice RKMP	(U,Ba,Ce,Gd,Mo,Pu,Si,Zr)	U-(Ba,Gd,Mo,Pu,Zr), Si-(Gd,Mo,Pu,Zr), Mo-(Ba,Ce,Pu,Zr), Ba-(Pu,Zr), Ce-Zr, Mo-Pu-U	[94, 103, 107]
USi	Two-sublattice CEF	$(U,Pu)_{3.4}Si_{3.45}$	-	[103]
U_3Si_{2+x}	Three-sublattice CEF	$(U,Pu,Ce,Gd,Zr)_3Si(Si,Va)$	U-Si-(SiVa)	[94]
U_3Si_{5+x}	Three-sublattice CEF	$U_3Si_5(Si,Va)$	U-Si-(SiVa)	[94]
Si (diamond)	One-lattice RKMP	(Si,U)	U-Si	[94]
δ-Pu	One-lattice RKMP	(Pu,Ba,Ce,Gd,Mo,Si,U,Zr)	Pu-(Ba,Mo,Si,U,Zr), Mo-(Ba,Ce), Zr-(Ba,Ce,U,Zr), U-(Ba,Gd)	[103]
α-Ce	One-lattice RKMP	(Ce,Pu)	-	[103]
η	One-lattice RKMP	(Pu,U)	Pu-U	[103]
ε	One-lattice RKMP	(Pu,U)	Pu-U	[103]
$USi_{1.88}$	Two-sublattice CEF	$(U,Pu)_{1.88}Si$	-	[103]
β-Pu	One-lattice RKMP	(Pu,U)	Pu-U	[103]
$MoSi_2$	Two-sublattice CEF	$(Si,U)_2(Mo,Zr)$	-	[103]
Mo_3Si	Two-sublattice CEF	$(Mo,Si)_3Si$	-	[103]
Hexagonal Laves	Two-sublattice CEF	$(Mo,Zr)_2(Mo,Pu,U,Zr)$	MoZr-(Mo,Pu,U,Zr), Mo-MoZr, Zr-MoZr	[103]
Cubic Laves	Two-sublattice CEF	$(Mo,Zr)_2(Ce,Mo,Pu,U,Zr)$	MoZr-(Ce,Mo,Pu,U,Zr), Mo-MoZr, Zr-MoZr	[103]
Pu_3Si_5	Two-sublattice CEF	Pu_3Si_5	-	[103]
Zr_5Si_3	Three-sublattice CEF	$(Mo,Si,Zr)_2Si_3(Mo,Zr)_3$	-	[103]

Pu_5Si_3	Three-sublattice CEF	$(Mo,Pu)_4(Mo,Pu,Si)Si_3$	Mo-MoSi-Si	[103]
α-Zr	One-lattice RKMP	(Zr,Ba,Ce,Gd,Mo,Pu,Si,U,Zr)	Zr-(Ba,Ce,Mo,Pu,Si,U), Mo-(Ba,Ce,Pu), U-(Ba,Gd,Pu), Gd-Si	[103, 107]
θ-Pu_6Zr	Two-sublattice CEF	$(Pu,Zr)_6(Pu,Zr)$	PuZr-(Pu,Zr), Pu-PuZr, Zr-PuZr	[103]
δ-UZr_2	Two-sublattice CEF	$(U,Zr)_2(U,Zr)$	Zr-UZr	[103]

6.2.2. First Principles Calculations

DFT calculations were performed with the Vienna Ab initio Simulation Package (VASP) [109]. The Perdew-Burke-Ernzerhof (PBE) formalism [110] was used to model the electron exchange correlation. The DFT+*U* method [111] with an effective *U* (U_{eff}) of 1.5 eV was used to correct for the strong correlation of U and Pu's 5*f* electrons. The U_{eff} of 1.5 eV for U was taken from the previous study of Noordhoek, et. al. [21], while *U*-ramping calculations [112] were performed to obtain a U_{eff} for Pu_3Si_2 (see Section A3 in Appendix) [113]. The U_3Si_2 unit cell was fully relaxed with a 500 eV cut-off energy for the plane wave basis set, a total energy convergence criterion of 10^{-4}eV, and a force convergence criterion of 0.01 eV/Å. A 120 atom 2x2x3 supercell with a γ-centered Monkhorst-pack k-point spacing of <0.02 $Å^{-1}$ was constructed for U_3Si_2 and the introduction of a single point defect was used to represent the inclusion of an FP at a dilute concentration.

To determine what U_{eff} to use for the Pu in the Pu_3Si_2, we performed *U*-ramping calculations, using U_{eff} from 0 to 4 eV, with a step of 0.1 eV. We used 600 eV plane wave cutoff, 10^{-6} eV and 10^{-2} eV/Å energy and forces convergence criteria, respectively, and 9×9×9 *k*-point mesh. The structures were fully relaxed with no symmetry constrain. We first relaxed the Pu_3Si_2 structure using U_{eff}=0 eV, and for all subsequent relaxations, the relaxed structure, wavefunction and charge density from the previous relaxation at lower U_{eff} were used. The Pu_3Si_2 lattice parameters relative error with respect to experiments [113], calculated using *U*-ramping [112] are shown in Fig. 6.5. There are two U_{eff} worth pointing out, 0 eV and 1.5 eV. For U_{eff}=0 eV the cumulative lever of error for both lattice parameters is at its lowest. On the other hand, for U_{eff}=1.5 eV, the *a*=*b* lattice parameters have low error, while the error for the c lattice parameter is large, it appears to converge beginning at U_{eff}=1.5 eV. Considering this and the fact that U_{eff}=1.5 eV was used for the U atoms, U_{eff}=1.5 eV was used again for the Pu atoms. Note that the structures at each U_{eff} relaxed to a 127 space group, the same as the experimental space group of Pu_3Si_2.

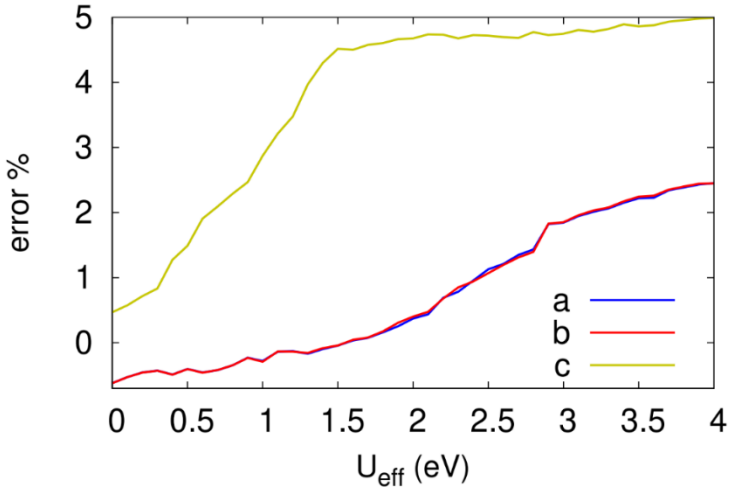

Fig. 6.5. Lattice parameters relative error with respect to the experimental lattice parameters of Pu_3Si_2 [113] as a function of the U_{eff}, calculated using U-ramping method.

To examine the solubility of FPs and Pu in U_3Si_2, the energy associated with a reaction of U_3Si_2 with an FP-silicide to form a ternary phase. In order to balance the reaction, an additional phase such as U or a U-silicide must be included, as demonstrated in the reaction:

$$c_1 U_3 Si_2 + c_2 FPSi + c_3 BP \leftrightarrow U_{71} Si_{48} FP. \quad 6.1$$

where BP is an additional balancing phase and $U_{71}Si_{48}FP$ product is an inclusive 120 atom supercell. For example, consideration of BaSi requires the reactant U_3Si as well

$$\frac{70}{3} U_3 Si_2 + BaSi + \frac{1}{3} BP \leftrightarrow U_{71} Si_{48} FP. \quad 6.2$$

The solvation energy, ΔE_{sol}, required for the above reaction was calculated from

$$\Delta E_{sol} = E(U_{71} Si_{48} FP) - \sum c_i E_r, \quad 6.3$$

where $E(U_{71}Si_{48}FP)$ is the total energy of the U_3Si_2 supercell with a solubilized FP and E_r is the energy of each reactant phase and c_i are the coefficients for the balanced reaction.

6.3. Results

Experimental efforts to assess potential U_3Si_2 interactions with individual representative FPs were performed by mixing constituents and determining solubilities and phase formation by electron microscopy and XRD characterization. Interactions of U_3Si_2 with a Mo/Zr alloy were similarly investigated via a diffusion couple to understand partitioning in the system. Modeling efforts to reflect the observed effects and provide an understanding of system behavior utilized thermochemical modeling together with DFT studies.

6.3.1. Interactions between U_3Si_2 and Individual Fission Products

Rietveld refinement of XRD patterns for all four FP-doped samples were performed in order to determine accurate lattice parameters for the U_3Si_2 phase and identify secondary phase formation and structure. Powder XRD of the 5 wt% Ce-doped U_3Si_2 indicated the presence of tetragonal $P4_12_12$ Ce_5Si_4 (Fig. 6.6a) which was confirmed through SEM imaging and EDS as shown in Fig. 6.6b, with no additional phases detected. Ce was seen to have a solubility limit of 3.6±0.9 at% based on the EDS analysis.

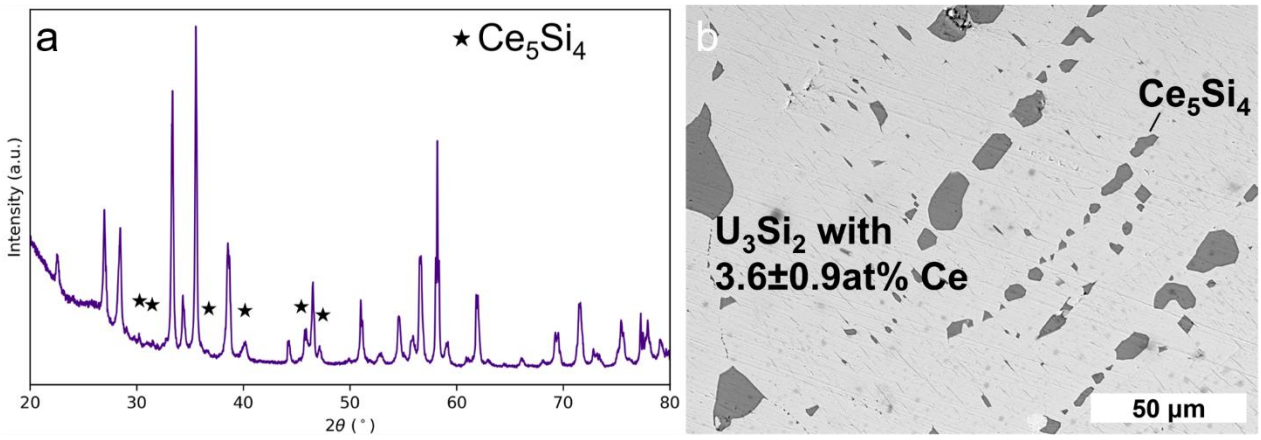

Fig. 6.6. (a) XRD pattern with the identified tetragonal Ce_5Si_4 secondary phase in the 5 wt% (22 at%) Ce-doped sample. (b) A representative BSE image with the solubility of Ce in the bulk indicated. Unlabeled peaks on the diffraction pattern correspond to U_3Si_2 peak positions.

The U_3Si_2 sample doped with 5 wt% Mo formed the ternary U_4MoSi_3 phase and γ-(Mo,U) as shown in Fig. 6.7, with the phase appearing to evolve from the visible fine eutectic structure. EDS measurements were unable to obtain any significant indications of solubility of Mo in U_3Si_2.

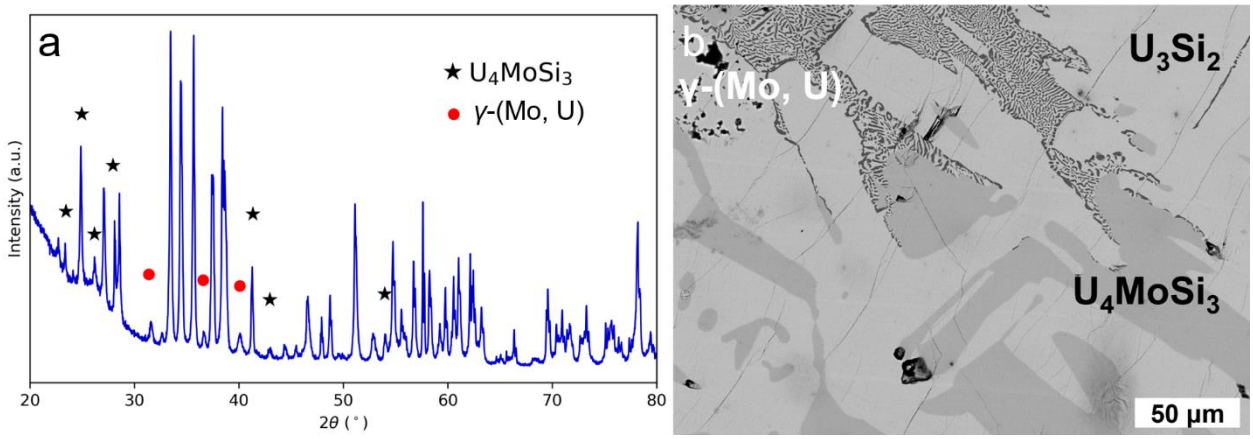

Fig. 6.7. (a) XRD pattern with the identified triclinic U_4MoSi_3 and the bcc γ-(U,Mo) from the secondary phase regions in the 5 wt% (30 at%) Mo-doped fuel sample. (b) A representative BSE image with identified phase regions. Unlabeled peaks on the diffraction pattern correspond with U3Si2 peak positions.

The Y-doped U_3Si_2 samples contained four phases consisting of orthorhombic Y_5Si_4 (Pnma structure), γ-U, tetragonal U_3Si, and U_3Si_2 as indicated in Fig. 6.8. EDS did not indicate statistically significant levels of Y dissolved in the U_3Si_2. The presence of the two additional U-rich phases (γ-U and U_3Si) formed as a result of Y-doping of the fuel suggest equilibrium was not achieved. Possible consequences of this are detailed in the discussion section.

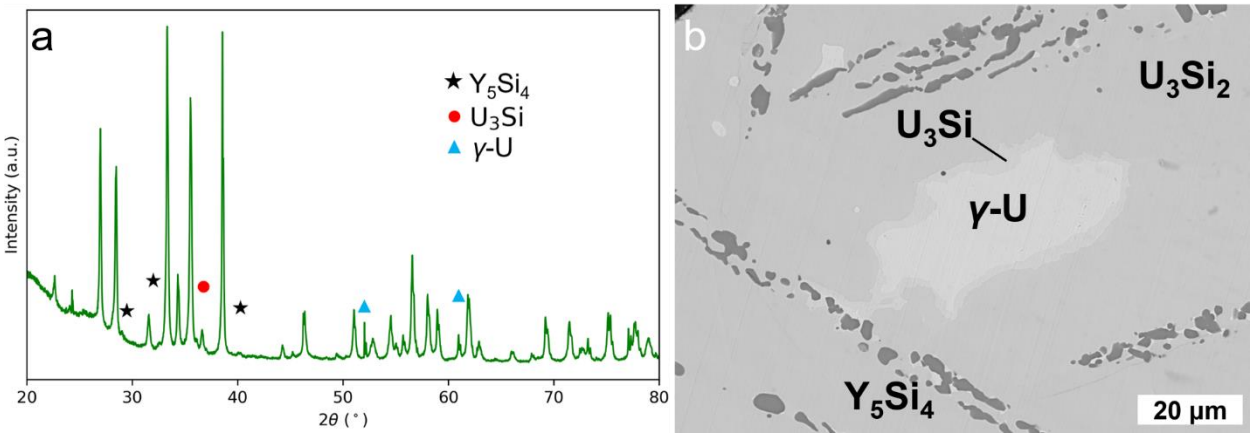

Fig. 6.8. (a) XRD pattern with the identified orthorhombic Y_5Si_4, bcc γ-U and the tetragonal U_3Si structures of the secondary phase regions in the 5 wt% (32 at%) Y-doped fuel sample. (b) A representative BSE image. Unlabeled peaks on the diffraction pattern correspond to U_3Si_2 peak positions.

Zr was found to be soluble in U_3Si_2 up to 3.6±0.4 at%, at which point Zr_5Si_4 and α-U precipitate from the fuel as seen in Fig. 6.9. Zirconium has been reported to have a solubility of up to 9.5 at% in the bulk [95], however, this high of a value could not be replicated in our work. The γ-U phase regions formed in direct proximity to Zr_5Si_4.

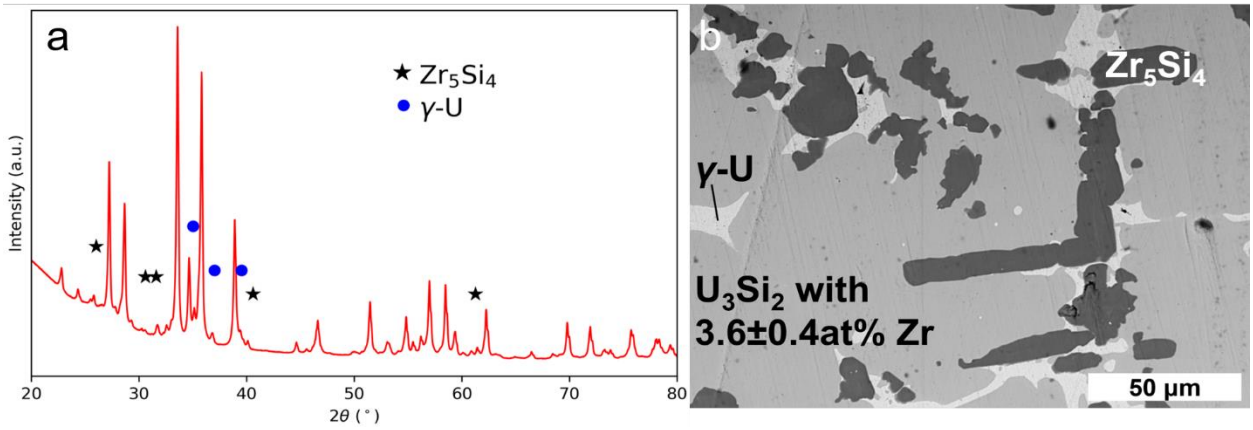

Fig. 6.9. (a) XRD pattern with the identified tetragonal Zr_5Si_4 and the bcc γ-U secondary phase regions in the 5 wt% (31 at%) Zr-doped fuel sample. Unlabeled peaks on the diffraction pattern correspond with U_3Si_2 peak positions. (b) A representative BSE image with the solubility of Zr in the bulk indicated.

Lattice parameters determined from the XRD patterns were used to identify any composition changes in the FP-doped U_3Si_2 samples. The overall changes observed in unit cell volumes resulting from FP-doping were calculated and are shown on a concentration basis by dividing the volume change by the dopant concentration (22, 30, and 31 at% for Ce, Mo, and Zr, respectively) and are summarized in Table 6.4. Inclusion of Mo or Zr in the fuel resulted in lattice contraction, with Zr having the more dramatic effect. Ce and Y doping resulted in apparent volume expansion, although the values for the Y-doped samples are likely in error as the unit cell volume change from the dissolution of Y of could not be accurately determined due to overlap of XRD peaks with those of both U_3Si and γ-U. The Ce and Zr FPs had similar levels of

solubility in the bulk with similar, but opposite volume changes. The effect of Mo on unit cell volume fell within error of nullity, confirming its lack of solubility in U_3Si_2.

Table 6.4. U_3Si_2 unit cell volume change due to FP-doping.

Fission Product	(ΔV/V)/FPat% (%)
Ce	0.018±0.001
Mo	-0.003±0.002
Zr	-0.015±0.002

6.3.2. Mo/Zr Interactions with U_3Si_2

The produced 1:1 Mo:Zr alloy used to investigate Mo/Zr interactions with U_3Si_2 contained two-phases: A bcc Zr-rich alloy phase ($Zr_{0.87}Mo_{0.3}$) and a fcc Mo-rich intermetallic phase ($MoZr_2$) as determined by XRD and SEM-EDS (Fig. 6.10), with the overall composition confirmed by EDS to be 50 at% Mo and Zr.

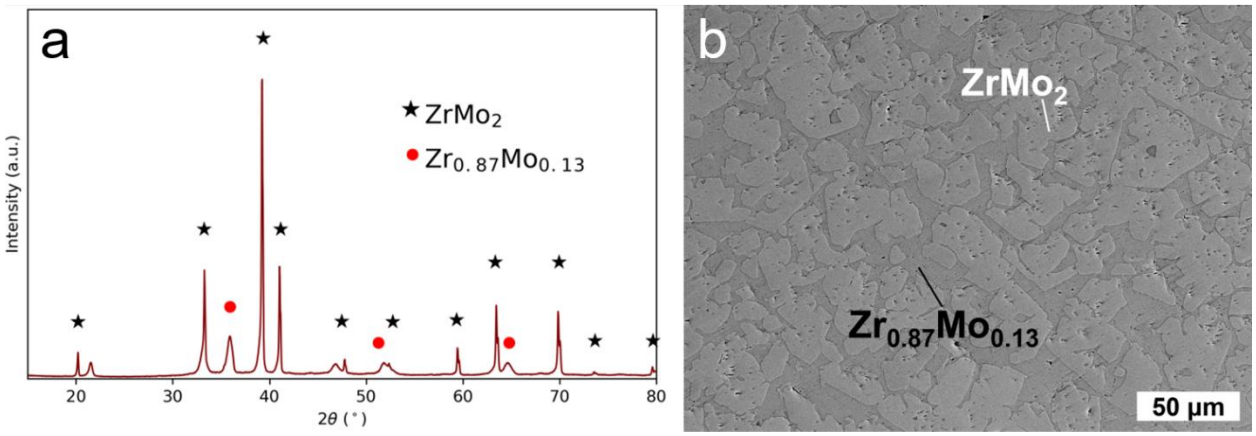

Fig. 6.10. (a) XRD pattern and (b) SEM image indicating EDS-confirmed chemical composition of the Mo/Zr alloy.

Examination of the U_3Si_2 face of the diffusion couple revealed a 16.6±0.7 µm wide band of U_4MoSi_3 as seen in Fig. 6.11. Zirconium was found dissolved in the U_4MoSi_3 intermetallic phase at a concentration of 0.6±0.2 at%. The concentration of Mo and Zr in the bulk U_3Si_2 was statistically insignificant and no additional U-Si phases were detected in the sample.

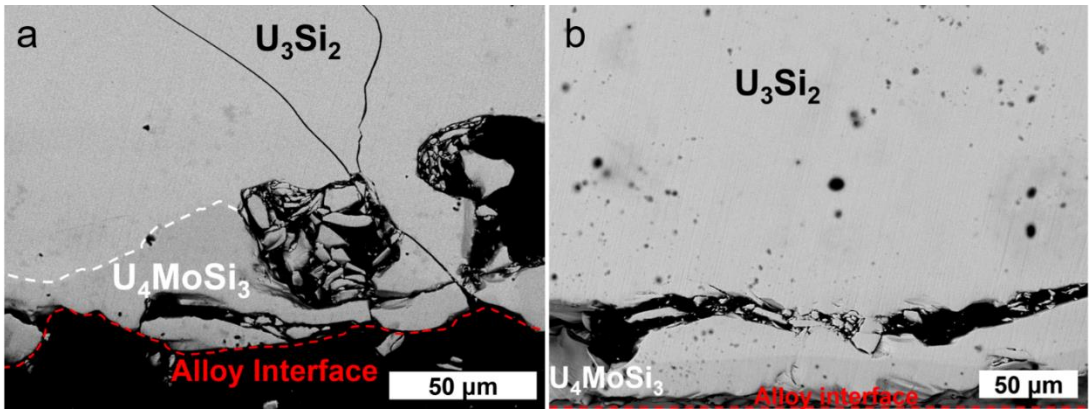

Fig. 6.11. (a) BSE image of the cross-section of the U_3Si_2 side of the diffusion couple following heating with (b) a second region of the sample. The white dotted line indicates the extent of U_4MoSi_3 ternary formation in the fuel and the red dotted line represents the location of the interface with the alloy.

On the Mo:Zr alloy side of the diffusion couple, analysis indicated a concentration of ≤18±4 at% U to a depth of 133±11 µm into the alloy (Fig. 6.12). A border of acicular Zr_2Si was observed behind the U-diffusion front. ZrMoSi containing precipitated U metal (Fig. 6.12b) formed a 13±3 µm thick region on the surface of the alloy at the interface with the U_3Si_2. No Si was detected in the Mo:Zr alloy.

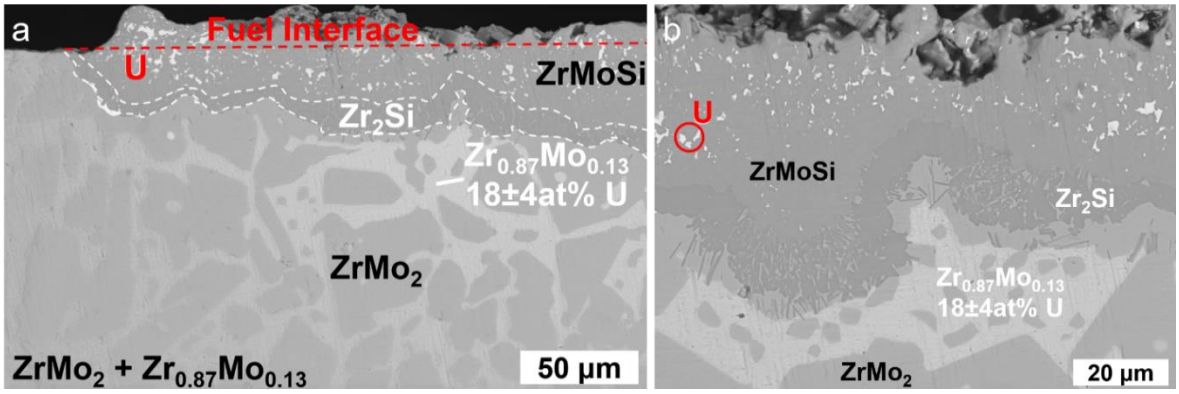

Fig. 6.12. (a) BSE image of the cross-section of the Mo/Zr alloy following heating of the diffusion couple with (b) an acicular Zr_2Si-containing region shown at higher magnification. White inclusions in the near-surface region are precipitated U-metal, an example of which is circled.

6.3.3. Modeling

Computed phase formation and solubility of FPs in U_3Si_2 served to help understand the observed secondary phase generation and solubility limits. Thermodynamic modeling provided generally expected phase assemblages and compositions for the stoichiometric and solution phases. First principles calculations provided comparative formation energies and identified probable solute crystal lattice sites.

6.3.3.1. Thermodynamic Modeling

Experimental results were used in the development of an FP-silicide thermodynamic database for use in describing burnup behavior including silicon partitioning. The database includes 64 compounds and 95 phases with 26 modeled solution phases. A summary of the systems included in the database is seen in Table 6.5. The USi-based phase was modeled using the two-sublattice CEF of the TAF-ID provided representation of $(U,Pu)_{3.4}Si_{3.45}$ [103]. A three-sublattice CEF model was used for $(U,Pu,Ce,Gd,Zr)_3Si_{2+x}$

and $(U,Pu,Ce,Gd,Zr)_3Si_2(Si,Va)$ [94] based on the current work and reported observations. U_3Si_{5+x} was similarly modeled using a $U_3Si_5(Si,Va)$ model, Va represents vacancies on the sublattice [94].

Table 6.5. Phases included in FP-silicide database

System	Silicide Phases	Ref.
U-Si*	USi_3, $USi_{1.88}$, USi, U_3Si, U_3Si_{2+x}, U_3Si_{5+x}	[94, 103]
Ba-Si	BaSi, $BaSi_2$	[64]
Ce-Si	CeSi, $CeSi_2$, Ce_3Si_2, Ce_5Si_3, Ce_5Si_4	[64, 104]
Gd-Si	$GdSi_2$, Gd_3Si_5, GdSi, Gd_5Si_4, Gd_5Si_3	[64, 107]
U-Mo-Si	$MoSi_2$, Mo_5Si_3, Mo_3Si, MoU_2, U_4MoSi_3*	[103]
U-Zr-Si	ZrSi, $ZrSi_2$, Zr_2Si, Zr_3Si, Zr_3Si_5, Zr_3Si_2, Zr_5Si_4, Zr_5Si_3, U_2Zr	[103]
Y-Si	YSi_2, Y_3Si_5, YSi, Y_5Si_4, Y_5Si_3	[64]
Se-Si	SeSi	[64]
Pu-Si	Pu_3Si_5, $PuSi_{1.88}$, PuSi, Pu_3Si_2,	[103]

*Compound thermodynamic values were optimized using analogous structure phases

Depletion calculations using the Serpent fuel code [114], provided fuel compositions at specific burnups for a prototypic LWR. Using these compositions, equilibrium calculations were conducted at two burnup levels: A high average burnup of 52.5 MWd/kgU and that of a possible high burnup region of 116.6 MWd/kgU at a uniform fuel temperature of 500°C [115]. The compositions are listed in Table 6.6 with the resulting equilibrium phase assemblages given in Table 6.7.

Table 6.6. Example fuel composition from Serpent [114] depletion calculations for burnups of 52.5 and 116.6 MWd/kgU. Grouped elements appear on the same line, with the first element representing the group in calculations.

Element(s)	**52.5 MWd/kgU Mole Fraction**	**116.6 MWd/kgU Mole Fraction**
U	0.555	0.495
Si	0.398	0.398
Pu, Am, Cm, Np	0.010	0.030
Gd, Nd, Pm, Sm, Eu	0.008	0.016
Zr, Nb	0.008	0.016
Mo	0.007	0.015
Ce, Pr	0.006	0.012
Ba, Sr	0.005	0.009
Y, La	0.003	0.006
Se, Te	0.001	0.002

Table 6.7. Calculated equilibrium phases in irradiated U_3Si_2 at 500°C.

Phase	52.5 MWd/kgU Mole Fraction	116.6 MWd/kgU Mole Fraction
$(U,Pu,Ce,Gd,Zr)_3Si_2$	0.9249	0.8618
U_3Si	0.0085	-
U_4MoSi_3	0.0354	0.0760
BaSi	0.0231	0.0445
Y_5Si_3	0.0031	0.0003
Y_5Si_4	-	0.0057
Se (liq)	0.0050	0.0116

Plutonium is expected to substitute for U, forming a $(U, Pu)_3Si_2$ solid solution. At both levels of burnup considered, Ce, Gd, and Zr are present below their associated solubility limits as described above, and thus not expected to precipitate in a second phase. The Y content is computed to result in the formation of Y_5Si_3 in the case of 52.5 MWd/kgU burnup, in contrast to the Y_5Si_4 seen experimentally. However, both Y_5Si_3 and Y_5Si_4 were computed to be present at a burnup of 116.6 MWd/kgU, likely as a result of different Si partitioning in the presence of higher FP content. Barium was predicted to form a monosilicide, and as the rare earth elements exceed their solubility limit in U_3Si_2, they likely form a solid solution secondary phase. Molybdenum is calculated to form the experimentally observed U_4MoSi_3 ternary, while elemental Se is expected to be present as a liquid at 500°C. Formation of FP-silicide phases does result in the reduction of some U_3Si_2 yielding an amount of the U-rich U_3Si phase at a burnup of 52.5 MWd/kgU. At 116.6 MWd/kgU burnup, U_3Si was not found to develop at 500°C as all U produced in the reduction of U_3Si_2 is associated with the U_4MoSi_3 ternary.

Additional equilibrium calculations were performed for a temperature range of 25-1250°C for comparison with DFT calculations and reported observations. The impact of fuel temperature on the phases present in the system at 52.5 and 116.6 MWd/kgU burnup is seen in Tables 6.8 and 6.9.

Table 6.8. Equilibrium-predicted FP phases together with $(U,Pu,Ce,Gd,Zr)_3Si_2$ as a function of temperature at a burnup of 52.5 MWd/kgU.

Element	25°C	200°C	400°C	600°C	800°C	1000°C	1250°C
U	U_3Si	U_3Si	U_3Si	U_3Si	Liquid*	Liquid*	Liquid*
Ba	BaSi	BaSi	BaSi	BaSi	-	-	-
Ce	-	-	-	-	-	-	-
Gd	-	-	-	-	-	-	-
Mo	U_4MoSi_3	U_4MoSi_3	U_4MoSi_3	U_4MoSi_3	U_4MoSi_3	U_4MoSi_3	U_4MoSi_3
Pu	-	-	-	-	-	-	-
Se	Se (s)	Se (s)	Se (l)	Se (l)	Se (g)	Se (g)	Se (g)
Y	YSi	Y_5Si_4	Y_5Si_3	Y_5Si_3	Y_5Si_4 Y_5Si_3	Y_5Si_3	-
Zr	-	-	-	-	-	-	-

*Liquid solution of (U,Si,Pu,Ba,Ce,Gd,Mo,Y,Zr)

Table 6.9. Equilibrium-predicted FP phases together with $(U,Pu,Ce,Gd,Zr)_3Si_2$ as a function of temperature at a burnup of 116.6 MWd/kgU

Element	25°C	200°C	400°C	600°C	800°C	1000°C	1250°C
U	U_3Si	-	-	-	Liquid*	Liquid*	Liquid*
Ba	BaSi	BaSi	BaSi	BaSi	BaSi	BaSi	-
Ce	-	-	-	-	-	-	-
Gd	-	-	-	-	-	-	-
Mo	U_4MoSi_3	U_4MoSi_3	U_4MoSi_3	U_4MoSi_3	U_4MoSi_3	U_4MoSi_3	U_4MoSi_3
Pu	-	-	-	-	-	-	-
Se	Se (s)	Se (s)	Se (l)	Se (l)	Se (g)	Se (g)	Se (g)
Y	YSi	YSi Y_5Si_4	Y_5Si_4	Y_5Si_4 Y_5Si_3	Y_5Si_4	YSi	YSi
Zr	-	-	-	-	-	-	-

*Liquid solution of (U,Si,Pu,Ba,Ce,Gd,Mo,Y,Zr)

At ~640°C at the lower burnup level, some BaSi is reduced to Ba. This reduction of BaSi is a result of the solubility of Ba in U [103] as it coincides with the degradation of U_3Si and the formation of a bcc phase, to which the Ba metal will partition to. At ~726°C, this bcc solution will begin to melt, ultimately forming a U,Si,Pu,Ba,Ce,Gd,Mo,Y,Zr liquid, where by 775°C, all remaining BaSi will have been reduced. Yttrium undergoes a series of transitions over the temperature range, forming a monosilicide at low temperatures before transitioning to Y_5Si_4, and then Y_5Si_3. At increased burnup, the Y_5Si_3 will transition back to Y_5Si_4 and then YSi forming from Si liberated by the decomposition of BaSi. As the temperature increases, the availability of Si for silicide formation will vary due to the FP phase changes noted above and decomposition of U_3Si such that partitioning of Si to the computed $(U,Pu,Ce,Gd,Zr)_3Si_2$ phase increases 1-3% between 25°C and 1250°C, depending on the level of burnup.

6.3.3.2. First Principles Calculations

Defect formation energies for select FPs (Ba, Ce, Gd, Pu, Y) occupying sites in U_3Si_2 were calculated by DFT using a 2x2x3 supercell, with Fig. 6.13 displaying the substitutional and interstitial sites considered. The U1, U2, Si, and interstitial sites at 4 Wyckoff positions (2b, 2c, 4g, and 4h), were explored for potential FP incorporation as these were previously shown to be the only interstitial positions for stable FP inclusion [97]. In the case of Y, two Y_5Si_4 structures were considered: Monoclinic ($P2_1/c$) and orthorhombic (Pnma) as both structures have been experimentally reported [116, 117], with the Pnma phase found to be more stable by 3meV [118].

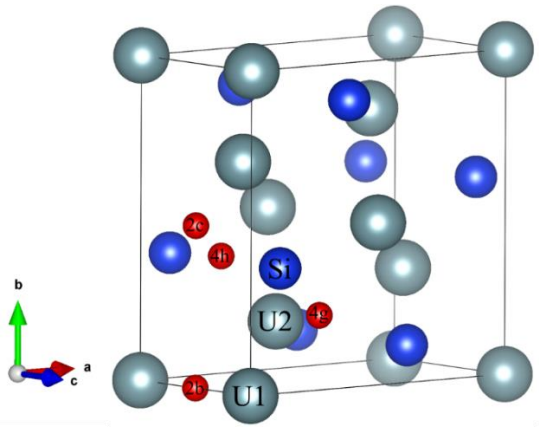

Fig. 6.13. U_3Si_2 structure with red spheres indicating potential interstitial sites.

Ce, Gd, and Pu were all found soluble in U_3Si_2, preferring substitution on the U2 site, while substitution on Si sites or interstitial formation yielded positive enthalpy changes. Elemental Ba and Y, however, were determined to be insoluble and resulted in secondary phase formation. The calculated ΔE_{sol} for FPs incorporated on U1 and U2 sites are listed in Table 6.10. The Si and 2b sites were also considered, however the energies for elements incorporated on those sites were prohibitively positive.

Various secondary FP-silicide phases were also considered and in the case of each FP (Ba, Ce, Gd, Pu, Y), the monosilicide was the most energetically stable as shown in Table 6.11. This was reflected as well in conventional thermodynamic equilibrium calculations mimicking the 0 K DFT condition (4 K).

Table 6.10. Calculated solvation energy, ΔE_{sol}, of Pu- and FP-silicide phases in U_3Si_2.

Element	**Mixing Phases**		**ΔE_{sol} (ev/atom)**
Barium	BaSi	U_3Si	1.078
	BaSi	U	1.007
	Ba_5Si3	USi	1.112
	Ba_2Si	USi	1.120
Cerium	CeSi	U_3Si	-0.122
	CeSi	U	-0.057
	Ce_5Si_4	U_3Si	-0.084
	Ce_5Si_4	U	-0.058
	Ce_5Si_3	USi	-0.812
	Ce_3Si_2	U, Si	-0.793
Gadolinium	GdSi	U_3Si	-0.453
	GdSi	U	-0.524
	Gd_5Si_4	U_3Si	-0.593
	Gd_5Si_4	U	-0.621
	Gd_5Si_3	USi	-0.704
	Gd	U_3Si	-1.205
Plutonium	PuSi	U_3Si	-0.589
	PuSi	U	-0.660

	Pu_3Si_2	U, Si	-1.061
	Pu_5Si_3	USi	-0.691
Yttrium	YSi	U_3Si	0.762
	YSi	U	0.692
	Y_5Si_4 ($P2_1/c$)	U_3Si	0.631
	Y_5Si_4 ($P2_1/c$)	U	0.602
	Y_5Si_4 (Pnma)	U_3Si	0.635
	Y_5Si_4 (Pnma)	U	0.607
	Y_5Si_3	USi	0.559

Table 6.11. Computed formation enthalpies, ΔH_f, for secondary phase formation.

Element	**Phase**	**ΔH_f (ev/atom)**
Cerium	CeSi	-0.651
	Ce_5Si_4	-0.598
	Ce_5Si_3	-0.550
Barium	$BaSi_2$	-0.359
	Ba_3Si_4	-0.406
	BaSi	-0.422
	Ba_5Si_3	-0.331
	Ba_2Si	-0.310
Gadolinium	Gd_5Si_3	-0.657
	Gd_5Si_4	-0.739
	GdSi	-0.825
Plutonium	Pu_3Si_2	-0.297
	Pu_5Si_3	-0.510
	PuSi	-0.633
Yttrium	YSi	-0.851
	Y_5Si_4 ($P2_1/c$)	-0.773
	Y_5Si_4 (Pnma)	-0.776
	Y_5Si_3	-0.720

6.4. Discussion

The solubility of Ce and Zr was expected to be considerable as they form silicides with the same stoichiometry and very similar structures. And indeed, Ce and Zr were determined to be soluble in the U_3Si_2 matrix with EDS-determined solubility limits of ~3.6 at%, where the measurements represent the first instance of Ce observed in U_3Si_2. While this is a low value, the concentrations of Ce or Zr produced during fuel burnup is unlikely to exceed this solubility limit. The measured value of Zr solubility falls below the previously reported value of about 9.5 at% [95] and requires further investigation. The current DFT calculations also indicated that the dissolution of Ce in U_3Si_2 to be more energetically favored than secondary phase formation.

Based on lattice parameter determinations from XRD, Mo-doping of U_3Si_2 resulted in an apparent lattice contraction of 0.003%, a value significantly below that calculated for other dopants and essentially negligible. This apparent lack of solubility agrees with EDS results as well as observations made by others [100, 119]. Yttrium was also seen to have no statistically significant solubility in the U_3Si_2 and DFT calculations indicate secondary phase formation is energetically favored over dissolution. The Ce and Zr solubility limits of ~3.6 at%, result in in a U_3Si_2 lattice expansion of 0.018% per atom% for Ce and a contraction of 0.015% per atom% for Zr. The variation agrees with expectations based on the lattice parameters of Ce_3Si_2, U_3Si_2, and Zr_3Si_2, wherein the Ce-silicide has the largest unit cell and Zr has the smallest of the three [10, 105, 120].

Above their solubility limits Ce and Zr in addition to Y were also observed to react with U_3Si_2 to form FP_5Si_4 phases. However, thermodynamically, Y_5Si_3 was predicted rather than the Y_5Si_4 we observed. The apparent inability to experimentally achieve equilibrium in the Y-doped sample may explain the discrepancy. YSi was observed by Ugajin and Itoh [95] in samples annealed above 1000°C as part of a rare earth monosilicide solid solution. The solubility of Y in this solid solution may account for the lack of Y_5Si_3 found in their work. Similarly, CeSi was not identified in our Ce-doped sample despite computational predictions and previously reported experimental efforts [95]. Thermodynamic calculations determined that the stability of CeSi is dictated by Si availability in the system. Small changes to Si content was found to result in the Ce phase switching between CeSi and Ce_5Si_4. As our samples were fabricated at different concentration and annealing conditions from those of Ugajin and Itoh [95], this explains their observation of CeSi while we found Ce_5Si_4 in our own samples. In Ugajin and Itoh's work [95], Zr was indicated to be present in an "unidentified U-Zr-Si compound." That U-Zr-Si phase may be the Zr_5Si_4 identified in samples in the current effort, where Ugajin and Itoh's [95] analysis may have been confounded by possible dissolution of U in Zr_5Si_4 and/or proximity to α-U making analysis difficult. The formation of the U_4MoSi_3 ternary phase in the Mo-doped sample in this work, however, does align with the report by Ugajin and Itoh [95] of a $U_4Mo(Mo_xSi_{1-x})Si_2$ phase.

In the current effort the presence of FPs Mo, Y, and Zr appear to encourage elemental U formation from U_3Si_2 at the high annealing temperatures, with the anomalous appearance U_3Si as well in the Y-containing samples. Uranium-rich phases are expected as a result of preferential FP-silicide formation over U_3Si_2. From 0 K DFT calculations the U_3Si phase is the most stable U-Si compound that forms in the reduction of U_3Si_2 by FPs, in agreement with thermodynamic equilibrium calculations. However, our samples were annealed at 1250°C, a temperature well above the ~920°C U_3Si decomposition temperature thus, the γ-U phase is the product of the reduction of U_3Si_2.

At 1250°C, Mo has significant solubility in γ-U [121] and the existence of a γ-(U,Mo) phase in the Mo-doped sample is consistent with reported experimental results [100, 119]. The thermodynamic calculations predict the occurrence of γ-U in the U_3Si_2 doped with Mo at temperatures above 800°C as the decomposition temperature of U_3Si phase decreases due to the higher stability of the γ-U phase with solute Mo. Uranium and Zr also form a highly stable solid solution of similarly structured γ-U/β-Zr at temperatures above ~615°C [64], confirmed by the current work by measurements of Zr dissolved in γ-U in the Zr-doped sample. As previously discussed, the existence of elemental U in the Y-doped sample is expected to be a result of the sample not reaching equilibrium.

Cerium-doped U_3Si_2 did not result in the development of phases other than Ce_5Si_4. While the individual Mo, Y, and Zr samples were fabricated by doping U_3Si_2 with either 30 at% Mo, 32 at% Y, or 31 at% Zr, the U_3Si_2 doped with Ce had a significantly lower concentration of 22 at%. The limit for U substitution by Ce does not appear to have been reached as no U-rich phases were observed.

The asymmetrical elemental concentrations in the diffusion couple in of 1:1 Mo:Zr alloy and U_3Si_2 indicates substantially differing rates and/or driving forces. While U and Si transport readily into the alloy, both FP elements had lower mobility in the silicide. Furthermore, the presence of Zr in the sample did not hinder the formation of a U-Mo-Si ternary phase containing a small fraction of Zr. The overall trend of diffusion and phase formation seen in the alloy reveals the preference for U to diffuse into the Zr-rich bcc phase at 1200°C. This echoes previously witnessed U diffusion in Zircalloy and is a result of elemental U and Zr forming similar bcc phases [122].

While Si did diffuse from U_3Si_2 into the Mo:Zr alloy, unlike U, it was not found to dissolve in any either alloy or intermetallic phase and manifested as either Zr_2Si or ZrMoSi, with Zr_2Si found adjacent to $ZrMo_2$ indicating its preference over forming a Mo-Zr solution phase. The $ZrMo_2$ or $Zr_{0.87}Mo_{0.13}$ solution phase will also preferentially react with the diffusing Si to produce the ZrMoSi ternary.

After high burnup the nature of the phases computed to form appear to remain unchanged as it progresses to an extreme that might be expected in the high burnup region of fuel pellets: U_3Si_2 reacts to form FP-silicides and U_3Si, as observed experimentally. The calculations also suggest there is insufficient Si liberated by fissioning to form stable FP-silicides causing an amount of the U_3Si_2 fuel to be reduced to U_3Si. For the computed burnups of 52.5 and 116.6 MWd/kgU, ~5.5 and ~12.3 atom%, respectively, of uranium from U_3Si_2 will be lost due to fissioning [123] and ~0.3% of the remaining U_3Si_2 will be reduced to U_3Si at typical operating conditions in the production of FP-silicide phases. In the case of 116.6 MWd/kgU burnup, smaller amounts of U_3Si were produced at low temperatures compared to the 52.5 MWd/kgU as U and Si produced through the consumption of U_3Si_2 during FP-silicide formation was used in the production U_4MoSi_3. As the concentration of Mo in the fuel doubled with the increase in burnup, more of the excess U and Si were incorporated into the generation of increased amounts of U_4MoSi_3. An example of elemental partitioning among the fuel and secondary phases for 52.5 MWd/kgU was estimated with the results seen in Table 6.12.

Table 6.12. Estimated phase assemblage/Si partitioning at 500°C in U_3Si_2 at 52.5 MWd/kgU burnup.

Phase	Mole Fraction
$(U,Pu,Zr,Ce,Pr,Np,Nd,Sm,Gd)_3Si_2$	0.8439
$(U,Pu,Zr,Ce,Pr,Np)_3Si$	0.0089
$U_4(Mo,Pd,Tc,Rh,Ru)Si_3$	0.0885
(Ba,Sr)Si	0.0226
$(Y,La)_5Si_3$	0.0030
(Cs,Rb)I	0.0018
Others (Cs,Rb,Te,Cd)	0.0318

7. U-Si-N System Thermodynamics and Phase Equilibria

Currently, only three research groups have prepared the UN- U_3Si_2 composite to study its properties [124-128]. Johnson et al. [125] fabricated the U_3Si_2 by conventional arc melting techniques and prepared the UN powder by hydriding-nitriding methods; the composite was formed by mixing ground silicide particles with the UN powder and sintering using spark plasma sintering (SPS) at 1450 °C. Liquid phase sintering of UN-U_3Si_2 fuel has been patented [127] as a means to improve densities, with sintering at temperatures close to the melting point of U_3Si_2, and where >90% theoretical density was achieved. Current work by Ortega et al. [128] and White et al. [124] use this technique, sintering at temperatures above 1700 °C.

As a consequence of sintering above the melting point of U_3Si_2 an unknown ternary phase of U-Si-N composition was observed by both Johnson, et al. [125] and White et al. [124] using SEM-EDS. Identification of the U-Si-N ternary phase was beyond the scope of their work, thus the composition of this phase has not been determined nor how its formation may affect overall fuel performance. In the current work efforts were made to identify the ternary phase using experimental and computational techniques.

7.1. Methodology

7.1.1. Experimental

7.1.1.1. Synthesis

U_3Si_2 ingots were arc-melted under gettered Ar-N_2 gas mixtures. The U_3Si_2 feedstock was characterized by SEM and XRD before arc melting. U_3Si_2 buttons were nitrided under two flowing cover compositions: 99% Ar - 1% N_2 (1% N_2) and 90% Ar – 10% N_2 (10% N_2). The arc melting technique was similar to the preparation of the U-Si samples. The O_2 concentration at the start of each sample melt was less than 10^{-14} ppm at the inlet and outlet of the system. Each sample was melted 3 times being flipped after each melt.

7.1.1.2. Characterization

SEM and XRD analysis were used to determine composition and for phase identification for each of the as-melted binary and nitrided samples. SEM samples were prepared by fracturing the buttons, potting them in epoxy and grinding and polishing using multiple grit sizes of SiC grinding discs and a 3 μm diamond suspension for the final polish. A Phenom ProX SEM (Phenom-World, Phoenix, Arizona, USA) equipped with a backscatter electron detector and energy dispersive spectrometer (EDS) was used for imaging and analyzing the as-melted samples. XRD samples were prepared by grinding button fragments using a mortar and pestle in an argon atmosphere glovebox. The powder was mounted on a Si crystal zero-background plate using a thin layer of vacuum grease, and then O-ring sealed inside a polymer dome while inside the glovebox to reduce the risk of oxidation. The polymer dome had an air scatter shield to minimize the background to signal contribution. The XRD pattern was collected on a Bruker XRD (D2 Phaser, Bruker AXS, Madison, WI, USA), from 15° to 90° 2θ with a 5 s hold and a 0.01° step size. Rietveld refinement of the powdered XRD were conducted using the MAUD software package [129]. To evaluate any phase transformation, differential scanning calorimetry (DSC) measurements were conducted using a DSC 404 F3 Pegasus (Netzsch Instruments) with a heating rate of 20 K min^{-1} to a final temperature of 973 K. Multiple thermal cycles were conducted on each sample to indicate reversible transitions.

7.1.2. Modeling

7.1.2.1. Density Functional Theory

First-principle calculations of the total energies of the different USi_x configurations were performed using DFT, as implemented in the Vienna ab initio Simulation Package (VASP) [79, 130] pseudopotential code. The electronic exchange and correlation energies were calculated with the generalized gradient approximation (GGA) using the Perdew-Burke-Ernzerhof (PBE) formalism [110]. The valence electrons that were explicitly treated in the calculations were $6s^2 6p^6 6d^2 5f^2 7s^2$ for U; $3s^2 3p^2$ for Si and a cut-off energy of 600 eV was used. Based on previous work by [43], the DFT+U formalism with the Dudarev implementation of the Hubbard correlation of U = 1.50 eV was used to handle the strong correlation of the 5f electrons. A k-point spacing of $2\pi \times 0.06$ $A^{\circ\,-1}$ was used to generate Monkhorst-Pack k-point grids for Brillouin sampling zone [131]. The total electronic energy convergence criterion was set to be at least 10^{-4} eV and the volume and shape of the cells were permitted to vary.

The DFT+U formalism was used as a fitness function for the evolutionary algorithm USPEX [132] to evaluate the stability and atomic structure of U_5Si_4 compound. The initial structures for the U_5Si_4 compound was randomly generated using the USPEX. Each new generation is then generated from a combination of: (i) the best-performing structure in the previous generation, and (ii) structures created using genetic operations. With this methodology the code is able to reliably predict ground state structures, and therefore is employed here.

The evolutionary algorithm was used in two different modes: (i) variable-composition and (ii) fixed-composition. The former was employed to construct the convex hull for the U-Si system and assess the reliability of the evolutionary algorithm. Up to 2500 structural relaxation calculations were performed in this mode. The latter mode was used to calculate the ground state for the known U_3Si_2 phase as a validation step, and for assessing the ground state of the U_5Si_4 with unit cells of $U_{10}Si_8$ and $U_{20}Si_{16}$. No initial assumptions about the crystal structures of the known phases were used in either of the modes. The reported structural symmetry was obtained from the FINDSYM [133] algorithm, using a tolerance of 0.1 Å. The single unit cell DFT+U method was used for assessing the thermodynamic stability of the U_5Si_4 structure that was proposed by Noël et al. [40].

The U-Si-N ternary phase spaced was probed using DFT+U methods; keeping the value of U_{eff} =1.5 eV for U_3Si_2 [43] and applying U_{eff} =1.85 eV for UN, two ternary candidates were investigated by systematically varying the U_{eff} values from 0-2.5 eV. A K-point spacing of <0.2 $Å^{-1}$ and a cut-off energy of 520 eV was used. Volume and shape of the unit cells were allowed to vary during minimization with a convergence criterion of 0.02 eV/Å**.**

7.1.2.2. Cluster Expansion

Using Cluster Expansion (CE) over the USi-USi_2 phase space the total configurational energy, i.e., enthalpy (H) of configurations (s) for USi_{2-x} ($2 \leq x \geq 1$), was determined where lattice sites i are occupied by Si or vacancies. The *H(s)* values are found from

$$H(s) = \sum_{\alpha_1=1}^{m_1} m_{\alpha_1}^{(1)} J_{\alpha_1}^{(1)} \sum_{i=1}^{N} s_i + \sum_{\alpha_2=1}^{m_2} m_{\alpha_2}^{(2)} J_{\alpha_2}^{(2)} \sum_{i=1}^{N}\sum_{j=1}^{N} s_i s_j + \sum_{\alpha_3=1}^{m_3} m_{\alpha_3}^{(3)} J_{\alpha_3}^{(3)} \sum_{i=1}^{N}\sum_{j=1}^{N}\sum_{k=1}^{N} s_i s_j s_k + \cdots \quad 7.1$$

where m_l is the number of clusters α_l that have interaction strength $J_{\alpha_l}$and multiplicity m_{α_l}, with l = 1, 2, 3 being the number of interacting lattice sites. To calculate the suitable $H(s)$, a finite set of clusters α and coefficients J_α were generated by using the MIT ab-initio phase stability (maps) code provided with the

ATAT toolkit [134, 135]. An optimized expression of $H(s)$ can be created using the formation energy E_f for a particular configuration, i, obtained from DFT, by using

$$\Delta E_f = E(\mathrm{USi}_{2-\mathrm{x}}) - [xE(\mathrm{USi}) + (1-x)E(\mathrm{USi}_2)], 2 \leq x \geq 1 \qquad 7.2$$

where $E(USi_{2-x})$, $E(USi)$ and $E(USi_2)$ are the DFT free energies of USi_{2-x}, pure USi and pure USi_2, respectively.

7.1.2.3. CALPHAD Modeling

The CALPHAD method was used to calculate the U-Si-N ternary phase diagram to represent the phase equilibria of the UN- U_3Si_2 composite fuel. This method uses mathematical models with adjustable parameters to represent Gibbs energy functions that are stored in a database and used to calculate phase equilibria across multicomponent systems. A set of internally consistent thermodynamic databases containing a description of the Gibbs energy for each phase is used for equilibrium calculations. The Gibbs energy functions are optimized using available experimental data from the literature to reproduce key thermodynamic properties. The binary systems U-N, U-Si and N-Si have been assessed using literature data [14, 37, 74, 136]and provide an extrapolation to the ternary U-Si-N phase space. For compounds with no experimental measurements, e.g., heat capacity, one can apply the Neumann-Kopp rule [60] which takes the average value of the pure elements in their reference state (SER). Then the molar Gibbs energy of a given phase α, is expressed as follows, with b_i being the stoichiometric factor and a_0 and a_1 are fitting coefficients:

$$G_m^{\alpha} - \sum_i b_i G_i^{SER} = a_0 + a_1 T \qquad 7.3$$

The ternary Gibbs energy parameters for U-Si-N compounds are catalogued in this manner since no experimentally available data confirms their compositional existence and therefore thermophysical data is also lacking.

7.2. Results

7.2.1. Experimental Results

The formation of a U-Si-N ternary phase was achieved by arc melting U_3Si_2 buttons under a partial nitrogen atmosphere. Figure 7.1 shows a picture of the U_3Si_2 button before and after arc melting under 90% Ar – 10% N_2.

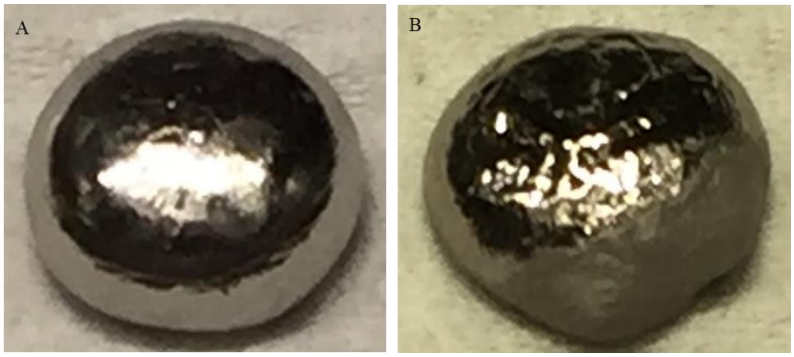

Fig. 7.1. Image of (A) U_3Si_2 before arc melting in N_2 atmosphere and (B) U_3Si_2 after arc melting in N_2 atmosphere

Phase separation in the arc melted samples occurred for those treated in either the 90% Ar – 10% N_2 or 99% Ar – 1% N_2 atmospheric conditions. The microstructures and XRD diffraction patterns for the U_3Si_2 samples nitrided in 1% N_2 and 10% N_2 are shown in Figs. 7.2 and 7.4, respectively.

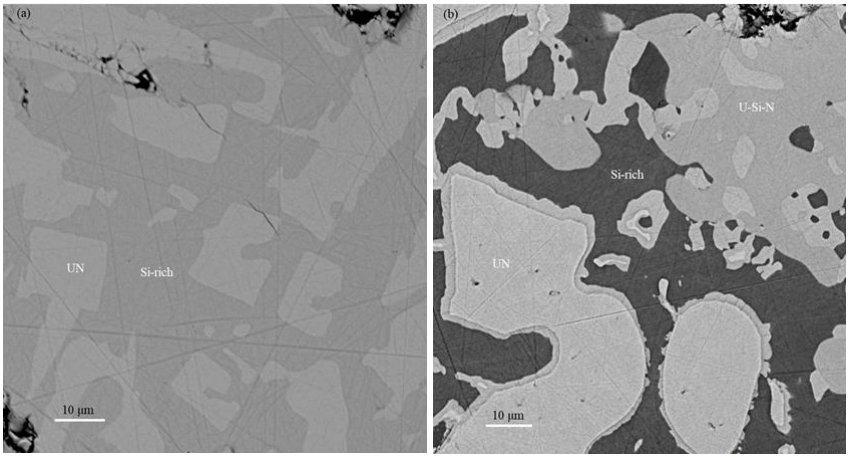

Fig. 7.2. SEM images of U_3Si_2 buttons that were nitrided under (a) 99% Ar - 1% N_2 (1% N_2) and (b) 90% Ar – 10% N_2 (10% N_2)

The microstructure for the sample prepared in the 1% N_2 appears less complex than that of the one prepared in 10% N_2. The images showed two phases identified as UN and a Si-rich phase by EDS analysis, and the XRD pattern for this sample revealed that the phases present are UN, U_3Si_2 and USi. As for the 10% N_2 cover gas prepared samples the backscatter images revealed that there are three phases, one of which contained all three elements as determined by EDS. The EDS system could not be utilized for quantitative determinations as the uranium electron density causes difficulties in measuring light element content. Figure 7.3 shows a representative EDS map for the 10%N_2 sample.

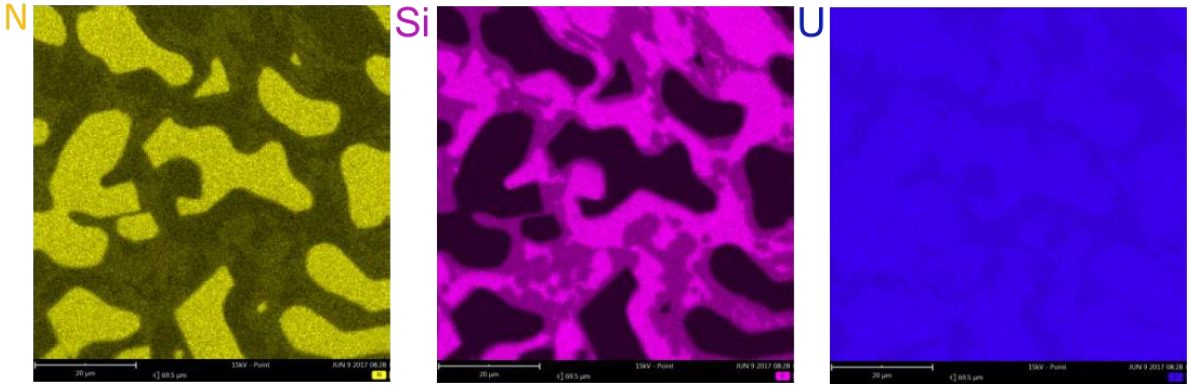

Fig. 7.3. EDS map of the U_3Si_2 nitrided in 90%Ar-10%N_2.

The XRD pattern for the 10% N_2 sample revealed UN, U_3Si_2, and USi as the major phases and a minor phase of unknown structure. There were three peaks at 26.085°, 29.638°, and 39.883° that could not be indexed. Additionally, these unidentified peaks did not appear in the sample prepared in 1% N_2. The minor phase present in the XRD pattern for the 10%N_2 sample could be associated with the U-Si-N phase that was found in the microstructure. When compared to the starting material the XRD diffraction patterns also revealed shifts in U_3Si_2 reflections for all angles in both the 1% and 10% N_2 samples.

As the carbide and nitride systems of uranium are similar in many respects [137, 138], it is suggested that the $U_{20}Si_{16}N_3$ and/or $U_3Si_2N_2$ could be a possible candidates for the observed ternary phase(s) analogous to the thermodynamically stable U-Si-C ternary compounds $U_{20}Si_{16}C_3$ and $U_3Si_2C_2$. Pöttgen et al. [139] have observed and determined the structure of the $U_{20}Si_{16}C_3$ and $U_3Si_2C_2$. As an attempt to fit the unidentified peaks, Rietveld refinements were performed considering the ternary structures present in the U-Si-C system; $U_{20}Si_{16}C_3$ (P6/mmm), $U_3Si_2C_2$ (I4/mmm) and $U_3Si_2C_3$ (I4/mmm and Immm). The unidentified peaks in the experimental pattern along with other low intensity reflections were a good fit to the $U_{20}Si_{16}N_3$ structure type. The refined structure showed a significant increase in the lattice parameter in comparison with $U_{20}Si_{16}C_3$, which is expected since nitrogen is a bigger element with larger atomic radius when compared to carbon. Table 7.1 gives a summary of the phases for each of the samples, with lattice parameters and the best fit ternary phase.

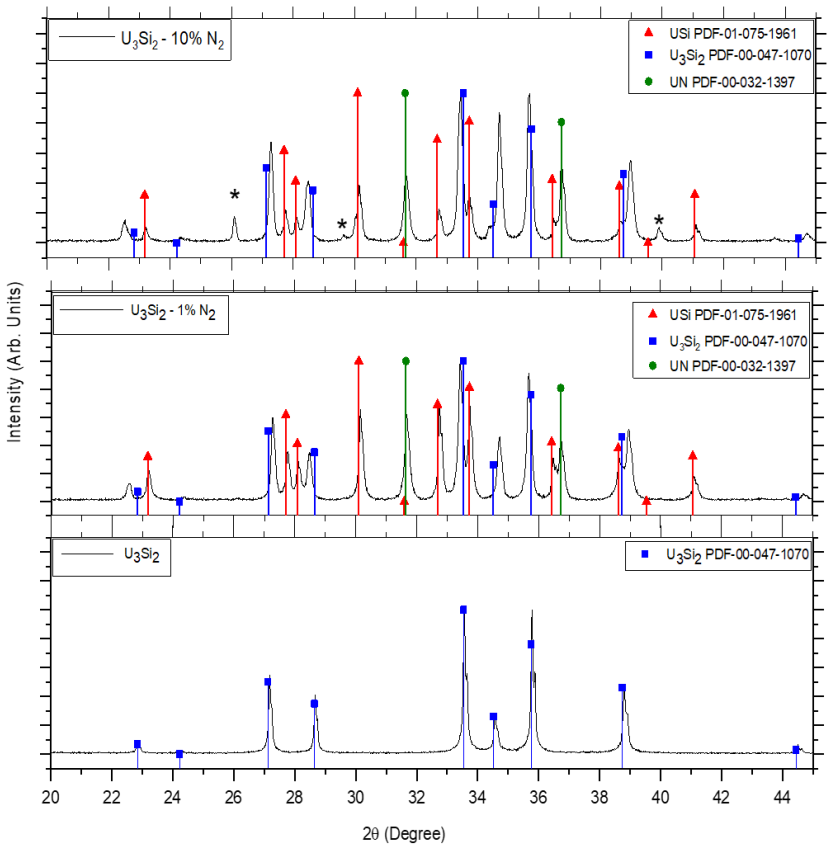

*Fig. 7.4. XRD patterns for U_3Si_2 samples that were nitrided under 99% Ar - 1% N_2 and (b) 90% Ar – 10% N_2 indexed using PDF's for U_3Si_2 [47], USi [47] and UN [140]. * indicates unidentified peaks.*

Table 7.1. Crystallographic Data of the U_3Si_2+10%N_2 and U_3Si_2+1%N_2 compared to the starting Material. Data was obtained using the MAUD [129] refinement software.

Sample	Phase	Space Group	Lattice parameters (Å)
U_3Si_2	U_3Si_2	P4/mbm	a=7.239 b=7.239 c = 3.905
U_3Si_2+1%N_2	U_3Si_2	P4/mbm	a=7.309 b=7.309 c=3.942
	USi	Pnma	a=5.662 b=7.663 c=3.900
	UN	Fm-3m	a=4.892 b=4.892 c=4.892
U_3Si_2+10%N_2	U_3Si_2	P4/mbm	a=7.307 b=7.307 c=3.941
	USi	Pnma	a=5.656 b=7.665 c=3.899
	UN	Fm-3m	a=4.891 a=4.891 c=4.891
	$U_{20}Si_{16}N_3$	P6/mmm	a=10.427 b=10.427 c=7.908

7.2.2. Computational Results

The symmetry of the optimized unit cells was verified with a tolerance of 0.05 Å for atomic positions and unit cell lengths. All U_{eff} values in-between and including 0.3eV and 1.9eV applied to the $U_{20}Si_{16}N_3$ system produced a unit cell that had *P6/mmm* symmetry. Lower U_{eff} values caused the unit cell to relax to a *P6/m* structure while for higher U_{eff} values it relaxed to a *P-3m1* structure. After geometry optimization of both the $U_{20}Si_{16}N_3$ and $U_3Si_2N_2$ structures, the lattice parameters were observed to vary with the on-site Coulombic correction (generally increasing with U_{eff} – the exception being the a/b parameter in $U_3Si_2N_2$). The variation in lattice parameters are reported in Table 7.2. Figure 7.5 shows the most stable calculated crystal structure for $U_{20}Si_{16}N_3$ and $U_3Si_2N_2$ respectively.

Table 7.2. Lattice constants of U20Si16N3 after geometry optimization with varying on-site Coulombic correction (Ueff) and the structure symmetry (with 0.05 tolerance). The lattice constants of U3Si2N2 are also given.

	$U_{20}Si_{16}N_3$				$U_3Si_2N_2$	
U_{eff}	a (Å)	b (Å)	c (Å)	Symmetry (0.05 Å tolerance)	a and b (Å)	c (Å)
0	10.2752	10.2752	7.9776	*P6/m*	3.6431	16.5160
0.1	10.2927	10.2874	7.9796	*P6/m*	3.6432	16.5397
0.3	10.3641	10.3687	7.9383	*P6/mmm*	3.6433	16.6101
0.5	10.2897	10.2910	8.0164	*P6/mmm*	3.6446	16.6840
0.7	10.5077	10.5215	8.1815	*P6/mmm*	3.6442	16.8093
0.9	10.4063	10.4244	8.0760	*P6/mmm*	3.6374	16.9837
1.1	10.4305	10.4427	8.1210	*P6/mmm*	3.6228	17.3304
1.3	10.4805	10.4937	8.1634	*P6/mmm*	3.6150	17.5354
1.5	10.5136	10.5315	8.1767	*P6/mmm*	3.5978	18.1608
1.7	10.5577	10.5720	8.2029	*P6/mmm*	3.6065	18.2064
1.9	10.5846	10.5854	8.2252	*P6/mmm*	3.6169	17.9487
2.1	10.5977	10.6253	8.2595	*P-3m1*	3.6401	17.8633
2.3	10.6330	10.6628	8.3959	*P1*	3.5835	18.7948
2.5	10.6489	10.6542	8.3455	*P1*	3.5885	18.8281
2.7	10.6621	10.6799	8.3611	*P1*	3.5929	18.8619
2.9	10.6722	10.6843	8.3660	*P1*	3.5982	18.8953

Since there is no experimental information concerning the thermophysical properties of the ternary U-Si-N compositions of interest, the parameters are adjusted based their stability with respect to the binary components. The ternary parameters for $U_{20}Si_{16}N_3$ and $U_3Si_2N_2$ were evaluated using the 'Mixer' feature in the Compound module of FACTSAGE. The Gibbs energy function for each of the ternary phases was

adjusted with a positive energy to destabilize the phases with respect to the binary phases. $U_{20}Si_{16}N_3$ was generated using $8U_3Si_2 + 3UN - 7U \rightarrow U_{20}Si_{16}N_3$, with the Gibbs energy parameter adjusted by 14,308 (J/mol) to obtain appropriate stability with

$$G_m^{\mathrm{U20Si16N3}} = 8\,G_m^{U3Si2} + 3\,G_m^{UN} - 7G_m^{U} + 14{,}308\ \text{(J/mol)} \qquad 7.4$$

Similarly, the other composition of interest, $U_3Si_2N_2$ was generated from

$$U_3Si_2 + 2UN - 2U \rightarrow U_3Si_2N_2 \qquad 7.5$$

and stabilized with 198,466 (J/mol):

$$G_m^{\mathrm{U3Si2N2}} = G_m^{U3Si2} + 2G_m^{UN} - 2G_m^{U} + 198{,}466\ \text{(J/mol)} \qquad 7.6$$

The coefficients for these ternary stoichiometric compound and their resulting enthalpies of formation are listed in Table 7.3.

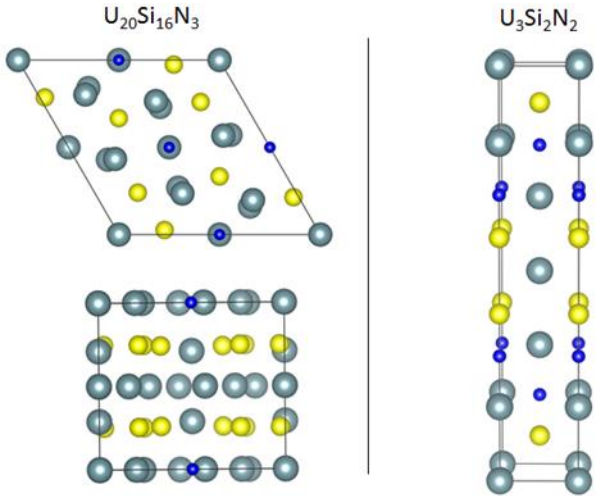

Fig. 7.5. Structure of $U_{20}Si_{16}N_3$ along the z-axis (upper) and along the x/y-axis (lower) and $U_3Si_2N_2$.

Table 7.3. Coefficients for Gibbs energy parameters evaluated via Neumann-Kopp type methods for the $U_{20}Si_{16}N_3$ and $U_3Si_2N_2$ ternary compounds

Gibbs Energy Parameter (J/mol)	$\Delta_f H^{\circ}_{298.15}$ **(kJ/mol)**
$G_m^{U20Si16N3} = -2650000.75 + 10394.46\,T - 1745.37\,T\,ln\,T - 0.17T^2 - 4.43\times10^3 + 10448284.8\,T^{-1} + 28.89\,T^{1.5} - 18372T^{.5}$	-2276.7
$G_m^{\mathrm{U3Si2N2}} = -590000.15 + 876.71\,\mathrm{T} - 186.45\,\mathrm{T}\ln T - 9.91\times10^{-3}T^2 - 7.53\times10^{-7}T^3 + 1874449.48\,T^{-1} + 2939.81\ln T$	-507.2

7.3. Discussion

The formation of a ternary phase in U-Si-N system was assessed by arc-melting U_3Si_2 buttons in partial N_2 atmosphere. Due to difficulties in controlling the arc in the presence nitrogen, only two conditions were tested, with 1% N_2 and 10% N_2 in Ar. While no ternary phase was observed in the lower N_2 samples, the addition of the nitrogen did cause a fraction of the U_3Si_2 to form USi and UN. Additionally, the lattice spacing of the remaining U_3Si_2 increased compared to the original U_3Si_2, indicating some solubility for nitrogen. The as-cast U_3Si_2 melted in higher N_2 concentration produced U_3Si_2, USi, UN and a ternary U-Si-N phases. The formation of the same ternary phase by different methods, demonstrates it is a thermodynamic stabile phase.

The uranium nitride and the uranium carbide systems are thermodynamically similar [137, 138]. The U-Si-C system has several ternary phases that have been identified and their structures are well characterized [52, 139, 141]. Two thermodynamically stable structures reported for the U-Si-C ternary include the $U_{20}Si_{16}C_3$ and $U_3Si_2C_2$ phases; additionally, varying degrees of carbon solubility in binary U-Si phases have been reported [52]. A thermodynamic assessment of U-Si-C has been performed by [74, 142], the latter description [74] relied on the binary descriptions of [143], [37] and [144] for the Si-C, U-Si and U-C descriptions respectively. The two ternary phases were assessed as stoichiometric compounds and the solubility of carbon in U_3Si_2 (up to 4% at.) was also included. Using the U-Si-C ternary as an analog to U-Si-N, we identified that two possible ternary phases could be $U_{20}Si_{16}N_3$ or $U_3Si_2N_2$, with supporting DFT results showing $U_{20}Si_{16}N_3$ being the more stable of the two. The XRD results also supported formation of the $U_{20}Si_{16}N_3$ phase.

Thermochemical values for the potential ternary phases were generated from the assessed binary systems using a Neumann-Kopp type algebraic sum of either elements in their standard state and/or binary or higher order constituents. Since there is no experimental information concerning the thermophysical properties on the ternary U-Si-N compositions of interest, the parameters adjusted based their stability with respect to the binary components. The U-Si-C diagram together with a calculated U-Si-N phase diagram are seen in Fig. 7.6.

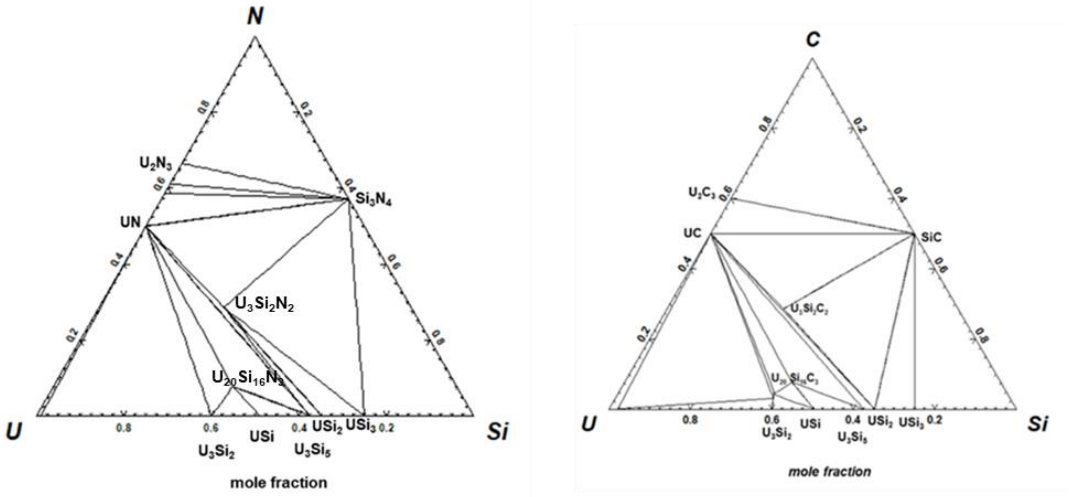

Fig. 7.6. The U-Si-C phase diagram and the analogous calculated U-Si-N phase diagram at 950°C.

8. Conclusions

The goal of the completed NEUP project was to develop an understanding of the phase equilibria of uranium silicide-nitride fuel, including behavior with respect to alternative cladding systems and response to the fission process. Early in the project it was understood that there was no longer a commercial interest in the inclusion of the nitride phase and thus the fundamental silicide-nitride composite work continued, but was de-emphasized.

This report thus represents efforts to better understand and refine the thermodynamics and phase equilibria of the U-Si and U-Si-N systems and has resulted in more detailed and accurate phase equilibria and thermodynamic models. Experimental and computational work addressing the compatibility of U_3Si_2 with Zircaloy-4, a ferritic FeCrAlY alloy, and SiC have revealed likely interactions and phase formation. Finally, experimental investigations supported by first principles calculations of U_3Si_2 together with representative fission product elements has revealed solubilities and potential phase formation during burnup, allowing prediction of phase behavior under irradiation. Key conclusions of the effort are provided below.

- The U_3Si_2 phase exhibits a homogeneity range from room temperature to its melting point as a hyperstoichiometric composition of U_3Si_2 was was found to be a single phase from room temperature to a maximum temperature of 1100 °C. This nonstoichiometric sample had a composition of 40.12 at.% Si and DFT predicted a stoichiometric deviation from $U_3Si_{1.95}$ to $U_3Si_{2.5}$. This data agrees with earlier claims of nonstoichiometry in U_3Si_2, and as such, a solid solution model was used for describing the U_3Si_2 phase field during the CALPHAD assessment.
- U_5Si_4 (*P6/mmm* space group) should not be considered as an equilibrium phase in the U-Si system. The phase could potentially be metastable with negative energy of formation located 2 meV above the U-Si convex hull and has a stable isostructural ternary phase, $U_{20}Si_{16}C_3$ (P*6/mmm*). This suggests that the binary could be stabilized by a third element.
- The crystal structure of the USi phase was confirmed as having a tetragonal supercell with an *I4/mmm* space group and invariant stoichiometry of $USi_{0.99}$.
- Above 450 °C, the U_3Si_5 phase was found to exhibit a homogeneity range. Below 450 °C, U_3Si_5 was found to exist with another unidentified phase. The nature of this other phase was unclear and further work is suggested. Regarding the equilibrium phase diagram, it is recommended that this phase transition not be included until more knowledge is acquired.
- The composition of the tetragonal α-USi_2 phase was found to be ~$USi_{1.84}$ after annealing for 72 hours at 1200 °C. It is to be reported as a line compound because any composition above 64.8 at.% Si exists as a two-phase region between $USi_{1.84}$ and USi_3
- The stoichiometric USi_2 phase was found to be metastable from both experimental and computational techniques, and as such, it is recommended that the phase not be a part of the U-Si equilibrium phase diagram. The AlB_2-type USi_2 phase was found to be dynamically stable and had a formation energy 2meV above the convex hull indicating that it could be formed experimentally if conditions are favorable. This serves as an explanation for the experimental inconsistency.
- A thermodynamic database for the U-Si phase containing the optimized parameters has been developed and an overall good agreement between the calculated diagram and the experimental phase diagram data was achieved. Representing the U_3Si_2 phase as a 3 sublattice model accurately accounts for Si interstitial defects, which are the primary defects found in this structure.
- Investigations of the U-Si-N system identified the ternary phase $U_{20}Si_{16}N_3$ with space group *P6/mmm*, demonstrating similarity with the U-Si-C system. First principles calculations for the $U_{20}Si_{16}N_3$ and $U_3Si_2N_2$ phases determined only the latter to be energetically favorable compared to UN and U_2N_3 for value U_{eff} values of ~1.1 eV. This value also produced lattice parameters very closely to those observed experimentally. The $U_3Si_2N_2$ phase was only energetically stable

assuming high U_{eff} values (2.1eV-2.5eV), which indicates it is likely not be stable in the U-Si-N system.

- The impact of individual FPs on the fuel was considered through the characterization of samples doped with 5 wt% of Ce, Mo, Y, or Zr. Of the four FPs considered, Ce and Zr were determined to have ~3.6 at% solubility in U_3Si_2 while Mo and Y were found to be insoluble, and the previously predicted U_4MoSi_3 was observed.
- Reduction of U_3Si_2 from FP silicide formation occurs and results in the precipitation of an additional U-rich phase. DFT calculations were used to evaluate the behavior of the FPs Ba and Gd as well as Pu in the absence of other data. They all were predicted to form monosilicides in equilibrium with U_3Si_2, in agreement with conventional thermodynamic equilibrium calculations. In addition, Ce, Gd, and Pu were computed to have finite solubility in U_3Si_2.
- A set of thermodynamic values were generated for U_3Si_2-FP to predict phase behavior in irradiated fuel. Utilizing the thermodynamic models and values it was determined that FP-silicide formation will cause some reduction of a minor fraction of U_3Si_2 to a lower silicide at high burnups.

9. References

[1] S. Ray, P. Xu, L. Hallstadius, F. Boylan, and S. Johnson, "Westinghouse Accident Tolerant Fuel Program," presented at the TopFuel 2015, Zurich, Switzerland, 2015.

[2] A. T. Nelson, J. T. White, D. D. Byler, J. T. Dunwoody, J. A. Valdez, and K. J. McClellan, "Overview of Properties and Performance of Uranium-Silicide Compounds for Light Water Reactor Applications," in *American Nuclear Society 2014 Summer Meeting*, Reno, Nevada, 2014, vol. 110: American Nuclear Society, pp. 987-989.

[3] K. A. Terrani, S. J. Zinkle, and L. L. Snead, "Advanced oxidation-resistant iron-based alloys for LWR fuel cladding," *Journal of Nuclear Materials*, vol. 448, no. 1-3, pp. 420-435, May 2014, doi: 10.1016/j.jnucmat.2013.06.041.

[4] K. Barrett, S. Bragg-Sitton, and D. Galicki, "Advanced LWR Nuclear Fuel Cladding System Development Trade-off Study," Idaho National Laboratory, 2012.

[5] N. R. Brown, A. Aronson, M. Todosow, R. Brito, and K. J. McClellan, "Neutronic performance of uranium nitride composite fuels in a PWR," *Nuclear Engineering and Design*, vol. 275, pp. 393-407, Aug 2014, doi: 10.1016/j.nucengdes.2014.04.040.

[6] N. R. Brown, M. Todosow, and A. Cuadra, "Screening of advanced cladding materials and UN-U3Si5 fuel," *Journal of Nuclear Materials*, vol. 462, pp. 26-42, Jul 2015, doi: 10.1016/j.jnucmat.2015.03.016.

[7] G. J. Youinou and R. S. Sen, "IMPACT OF ACCIDENT-TOLERANT FUELS AND CLADDINGS ON THE OVERALL FUEL CYCLE: A PRELIMINARY SYSTEMS ANALYSIS," *Nuclear Technology*, vol. 188, no. 2, pp. 123-138, Nov 2014.

[8] "Thermodynamics for Advanced Fuels-International Database." https://www.oecd-nea.org/science/taf-id (accessed.

[9] "SGTE Casebook: Thermodynamics at Work , Second Edition," *Sgte Casebook: Thermodynamics at Work , Second Edition*, pp. 1-454, 2008, doi: 10.1533/9781845693954.

[10] K. Remschnig, T. Le Bihan, H. Noel, and P. Rogl, "Structural chemistry and magnetic behavior of binary uranium silicides," *J. Solid State Chem.*, vol. 97, pp. 391-399, 1992.

[11] R. C. Birtcher, J. W. Richardson, and M. H. Mueller, "Amorphization of U3Si2 by ion or neutron irradiation," *Journal of Nuclear Materials*, vol. 230, no. 2, pp. 158-163, Jun 1996, doi: 10.1016/0022-3115(96)00160-2.

[12] E. G. Obbard *et al.*, "Anisotropy in the thermal expansion of uranium silicide measured by neutron diffraction," *Journal of Nuclear Materials*, vol. 508, pp. 516-520, Sep 2018, doi: 10.1016/j.jnucmat.2018.04.049.

[13] J. T. White, A. T. Nelson, D. D. Byler, D. J. Safarik, J. T. Dunwoody, and K. J. McClellan, "Thermophysical properties of U3Si5 to 1773 K," *Journal of Nuclear Materials,* vol. 456, pp. 442-448, Jan 2015, doi: 10.1016/j.jnucmat.2014.10.021.

[14] S. C. Middleburgh, R. W. Grimes, E. J. Lahoda, C. R. Stanek, and D. A. Andersson, "Non-stoichiometry in U3Si2," *Journal of Nuclear Materials,* vol. 482, pp. 300-305, Dec 2016, doi: 10.1016/j.jnucmat.2016.10.016.

[15] D. A. Andersson, X. Y. Liu, B. Beeler, S. C. Middleburgh, A. Claisse, and C. R. Stanek, "Density functional theory calculations of self- and Xe diffusion in U3Si2," *Journal of Nuclear Materials,* vol. 515, pp. 312-325, Mar 2019, doi: 10.1016/j.jnucmat.2018.12.021.

[16] J. T. White, A. T. Nelson, J. T. Dunwoody, D. D. Byler, D. J. Safarik, and K. J. McClellan, "Thermophysical properties of U5Si3 to 1773K," *J. Nucl. Mater.,* vol. 464, pp. 275-280, 2015.

[17] S. C. Vogel, "gsaslanguage: a GSAS script language for automated Rietveld refinements of diffraction data," *Journal of Applied Crystallography,* vol. 44, pp. 873-877, Aug 2011, doi: 10.1107/s0021889811023181.

[18] K. Momma and F. Izumi, "VESTA 3 for three-dimensional visualization of crystal, volumetric and morphology data," *Journal of Applied Crystallography,* vol. 44, pp. 1272-1276, Dec 2011, doi: 10.1107/s0021889811038970.

[19] W. H. Zachariasen, "CRYSTAL CHEMICAL STUDIES OF THE 5F-SERIES OF ELEMENTS .8. CRYSTAL STRUCTURE STUDIES OF URANIUM SILICIDES AND OF CESI2, NPSI2 AND PUSI2," *Acta Crystallographica,* vol. 2, no. 2, pp. 94-99, 1949, doi: 10.1107/s0365110x49000217.

[20] S. Takajo and S. C. Vogel, "Determination of pole figure coverage for texture measurements with neutron time-of-flight diffractometers," *Journal of Applied Crystallography,* vol. 51, pp. 895-900, Jun 2018, doi: 10.1107/s1600576718007732.

[21] M. J. Noordhoek, T. M. Besmann, D. Andersson, S. C. Middleburgh, and A. Chernatynskiy, "Phase equilibria in the U-Si system from first-principles calculations," *J. Nucl. Mater.,* vol. 479, pp. 216-223, 2016.

[22] D. A. Lopes, V. Kocevski, T. L. Wilson, E. E. Moore, and T. M. Besmann, "Stability of U5Si4 phase in U-Si system: Crystal structure prediction and phonon properties using first-principles calculations," *Journal of Nuclear Materials,* vol. 510, pp. 331-336, Nov 2018, doi: 10.1016/j.jnucmat.2018.08.026.

[23] E. Jossou, U. Eduok, N. Y. Dzade, B. Szpunar, and J. A. Szpunar, "Oxidation behaviour of U3Si2: an experimental and first principles investigation," *Physical Chemistry Chemical Physics,* vol. 20, no. 7, pp. 4708-4720, Feb 2018, doi: 10.1039/c7cp07154j.

[24] J. Wang, K. Wang, C. H. Ma, and L. D. Xie, "Critical evaluation and thermodynamic optimization of the (U plus Bi), (U plus Si) and (U plus Sn) binary systems," *Journal of Chemical Thermodynamics,* vol. 92, pp. 158-167, Jan 2016, doi: 10.1016/j.jct.2015.08.029.

[25] S. C. Middleburgh, A. Claisse, D. A. Andersson, R. W. Grimes, P. Olsson, and S. Maskova, "Solution of hydrogen in accident tolerant fuel candidate material: U3Si2," *Journal of Nuclear Materials,* vol. 501, pp. 234-237, Apr 2018, doi: 10.1016/j.jnucmat.2018.01.018.

[26] J. Hafner and G. Kresse, "The Vienna Ab-initio Simulation Program VASP: An efficient and versatile tool for studying the structural, dynamic, and electronic properties of materials," *Properties of Complex Inorganic Solids,* pp. 69-82, 1997.

[27] V. I. Anisimov, J. Zaanen, and O. K. Andersen, "BAND THEORY AND MOTT INSULATORS - HUBBARD-U INSTEAD OF STONER-I," *Physical Review B,* vol. 44, no. 3, pp. 943-954, Jul 1991, doi: 10.1103/PhysRevB.44.943.

[28] A. I. Liechtenstein, V. I. Anisimov, and J. Zaanen, "DENSITY-FUNCTIONAL THEORY AND STRONG-INTERACTIONS - ORBITAL ORDERING IN MOTT-HUBBARD INSULATORS," *Physical Review B,* vol. 52, no. 8, pp. R5467-R5470, Aug 1995, doi: 10.1103/PhysRevB.52.R5467.

[29] S. L. Dudarev, D. N. Manh, and A. P. Sutton, "Effect of Mott-Hubbard correlations on the electronic structure and structural stability of uranium dioxide," *Philosophical Magazine B-Physics of Condensed Matter Statistical Mechanics Electronic Optical and Magnetic Properties,* vol. 75, no. 5, pp. 613-628, May 1997, doi: 10.1080/13642819708202343.
[30] Y. Mishin, M. R. Sorensen, and A. F. Voter, "Calculation of point-defect entropy in metals," *Philosophical Magazine a-Physics of Condensed Matter Structure Defects and Mechanical Properties,* vol. 81, no. 11, pp. 2591-2612, Nov 2001, doi: 10.1080/01418610108216657.
[31] B. H. Toby, "R factors in Rietveld analysis: How good is good enough?," *Powder Diffraction,* vol. 21, no. 1, pp. 67-70, Mar 2006, doi: 10.1154/1.2179804.
[32] S. Maskova, K. Miliyanchuk, and L. Havela, "Hydrogen absorption in U3Si2 and its impact on electronic properties," *Journal of Nuclear Materials,* vol. 487, pp. 418-423, Apr 2017, doi: 10.1016/j.jnucmat.2017.02.036.
[33] A. Mohamad, Y. Ohishi, H. Muta, K. Kurosaki, and S. Yamanaka, "Thermal and mechanical properties of polycrystalline U3Si2 synthesized by spark plasma sintering," *Journal of Nuclear Science and Technology,* vol. 55, no. 10, pp. 1141-1150, 2018, doi: 10.1080/00223131.2018.1480431.
[34] L. D. Loch, G. B. Engle, G. B. Snyder, and W. H. Duckworth, "Survery of Refractory Uranium Compounds," Battelle Memorial Institute, Columbus, OH, 1959.
[35] K. M. Taylor and C. H. McMurtry, "Synthesis and Fabrication of Refractory Uranium Compounds," Carborundum Company, 2010.
[36] K. A. Terrani, "Accident tolerant fuel cladding development: Promise, status, and challenges," *Journal of Nuclear Materials,* vol. 501, pp. 13-30, Apr 2018, doi: 10.1016/j.jnucmat.2017.12.043.
[37] A. Berche, C. Rado, O. Rapaud, C. Gueneau, and J. Rogez, "Thermodynamic study of the U-Si system," *Journal of Nuclear Materials,* vol. 389, no. 1, pp. 101-107, May 2009, doi: 10.1016/j.jnucmat.2009.01.014.
[38] A. Kaufmann, B. Cullity, and G. Bitsianes, "URANIUM-SILICON ALLOYS," *Transactions of the American Institute of Mining and Metallurgical Engineers,* vol. 209, pp. 23-27, 1957.
[39] A. Brown and J. J. Norreys, "BETA-POLYMORPHS OF URANIUM AND THORIUM DISILICIDES," *Nature,* vol. 183, no. 4662, pp. 673-673, 1959, doi: 10.1038/183673a0.
[40] H. Noel, J. P. Queneau, J. P. Durand, and P. Colomb, "A new phase, U5Si4," presented at the International Conference on Strongly Correlated Electron Systems-SCSES98, Paris, 1998.
[41] R. E. Hoggan, L. F. He, and J. M. Harp, "Interdiffusion behavior of U3Si2 with FeCrAl via diffusion couple studies," *Journal of Nuclear Materials,* vol. 502, pp. 356-369, Apr 2018, doi: 10.1016/j.jnucmat.2017.10.057.
[42] V. Kocevski, D. A. Lopes, and T. M. Besmann, "Investigation of the on-site Coulomb correction and temperature dependence of the stability of U-Si phases using DFT plus U," *Journal of Nuclear Materials,* vol. 524, pp. 157-163, Oct 2019, doi: 10.1016/j.jnucmat.2019.07.003.
[43] M. J. Noordhoek, T. M. Besmann, D. Andersson, S. C. Middleburgh, and A. Chernatynskiy, "Phase equilibria in the U-Si system from first-principles calculations," *Journal of Nuclear Materials,* vol. 479, pp. 216-223, Oct 2016, doi: 10.1016/j.jnucmat.2016.07.006.
[44] T. L. Bihan, H. Noel, and P. F. YRogl, "Crystal Structure of the Uranium Monosilicide (USi)," *Journal of Alloys and Compounds,* vol. 240, pp. 128-133, 1996.
[45] B. T. Noordhoek M., Andersson D. , Middleburgh S. and Chernatynskiy A., "Phase equilibria in the U-Si system from first-principles calculations," *Journal of Nuclear Materials,* pp. 216-223, 2016.
[46] T. L. Ulrich, S. C. Vogel, J. T. White, E. Sooby Wood, and T. M. Besmann, "High temperature neutron diffraction investigation of U3Si2," *Materialia,* vol. 9, 2020.
[47] K. Remschnig, T. Le Bihan, H. Noel, and P. Rogl, "STRUCTURAL CHEMISTRY AND MAGNETIC-BEHAVIOR OF BINARY URANIUM SILICIDES," *Journal of Solid State Chemistry,* vol. 97, no. 2, pp. 391-399, Apr 1992, doi: 10.1016/0022-4596(92)90048-z.

[48] H. Vaugoyeau, L. Lombard, and J. P. Morlevat, "STUDY OF URANIUM-SILICON EQUILIBRIUM DIAGRAM," *Journal of Nuclear Materials,* vol. 39, no. 3, pp. 323-+, 1971, doi: 10.1016/0022-3115(71)90153-x.
[49] M. E. E. Wilson T. L., Lopes D. A. , Kocevski V. , Wood E. S., White J. T., Nelson A. T. , McMurray J. W. , Middleburg S. C. , Xu P. & Besmann T. M., "Uranium nitride-silicide advanced nuclear fuel: higher efficiency and greater safety," *Advances in Applied Ceramics,* pp. 76-81, 2018.
[50] J. T. White, A. T. Nelson, J. T. Dunwoody, D. D. Byler, and K. J. McClellan, "Thermophysical properties of USi to 1673 K," *Journal of Nuclear Materials,* vol. 471, pp. 129-135, Apr 2016, doi: 10.1016/j.jnucmat.2016.01.013.
[51] M. D. L. Pinto, "URANIUM-IRON-SILICON SYSTEM . NEW PHASE U2FESI3," *Acta Crystallographica,* vol. 21, pp. 999-&, 1966, doi: 10.1107/s0365110x6600433x.
[52] P. Rogl and H. Noel, "The C-Si-U system (carbon-silicon uranium)," *Journal of Phase Equilibria,* vol. 16, no. 1, pp. 66-72, Feb 1995, doi: 10.1007/bf02646251.
[53] C. W. Bale *et al.*, "FactSage thermochemical software and databases, 2010–2016," (in English), *CALPHAD: Computer Coupling of Phase Diagrams and Thermochemistry,* Article vol. 54, pp. 35-53, Sept 2016, doi: 10.1016/j.calphad.2016.05.002.
[54] G. Kimmel, B. Sharon, and M. Rosen, "STRUCTURE AND PHASE-STABILITY OF URANIUM-SILICON U3SI AT LOW-TEMPERATURES," *Acta Crystallographica Section B-Structural Science,* vol. 36, no. OCT, pp. 2386-2389, 1980, doi: 10.1107/s0567740880008783.
[55] A. E. Dwight, "Study of the Uranium-Aluminum-Silicon System," Argonne National Laboratory, 1982.
[56] J. T. White, A. T. Nelson, D. D. Byler, J. A. Valdez, and K. J. McClellan, "Thermophysical properties of U3Si to 1150 K," *Journal of Nuclear Materials,* vol. 452, no. 1-3, pp. 304-310, Sep 2014, doi: 10.1016/j.jnucmat.2014.05.037.
[57] C. K. Chung *et al.*, "Enthalpies of formation and phase stability relations of USi, U3Si5 and U3Si2," *Journal of Nuclear Materials,* vol. 523, pp. 101-110, Sep 2019, doi: 10.1016/j.jnucmat.2019.05.052.
[58] L. Kaufman, *Hume-Rothery and CALPHAD thermodynamics* (Calphad and Alloy Thermodynamics). 2002, pp. 3-19.
[59] L. Kaufman and H. Bernstein, *Computer Calculation of Phase Diagram. With Special Reference to Refractory Metals*. Academic Press, New York, NY, 1970.
[60] H. L. Lukas, S. G. Fries, and B. Sundman, *Computational Thermodynamics, The Calphad Method*. Cambridge University Press, 2007.
[61] M. Perrut and (ONERA), "Thermodynamic Modeling by the CALPHAD Method and its Applications to Innovative Materials," *AerospaceLab,* vol. 10, no. 9, pp. 1-11, 2015, doi: 10.1276212015.AL09.10.
[62] R. Ferro and G. Cacciamani, "Remarks on crystallochemical aspects in thermodynamic modeling," *Calphad-Computer Coupling of Phase Diagrams and Thermochemistry,* vol. 26, no. 3, pp. 439-458, Sep 2002, Art no. Pii s0364-5916(02)00056-1, doi: 10.1016/s0364-5916(02)00056-1.
[63] Z. K. Liu, "First-Principles Calculations and CALPHAD Modeling of Thermodynamics," *Journal of Phase Equilibria and Diffusion,* vol. 30, no. 5, pp. 517-534, Oct 2009, doi: 10.1007/s11669-009-9570-6.
[64] A. T. Dinsdale, "SGTE data for pure elements," *Calphad,* vol. 15, pp. 317-425, 1991.
[65] M. Hillert, "The compound energy formalism," *Journal of Alloys and Compounds,* vol. 320, no. 2, pp. 161-176, May 2001, doi: 10.1016/s0925-8388(00)01481-x.
[66] C. K. Chung *et al.*, "Enthalpies of formation and phase stability relations of USi, U3Si5 and U3Si2," *Journal of Nuclear Materials,* vol. 523, pp. 101-110, Sep 2018, doi: 10.1016/j.jnucmat.2019.05.052.

[67] P. Gross, Hayman, C., and H. Clayton, "Heats of formation of uranium silicides and nitrides," in In Thermodynamic ofNuclear Materials- Proceedings of Symposium on Thermodynamics of Nuclear Materials, International Atomic Energy Agency, Veinna, 1962, pp. 653-665.

[68] C. B. Alcock and P. Grieveson, "THERMODYNAMIC STUDY OF COMPOUNDS OF URANIUM WITH SILICON, GERMANIUM, TIN, AND LEAD," (in English), *Journal of the Institute of Metals*, Article vol. 90, no. 8, pp. 304-&, 1962.

[69] R. Birtcher, M. Mueller, J. Richardson, and J. Faber, "Neutron Irradiated Uranium Silicides Studied by Neutron Diffraction and Rietveld Analysis," in *MRS Proceedings*, 1989, vol. 166, p. 437, doi: 10.1557/PROC-166-437.

[70] P. A. G. O'Hare, M. Ader, W. N. Hubbard, G. K. Johnson, and J. L. Settle, *Calorimetric studies on actinide compounds and materials of interest in reactor technology* (no. Proceedings series; 2 v.; v. 2). International Atomic Energy Agency, Vienna (Austria); Symposium on the thermodynamics of nuclear materials; Vienna, Austria;, 1975.

[71] P. Gross, Hayman, C., and H. Clayton, "Heats of formation of uranium silicides and nitrides," in *In Thermodynamic of Nuclear Materials- Proceedings of Symposium on Thermodynamics of Nuclear Materials, International Atomic Energy Agency*, Veinna, 1962, pp. 653-665.

[72] J. Lacaze and B. Sundman, "Am assessment of the Fe-C-Si system," *Met Trans A*, vol. 22A, p. 2211, 1991.

[73] S. Chatain, C. Guéneau, and D. Labroche, "Thermodynamic assessment of the Fe-U binary system," *J. Phase. Equil*, vol. 24, p. 122, 2003.

[74] N. Dupin, "Revision of the thermodynamic assessment of the C-Si-U ternary system," Calcul Thermodynamique, 2012.

[75] D. Berthebaud, O. Tougait, and A. P. Gonçalves, "Phase relations and stabilities at 900°C in the U-Fe-Si ternary system," *Intermet*, vol. 16, p. 373, 2008.

[76] R. E. Hoggan, L. He, and J. M. Harp, "Interdiffusion behavior of U3Si2 with FeCrAl via interdiffusion couple studies," *J. Nucl. Mater*, 2018.

[77] L. He, J. M. Harp, R. E. Hoggan, and A. R. Wagner, "Microstructure studies of interdiffusion behavior of U3Si2/Zircaloy-4 at 800 and 1000 degrees C," *Journal of Nuclear Materials*, vol. 486, pp. 274-282, Apr 2017, doi: 10.1016/j.jnucmat.2017.01.035.

[78] W. H. R. Ischia G., Lutterotti L. , and Berberich F., "Quantitative Rietveld texture analysis from single synchrotron diffraction images.," *J. Appl. Cryst.*, pp. 377-380, 2005.

[79] F. J. Kresse G., "Efficient iterative schemes for ab initio total-energy calculations using a plane-wave basis set," *Phys. Rev. B 54*, p. 11169, 1996.

[80] B. K. Perdew J. P., and Ernzerhof M., "Generalized Gradient Approximation Made Simple," *Physical Review Letters*, pp. 3865-3868, 1997.

[81] B. G. A. Dudarev S. L., Savrasov S. Y., Humphreys C. J. , and Sutton A. P., "Electron-energy-loss spectra and the structural stability of nickel oxide: An LSDA+U study," *Physical Review B*, pp. 1505-1509, 1998.

[82] O. Redlich and A. T. Kister, "Algebraic representation of thermodynamic propertiesand the classification of solutions," *Industrial and Engineering Chemistry*, vol. 40, pp. 345-348, 1948.

[83] R. B. Adamson, "Zirconium Production and Technology: The Kroll Medal Papers 1975-2010," *ASTM International*, 2010.

[84] T. A. Meredig B., Hansen H. A. , Wolverton C., and van de Walle A., "Method for locating low-energy solutions within DFT+U," *Physical Review B*, p. 195128, 2010.

[85] T. I. Togo A, "First principles phonon calculations in materials science," *Scripta Materialia*, pp. 1-5, 2015.

[86] M. Zinkevich, N. Mattern, Seifert-H.J., and E. Gmelin, "A thermodynamic assessment of the Fe-Gd-Mo system," *Scandanavian Journal of Mettalurgy*, vol. 31, pp. 34-51, 2002.

[87] A. P. Goncalves, C. T. Almeida, J. Ray, and J. P. Spirlet, "Phase relations and single crystal growth of U-Fe-M (M=Al,Si) Compounds with ThMn12 type structure," *Material Leters,* vol. 19, pp. 13-16, 1994.
[88] A. C. Kubaschewski O., Spencer P., *Materials Thermochemistry, 6th ed.,* . Oxford: Pergamom Press, 1993.
[89] P. Söderlind, "First-principles phase stability, bonding, and electronic structureof actinide metals," *Journal of Electron Spectroscopy and Related Phenomena,* pp. 2-7, 2013.
[90] H. G. Jain A., Ong S. P., Moore C. J. , Fischer C. C., Persson K. A., and Ceder G., "Formation enthalpies by mixing GGA and GGA," *Physical Review B,* p. 045115, 2011.
[91] D. A. Lopes, V. Kocevski, T. L. Wilson, E. E. Moore, and T. M. Besmann, "Stability of U5Si4 phase in U-Si system: Crystal structure prediction and phonon properties using first-principles calculationscd," *Journal of Nuclear Materials,* vol. 510, pp. 331-336, 2018.
[92] S. C. Middleburgh, R. W. Grimes, E. J. Lahoda, C. R. Stanek, and D. A. Andersson, "Non-stoichiometry in U3si2 " *J. Nucl. Mater.,* vol. 482, pp. 300-305, 2016.
[93] T. L. Ulrich *et al.,* "Modeling the U-Si and U-Si-N systems based on computed and experimental phase analysis, NEUP Milestone Report.," ed, 2017.
[94] T. L. Ulrich, "Modeling the Uranium-Silicon Phase Equilibria Based on Computational and Experimental Analysis, Ph.D. Dissertation," Ph.D., University of South Carolina, 2019.
[95] M. Ugajin and A. Itoh, "Experimental investigations on the chemical state of solid fission-product elements in U3si2," *J. Alloys Compd.,* vol. 213/214, pp. 369-371, 1994.
[96] J. Turner, J. Buckley, G. Phillips, and T. J. Abram, "The use of gadolinium as a burnable poison within the U_3Si_2 fuel pellets," *J. Nucl. Mater.,* vol. 509, pp. 204-211, 2018.
[97] D. Nanopoulos, "Mechanistic modelling of swelling in the accident tolerant fuel candidate U_3Si_2, Master's Thesis," KTH Royal Institute of Technology, Stockholm, Sweden, 2017.
[98] G. Ischia, H.-R. Wenk, L. Lutterotte, and F. Berberich, "Quantitative Rietvel texture analysis of zirconium from single synchotron diffraction images," *J. Appl. Cryst.,* vol. 38, pp. 377-380, 2005.
[99] A. Jain *et al.,* "The Materials Project: A materials genome approach to accelerating materials innovation," *APL Mater.,* vol. 1, p. 011002, 2013.
[100] P. Rogl, H. Noël, and T. Le Bihan, "Phase equilibria and magnetism in the Mo-Si-U system," *J. Nucl. Mater.,* vol. 288, pp. 66-75, 2001.
[101] K. Momma and F. Izumi, "VESTA: A three-dimensional visualization system for electronic and structural analysis," *J. Appl. Cryst.,* vol. 41, pp. 653-658, 2008.
[102] C. W. Bale *et al.,* "FactSage Thermochemical Software and Databases," *Calphad,* vol. 26, pp. 189-228, 2002.
[103] OECD-NEA. "TAF-ID: Thermodynamics of Advanced Fuels - International Database." https://www.oecd-nea.org/science/taf-id/ (accessed 2019).
[104] A. Shukla, Y.-B. Kang, and A. D. Pelton, "Thermodynamic assessment of the Ce–Si, Y–Si, Mg–Ce–Si and Mg–Y–Si systems," *Int. J. Mat. Res.,* vol. 100, p. 208, 2009.
[105] M. V. Bulanova, P. N. Zheltov, K. A. Meleshevich, P. A. Saltykov, and G. Effenberg, "Cerium-silicon system," *J. Alloys Compd.,* vol. 345, pp. 110-115, 2002.
[106] H. Okamoto, "Silicon-Yttrium," *J. Phase Equilib. Diff.,* vol. 32, p. 475, 2011.
[107] M. Huang, D. L. Schlagel, F. A. Schmidt, and T. A. Lograsso, "Experimental investigation and thermodynamic modeling of the Gd-Si system," *J. Alloys Compd.,* vol. 441, pp. 94-100, 2007.
[108] M. Hillert, *J. Alloys Compd.,* vol. 320, p. 161, 2001.
[109] G. Kresse and J. Furthmüller, "Efficient iterative schemes for ab initio total-every calculations using a plane-wave basis set," *Phys. Rev. B.,* vol. 54, pp. 11169-11186, 1996.
[110] J. P. Perdew, K. Burke, and M. Ernzerhof, "Generalized gradient approximation made simple," *Phys. Rev. Lett.,* vol. 77, pp. 3865-3868, 1996.

[111] S. L. Dudarev, G. A. Botton, S. Y. Savrasov, C. J. Humphreys, and A. P. Sutton, "Energy-electron-loss spectra and the structural stability of nickel oxide: An LSDA+U study," *Phys. Rev. B.*, vol. 57, pp. 1505-1509, 1998.
[112] B. Meredig, A. Thompson, H. A. Hansen, C. Wolverton, and A. van de Walle, "Method for locating low-energy solutions within DFT+U," *Phys. Rev. B*, vol. 82, p. 195128, 2010.
[113] P. Boulet, F. Wastin, E. Colineau, J. C. Griveasu, and J. Rebizant, "The binary system Pu-Si: Crystallochemistry and magnetic properties," *J. Phys.: Condens. Matter*, vol. 15, pp. S2305-S2308, 2003.
[114] J. Leppänen, M. Pusa, T. Viitanen, V. Valtavirta, and T. Kaltiasenaho, "The Serpent Monte Carlo code: Status, development and applications in 2013," *Ann. Nucl. Energy*, vol. 82, pp. 142-150, 2015.

[115] F. Cappia and J. M. Harp, "Postirradiation examinations of low burnup U_3Si_2 fuel for light water reactor applications," *J. Nucl. Mater*, vol. 518, pp. 62-79, 2019.
[116] H. Wang, F. Wang, K. Jones, and G. J. Miller, *Inorg. Chem.*, vol. 50, p. 12714, 2011.
[117] B. Y. Kotur and I. R. Mokra, *Inorg. Mater.*, vol. 30, p. 729, 1994.
[118] "ICSD: Inorganic Crystal Structure Database." FIZ Karlsruhe. https://icsd.products.fiz-karlsruhe.de/ (accessed.
[119] M. Ugajin, A. Itoh, S. Okayasu, and Y. Kazumata, "Uranium molybdenum silicide $U3_MoSi2$ and phase equilibria in the U-Mo-Si system," *J. Nucl. Mater.*, vol. 257, pp. 145-151, 1998.

[120] M. Boyko, N. Muts, I. Muts, and R. Gladyschevskii, "Structure refinements of the compounds Pr_5Si_3 and Zr_3Si_2 " *Chem. Met. Alloys.*, vol. 6, pp. 56-62, 2013.
[121] A. Berche, N. Dupin, C. Guéneau, C. Rado, B. Sundman, and J. C. Dumas, *J. Nucl. Mater.*, vol. 411, p. 131, 2011.
[122] D. L. Adorno *et al.*, "Compatibility of U_3Si_2 fuel with Zr, FeCrAl, and SiC/SiC based cladding, NEUP Milestone Report," ed, 2018.
[123] G. Kępisty and J. Cetnar, "On the discrepancies between FIMA and specific burnup," *Prog. Nucl. Energ.*, vol. 98, pp. 187-192, 2017.
[124] J. T. White, A. W. Travis, J. T. Dunwoody, and A. T. Nelson, "Fabrication and thermophysical property characterization of UN/U_3Si_2 composite fuel forms," *Journal of Nuclear Materials*, vol. 495, pp. 463-474, 2017, doi: doi.org/10.1016/j.jnucmat.2017.08.041.
[125] K. D. Johnson, A. M. Raftery, D. A. Lopes, and J. Wallenius, "Fabrication and microstructural analysis of UN-U3Si2 composites for accident tolerant fuel applications," *Journal of Nuclear Materials*, vol. 477, pp. 18-23, Aug 15 2016, doi: 10.1016/j.jnucmat.2016.05.004.
[126] A. M. Raftery, "Fabrication and Characterization of UN-USix Nuclear Fuel," Master in Nuclear Energy Engineering, Reactor Physics Department, KUNGLIGA TEKNISKA HÖGSKOLAN, 2015.

[127] J. P. Hammond, "Process for Sintering Uranium Nitride with a Sintering Depressant," US, 1965.

[128] L. H. Ortega, B. J. Blamer, J. A. Evans, and S. M. McDeavitt, "Development of an accident-tolerant fuel composite from uranium mononitride (UN) and uranium sesquisilicide (U-3 Si-2) with increased uranium loading," *Journal of Nuclear Materials*, vol. 471, pp. 116-121, Apr 1 2016, doi: 10.1016/j.jnucmat.2016.01.014.
[129] L. Lutterotti, M. Bortolotti, G. Ischia, I. Lonardelli, and H. R. Wenk, "Rietveld texture analysis from diffraction images," *Zeitschrift Fur Kristallographie*, pp. 125-130, 2007 2007.
[130] G. Kresse and J. Hafner, "ABINITIO MOLECULAR-DYNAMICS FOR LIQUID-METALS," *Physical Review B*, vol. 47, no. 1, pp. 558-561, Jan 1 1993, doi: 10.1103/PhysRevB.47.558.
[131] H. J. Monkhorst and J. D. Pack, "Special points for Brillouin-zone integrations," *Physical Review B*, vol. 13, p. 5188, 1976, doi: https://doi.org/10.1103/PhysRevB.13.5188.

[132] C. W. Glass, A. R. Oganov, and N. Hansen, "USPEX - Evolutionary crystal structure prediction," (in English), *Computer Physics Communications,* Article vol. 175, no. 11-12, pp. 713-720, Dec 2006, doi: 10.1016/j.cpc.2006.07.020.
[133] H. T. Stokes and D. M. Hatch, "FINDSYM: program for identifying the space-group symmetry of a crystal," *Journal of Applied Crystallography,* vol. 38, no. 1, pp. 237-238, 2005, doi: doi:10.1107/S0021889804031528.
[134] A. van de Walle, M. Asta, and G. Ceder, "The Alloy Theoretic Automated Toolkit: A user guide," *Calphad-Computer Coupling of Phase Diagrams and Thermochemistry,* vol. 26, no. 4, pp. 539-553, Dec 2002, Art no. Pii s0364-5916(03)00005-1, doi: 10.1016/s0364-5916(02)80006-2.
[135] A. van de Walle and G. Ceder, "Automating first-principles phase diagram calculations," *Journal of Phase Equilibria,* vol. 23, no. 4, pp. 348-359, Aug 2002.
[136] L. Dumitrescu and B. Sundman, "A THERMODYNAMIC REASSESSMENT OF THE SI-AL-O-N SYSTEM," (in English), *Journal of the European Ceramic Society,* Article vol. 15, no. 3, pp. 239-247, 1995, doi: 10.1016/0955-2219(95)93945-y.
[137] J. Williams and R. A. J. Sambell, "THE URANIUM MONOCARBIDE-URANIUM MONONITRIDE SYSTEM," *Journal of the Less-Common Metals,* vol. 1, no. 3, pp. 217-226, 1959 1959, doi: 10.1016/0022-5088(59)90030-x.
[138] R. E. Rundle, N. C. Baenziger, A. S. Wilson, and R. A. McDonald, "THE STRUCTURES OF THE CARBIDES, NITRIDES AND OXIDES OF URANIUM," *Journal of the American Chemical Society,* vol. 70, no. 1, pp. 99-105, 1948 1948, doi: 10.1021/ja01181a029.
[139] R. Pottgen, D. Kaczorowski, and W. Jeitschko, "CRYSTAL-STRUCTURE, MAGNETIC-SUSCEPTIBILITY AND ELECTRICAL-CONDUCTIVITY OF THE URANIUM SILICIDE CARBIDES U3SI2C2 AND U20SI16C3," *Journal of Materials Chemistry,* vol. 3, no. 3, pp. 253-258, Mar 1993, doi: 10.1039/jm9930300253.
[140] M. C. Morris *et al.*, "Standard X-ray diffraction powder patterns. Section 19 - Data for 51 substances," *Standard X-ray diffraction powder patterns. Section 19 - Data for 51 substances,* pp. iv+114 pp-iv+114 pp, Dec. 1982.
[141] P. Guinet, H. Vaugoyeau, and J. Jolivet, "U3SI-C SECTION OF U-C-SI DIAGRAM NEAR U3SI PHASE UP TO 950 DEGREES C," *Journal of Nuclear Materials,* vol. 36, no. 1, pp. 94-+, 1970, doi: 10.1016/0022-3115(70)90065-6.
[142] C. Utton, "Thermodynamic Assessment of U-Si-C system," 2009.
[143] J. Grobner, H. L. Lukas, and F. Aldinger, "Thermodynamic calculation of the ternary system Al-Si-C," *Calphad-Computer Coupling of Phase Diagrams and Thermochemistry,* vol. 20, no. 2, pp. 247-254, Jun 1996, doi: 10.1016/s0364-5916(96)00027-2.
[144] C. Gueneau *et al.*, "Thermodynamic modelling of advanced oxide and carbide nuclear fuels: Description of the U-Pu-O-C systems," *Journal of Nuclear Materials,* vol. 419, no. 1-3, pp. 145-167, Dec 2011, doi: 10.1016/j.jnucmat.2011.07.033.

Data Availability

The raw data required to reproduce these findings are available to download from https://osf.io/mdkzr/. The processed data required to reproduce these findings are available to download from https://osf.io/mdkzr/.

Project-Produced Publications

Impact of Fission Product Inclusion on Phase Development in U_3Si_2 Fuel, Kaitlin E. Johnson, Denise L. Adorno, Vancho Kocevski, Tashiema L. Ulrich, Joshua T. White, Antoine Claisse, Jacob W. McMurrary, Theodore M. Besmann, submitted to J. Nucl. Mat.

High Temperature Neutron Diffraction Investigation of U_3Si_2, Tashiema L. Ulrich, Sven C. Vogel, Joshua T. White, David A. Andersson, Elizabeth Sooby Wood, Theodore M. Besmann, Materialia, accepted.

Investigation of the on-site Coulomb correction and temperature dependence of the stability of U-Si phases using DFT+U, V. Kocevski, D.A. Lopes, T.M. Besmann, J. Nucl. Mat. 524 (2019) 157-163 https://doi.org/10.1016/j.jnucmat.2019.07.003

Experimental and computational assessment of U-Si-N ternary phases, D.A. Lopes, T.L. Wilson, V. Kocevski, E.E. Moore, T.M. Besmann, E. Sooby Wood, J.T. White, A.T. Nelson, S.C. Middleburgh, A. Claisse, J. Nucl. Mat. 516 (2019) 194-201 DOI: 10.1016/j.jnucmat.2019.01.008

Stability of U_5Si_4 phase in U-Si system: Crystal structure prediction and phonon properties using first-principles calculations, D.A. Lopes, V. Kocevski, T. L. Wilson, E. E. Moore, T. M. Besmann, J. Nucl. Mat., Volume 510, Pages 331-336 (2018).

Uranium Nitride-Silicide Advanced Nuclear Fuel: Higher Efficiency And Greater Safety, Tashiema L. Wilson, Emily E. Moore, Denise Adorno Lopes, Vancho Kocevski, Elizabeth Sooby Wood, Joshua T. White, Andrew T. Nelson, Jacob W. McMurray, Simon C. Middleburg, Peng Xu & Theodore M. Besmann, Advances in Applied Ceramics 117 (S1) s76-s81, (2018) DOI:10.1080/17436753.2018.1521607

Modeling the Uranium-Silicon Phase Equilibria Based on Computational and Experimental Analysis, Tashiema L. Ulrich, Ph.D. Thesis, University of South Carolina, December, 2019.